Politecnico di Torino

ScuDo
Scuola di Dottorato ~ Doctoral School
WHAT YOU ARE, TAKES YOU FAR

Doctoral Dissertation
Doctoral Program in Management, Production and Design (36^{th}cycle)

Towards effective production in DED: linking process parameters to the properties of the deposition

By

Adriano Nicola Pilagatti

******

Supervisor(s):
Prof. E. Atzeni, Supervisor
Prof. A. Salmi, Co-Supervisor

Doctoral Examination Committee:
Prof. S.L. Campanelli, Referee, Politecnioco di Bari
Prof. M. Barletta, Referee, Università Roma Tre
Prof. P. Minetola, Politecnico di Torino
Prof. P. Stavropoulos, University of Patras
Prof. E. Savio, Università di Padova

Politecnico di Torino
2024

Declaration

I hereby declare that, the contents and organization of this dissertation constitute my own original work and does not compromise in any way the rights of third parties, including those relating to the security of personal data.

Adriano Nicola Pilagatti
2024

* This dissertation is presented in partial fulfillment of the requirements for **Ph.D. degree** in the Graduate School of Politecnico di Torino (ScuDo).

Fight the ignorance, read! – Lella Leoci

Acknowledgements

The author extends heartfelt gratitude to Professor Eleonora Atzeni and Professor Alessandro Salmi for their exceptional mentorship throughout the doctoral journey. Their unflagging respect for the author, both as an individual and as a scholar, has been deeply impactful. Their step-by-step guidance and invaluable teachings on scientific methodology and problem-solving approaches have been instrumental in shaping this research. Without their guidance, this work would not have reached fruition. They have earned the author's highest esteem and gratitude. Furthermore, the author is indebted to them for imparting a genuine passion for the field, enriching not only this research but also the author's entire professional outlook.

An acknowledgment is also made to Professor Luca Iuliano and the entire IAM@PoliTo (Integrated Additive Manufacturing Center at the Politecnico di Torino) for providing an intellectually stimulating environment and essential resources for this research. Special thanks are expressed to laboratory technicians Giovanni Marchiandi, Matteo Perrone, and Manuele Masse for their consistent and courteous technical assistance.

Special acknowledgement is given to Professor Elvio Bonisoli, whose untimely passing last year is deeply mourned. The author's knowledge is mainly attributable to his teachings. Despite his busy schedule, he always found time to impart wisdom with kindness. The invaluable bond of esteem and respect between the author and Professor Bonisoli will forever be cherished.

The author wishes to express gratitude to Professor Abdollah Saboori for invaluable insights into materials and techniques, as well as for his ongoing support, esteemed kindness, and understanding. Acknowledgments are extended to Professor Paolo Minetola for his timely and critical assistance whenever needed. Further appreciation is conveyed to Professor Diego Manfredi and Dr. Alberta Aversa for their invaluable support and collaboration in material science. Their personal kindness and

constant availability have greatly enriched this work. Special and heartfelt thanks are directed to Professor Gianfranco Genta, whose passion and pedagogical approach have served as a turning point in the methodological orientation of this thesis.

The authors extend further appreciation to their colleagues who have been instrumental in both the intellectual and practical aspects of this research journey. The author wishes to thank Josip Vincic, whose collaboration has grown into a genuine friendship, enriching both the academic and personal dimensions of this endeavor. A special acknowledgment is reserved for Luigi Panza, a colleague and friend whose esteem has been long-standing. His advice, opinions, and overall attitude have been pivotal in shaping both the author's personal and professional growth. The author acknowledges Dr. Gabriele Piscopo, whose remarkable doctoral work has provided intellectual inspiration for this research. Gratitude is extended to Mirna Poggi, a colleague with whom the author began this academic journey.

The author is particularly indebted to colleague Giuseppe Vecchi, who initially was a student under the author's guidance and later evolved into a reliable and invaluable colleague. His unwavering kindness and availability have been nothing short of invaluable. The gratitude is also extended to Federica Valenza for her support and mutual respect. Her kindness, willingness to engage in new challenges, and overall availability are not only highly valued, but also characteristics the author believes will propel her to great lengths in her future endeavors.

The acknowledgment is extended to Mankirat Singh Khandpur for his consistent willingness to assist. Beyond being a highly respected and skilled colleague, his contributions have significantly aided the author in this research journey. The authors extend an appreciation to Marco Viccica, a colleague with whom the author initiated this academic journey and who has consistently offered assistance. A special acknowledgment is given to Mattia Glorioso for his constant support and specific assistance in the area of microcontrollers. The author is grateful and highly esteeming Dr. Giacomo Maculotti, whose advice, support, and respect are acknowledged and hold invaluable worth for the author. Particular acknowledgment is also due to Dr. Mohammad Hossein Mosallanejad and colleague Mohammad Taghian Todeshki for their remarkable kindness and unwavering support. Their contributions have been instrumental in the development of a supportive and enriching research environment.

An acknowledgment is extended to John Stavridis and all the technicians at Prima Additive for their support. Particular gratitude is directed to John for his esteem and unwavering assistance.

Special thanks are extended to Elias De Smet and Kevin John, esteemed and trusted colleagues with whom the author participated in and won the euspen Talent Program at CERN in Geneva. For them, the author has deep esteem, respect, and admiration.

Special thanks are extended to Ilaria Lagalante, Serena Lerda, and Jayant Barode for their invaluable assistance in the laboratory setting. Their expertise and timely advice have been crucial in the successful completion of the experimental component of this research.

The author wishes to express profound gratitude to Professor Panagiotis Stavropoulos and Harry Bikas for extending the invaluable opportunity for a visiting period and for their unwavering support while integrating into the team. Further acknowledgment is due to Alexios Papacharalampopoulos, Vicky Panagiotopoulou, Kyriakos Sampatakakis, Konstantinos Tzimanis, Thanassis Souflas, Christos Papaioannou, Anna-Maria Korfiati, Christos Gerontas, and Nick Porevopoulos, as well as all the staff and student members of the LMS. The warm welcome and sustained support throughout the author's stay have been integral to the overall research experience and are deeply appreciated.

The author wishes to express heartfelt gratitude to all friends and family members who have offered emotional and moral support throughout this long journey. Although it is inevitable to inadvertently omit someone in this acknowledgment, particular thanks are extended to Mauro Siciliano, Giulia Salvatore, and Ilaria Longo for their unwavering support. Among all friends, special mention must be made of Onofrio Marzolla, Sergio Petrosillo, and Giuseppe Capra, who have consistently supported the author's choices and provided motivation through both highs and lows. The author wishes to express heartfelt gratitude to all friends who have generously dedicated their time (often between various matches) throughout the doctoral period. Foremost among them is Leandro Dionigi Mallamaci, whose kindness and friendship have been invaluable for a prolonged period. Special thanks are also extended to Olmo Recami, Damiano Pivotto, Stefano Caccialupi, Francesco Coti, and Federico Giuffrida for their camaraderie and support, which have been significant sources of relief and motivation during the demanding journey of doctoral studies.

Sincere gratitude is also directed towards Lella Leoci and Piero Picoco, individuals whose worth to the author is beyond measure. Their support and kindness have left an indelible impact on the author's life. Additional heartfelt appreciation is extended to Roberto Rizzi, Eleonora Di Carlo, Flavio Liam Rizzi, and Isabel Rizzi, who constitute a second family for the author and have provided invaluable emotional sustenance.

Special appreciation is bestowed on my cousin Paolo Recchia, who has consistently served as a guiding light in both my personal and professional life. His role as an inspiration in life cannot be understated.

Last but not least, profound appreciation is conveyed to Pamela Pipoli, the author's life partner. Her influence is immeasurable, shaping who the author has become and will continue to evolve into. This work is as much hers as it is the author's, and for that, the deepest gratitude is expressed.

Abstract

The rapidly advancing field of Additive Manufacturing (AM) has ushered in a myriad of technological innovations, among which Direct Energy Deposition with Laser Beam and Powder Feedstock Material (DED-LB/Powder) shows remarkable potential for efficient material deposition in industrial applications. However, optimizing these systems demands an interdisciplinary methodology supported by robust process parameters. This study employs the Design of Experiments (DoE) to navigate this complex landscape, offering a systematic approach to establishing reliable, data-driven process parameters.

This work is structured into two main parts. The first focuses on characterizing the powder feeder system and narrowing down the variables that interact during the fabrication process. This phase is critical for isolating key parameters and laying the groundwork for subsequent optimization. The second part is devoted to the experimental development and testing of a method for establishing a linkage between the three typical physical processes in DED: powder stream dynamics, melt pool formation, and track solidification. By comprehensively examining these interrelated phenomena, the study aims to create a cohesive framework that enhances the predictability and robustness of DED-LB/Powder systems, thereby advancing their readiness for broader industrial applications.

The first segment of this study focuses on the comprehensive characterization of the powder stream process within a powder feeder system. Utilizing a combination of experimental techniques, statistical analyses, and regression methods, response surfaces were derived. These surfaces not only delineate the operational boundaries and ranges but also enable the precise setting of factors to achieve a specified powder mass flow rate. The subsequent phase optimizes the carrier gas level, essential for adequate powder transportation. By tuning this variable, the study establishes the

optimal gas level required for consistent and accurate deposition, thereby minimizing variability.

The second segment of this study is dedicated to the formulation of mathematical models that serve as a bridge between three core physical processes involved in DED. Through hypothesis testing and multifactorial experimentation, the efficacy and robustness of the developed methodology were rigorously evaluated. Specifically, three physical properties of the specimens—density, porosity, and micro-hardness—and one geometric property, the target height growth, were examined. A single experiment was conducted to assess both the robustness and sensitivity of the method. Utilizing regression analyses, relationships among these variables were established. In the final phase, a computational code was developed that provides end-users with the necessary process parameters tailored to varying input conditions.

The meticulous analyses conducted in this study validate the initial hypotheses and generalize the findings, making them both applicable and adaptable to a wide array of DED-LB/Powder systems. This work comprehensively addresses the initial research questions and provides a nuanced understanding of the DED-LB process, laying the groundwork for future research in this rapidly evolving field. Through the systematic exploration and validation of key process parameters and their interactions, the study establishes a rigorous mathematical framework that facilitates optimized material deposition. The contributions of this research stand as a seminal effort in bridging the knowledge gaps in DED-LB systems and offer a robust foundation for subsequent investigations.

Contents

List of Figures

List of Tables

Nomenclature

Greek Symbols

α	Type I error
β	Type II error
κ	Powder surplus – But-to-fly ratio

Acronyms / Abbreviations

$\bar{R}$	Ideal gas constant
χ^2-test	Pearson's Chi-squared test for independence or Goodness-of-Fit
ΔH_{vap}	Enthalpy of vaporization
ΔT	Temperature increase
ΔZ	Track height = Z-increment per layer
A_t	Total area of the deposition head channels
BCs	Boundary Conditions
c	Specific heat of the melt pool (liquefied state)
D	Laser beam diameter
D_{track}	Track penetration depth
E	Energy density
E_k	Kinetic energy

F Powder density

F-test F-test for equality of variance

H Track height

H_0 Null hypothesis

H_1 Alternative hypothesis

H_A Air absolute humidity

H_R Air relative humidity

m_p Average mass of the powder particle

$m_{meltpool}$ Melt pool mass

n Number of replications

$n_{channels}$ Number of channels of the deposition head

O_e Overlap efficiency

p Air pressure

P_t Total perimeter of the deposition head channels

p_v Saturation vapour pressure

Q_p Powder mass flow rate

Q_{track}

R Volumetric powder flow rate divided by volumetric track rate

r Pearson correlation coefficient

R^2 Coefficient of Determination

$R^2(adj)$ Adjusted Coefficient of Determination

$R^2(pred)$ Predicted Coefficient of Determination

T Temperature

t-test Student's t-test for statistical significance

T_A Temperature of the air inside of the chamber

T_T Thermocouple temperature

T_{Air} Air temperature

v Travel speed

V_p Volumetric powder flow rate

v_p Velocity of the powder

V_{Ar} Carrier gas flow rate (Ar)

V_{cg} Carrier gas flow rate

v_{cg} Velocity of the carrier gas

V_{track} Volumetric track rate

W Track width

Z-test Z-test for statistical significance

3D-printing Three dimensional printing

MS_{Error} Mean square of the error

$MS_{Treatment}$ Mean square of the treatments

SS_{Model} Sum of square of the model

ADT Anderson-Darling test

AM Additive Manufacturing

ANCOVA Analysis of Covariance

ANOVA Analysis of Variance

CCD Central composite design

CFD Computational Fluid Dynamics

CNC Computer Numerical Control

CT Computed tomography

CV Coefficient of Variation

D-WAAM Double Wire Arc Additive Manufacturing

DED Directed Energy Deposition

DED-Arc/Wire Directed Energy Deposition Arc Wire

DED-LB/Powder Laser Beam Powder Directed Energy Deposition

DoE Design of Experiment

ES Effect Size

FFF Fused filament fabrication

FGM Functionally Graded Materials

GED Global Energy Density

GMAW Gas Metal Arc Welding

GTAW Gas Tungsten Arc Welding

HAZ Heat Affected Zone

IoT Internet of Things

JIT Just-in-Time

LOF lack-of-fit

LQM Least squares method

MS Mean square

NDT Non-destructive testing

NPP Normal probability plot

OC Operating Characteristic curve

OFAT One-factor-at-a-time

PCC Pearson correlation coefficient

PE Pure error

PRESS Predicted residual error sum of squares

RSM Response Surface Methodology

SL Significance level

SLS Selective laser sintering

SS Sum of square

SS_{Error} Error sum of square

SS_{Total} Total sum of square

$SS_{Treatment}$ Treatment sum of square

WAAM Wire Arc Additive Manufacturing

Chapter 1

A gentle introduction to the Directed Energy Deposition

1.1 A modern manufacturing challenge

The contemporary manufacturing sector is experiencing an escalating rate of paradigmatic shifts, necessitating a reevaluation and subsequent update of traditional methodologies. Influenced by the advent of technological innovations, globalization, and rapidly changing customer needs, modern manufacturing environments face unprecedented complexities. These challenges require agile, efficient, and customer-oriented strategies to ensure a sustained competitive advantage. One of the defining aspects of this paradigm shift is the increasing adoption of Industry 4.0 technologies and lean manufacturing principles, both of which have considerable potential to revolutionize the manufacturing landscape [3].

Lean manufacturing has long been the cornerstone of waste reduction, operational efficiency, and Just-in-Time (JIT) delivery [4]. This approach focuses on maximizing value for the customer while minimizing waste and inefficiencies. The lean philosophy is closely aligned with the objectives of Industry 4.0, a term that refers to the digitization and automation of manufacturing processes. Both paradigms aim to achieve exceptional levels of operational efficiency. However, they approach this objective differently: lean through process optimization and waste reduction, and Industry 4.0 through smart technologies and data analytics [5]. Lean manufacturing aims to identify and eliminate waste in many forms, including overproduction, idle

time, and unnecessary transport. Industry 4.0 complements this by enabling real-time monitoring and data analysis, making it easier to identify inefficiencies and adapting processes accordingly. The synergistic effect of these two paradigms could lead to unprecedented levels of waste minimization.

Both lean and Industry 4.0 have significant implications for energy efficiency. Lean manufacturing improves energy use by optimizing production flows, minimized waste, and reduced idle times, reducing energy footprint. Industry 4.0 can improve this through smart energy management systems that dynamically adjust energy usage based on real-time demands. JIT manufacturing, an integral part of lean thinking, aims to produce the right product at the right time, in the right amount. Industry 4.0 technologies such as the Internet of Things (IoT) and real-time data analytics can further fine-tune JIT processes by accurately predicting manufacturing requirements, thereby reducing stock shortages and overstocks [6].

It is precisely within this historical and socio-economic context that Additive Manufacturing (AM) has emerged. This innovative manufacturing technique not only allows considerable flexibility in production, but also finds its utility within the framework of lean manufacturing and Industry 4.0. AM is inherently aligned with the principles of waste reduction, as it enables additive processes that use only material where needed. Moreover, its digital nature makes it an ideal fit for data-driven, automated environments championed by Industry 4.0.

AM, commonly referred to as 3D-printing in non-specialized contexts, is the fabrication of a three-dimensional object from a Computer-Aided Design or digital 3D model. This process involves layer-by-layer deposition, joining, or solidifying material under computer control. The term "3D printing" has become closely associated with fused filament fabrication (FFF), a specific technique invented by Scott Crump. In 1992, Crump filed the patent US5121329A, entitled *"Apparatus and method for creating three-dimensional objects"* [7]. A crucial turning point in the popularization of 3D-printing was the anticipated expiration of this patent on October 30, 2009. This led to a significant decrease in the cost of FDM printers, with prices dropping from over $10.000 to under $1.000. The expiration of the patent had a twofold effect: not only did it catalyze the emergence of consumer-friendly 3D printer manufacturers, such as MakerBot and Ultimaker, but it also intensified commercial interest across various sectors [8]. As a result, 3D-printing technology

experienced rapid proliferation in the hobbyist market and industrial applications, attracting significant media attention and research interest.

1.2 Application of Directed Energy Deposition in modern industry

Building upon the foundational patents dating back to 1983, manufacturing firms initially embraced AM primarily for prototyping [9]. Over the years, the application of AM expanded from this rudimentary function to the production of complex components, including those made of metallic alloys. As industries strive for increased efficiency, reduced waste, and JIT production - all core tenets of lean manufacturing and Industry 4.0 - AM has emerged as a significant player [10, 11].

In line with these trends, 3D-printing technology has evolved to serve the consumer market and solve complex industrial problems, particularly waste reduction and component recovery. A subset of AM techniques that has garnered considerable attention for this specific purpose is Directed Energy Deposition (DED). This technology became prominent in July 2021, when a fully functional stainless steel bridge was constructed using Directed Energy Deposition Arc Wire (DED-Arc/Wire), also known as Wire Arc Additive Manufacturing (WAAM) [12]. Subsequently, it was installed on the Oudezijds Achterburgwalin canal in Amsterdam (see Fig. 1.1).

Fig. 1.1 MX3D bridge, world's first 3D printed stainless steel bridge in Amsterdam (NED)

The bridge is a wonder of engineering and embodies real-world implementation of these advanced techniques. It has a sophisticated sensor network that monitors structural integrity and environmental conditions. The data collected are sent to an online repository hosted by The Alan Turing Institute for long-term analysis. This real-time monitoring facilitates predictive maintenance and provides information on structural behavior and environmental interactions. DED technologies like WAAM offer precise control over material deposition, thus minimizing waste. Moreover, they are particularly well suited for repair and remanufacturing applications, presenting a pathway for recovering components that would otherwise be discarded.

In the academic world, interest in AM and DED has grown exponentially. As depicted in Fig. 1.2, this surge, particularly evident in the latter part of the timeline, underscores the growing recognition and exploration of these technologies within scholarly communities. The dashed curves in the graph extend projections up to a decade ahead, predicting the potential trend of scientific publications through 2033. A custom-designed Wide Neural Network was developed and utilized to facilitate these projections. The model was trained using data sourced from Scopus up to 2022. To further validate the robustness and generalizability of the model, a 5-fold Cross-Validation technique was rigorously implemented as an additional verification measure.

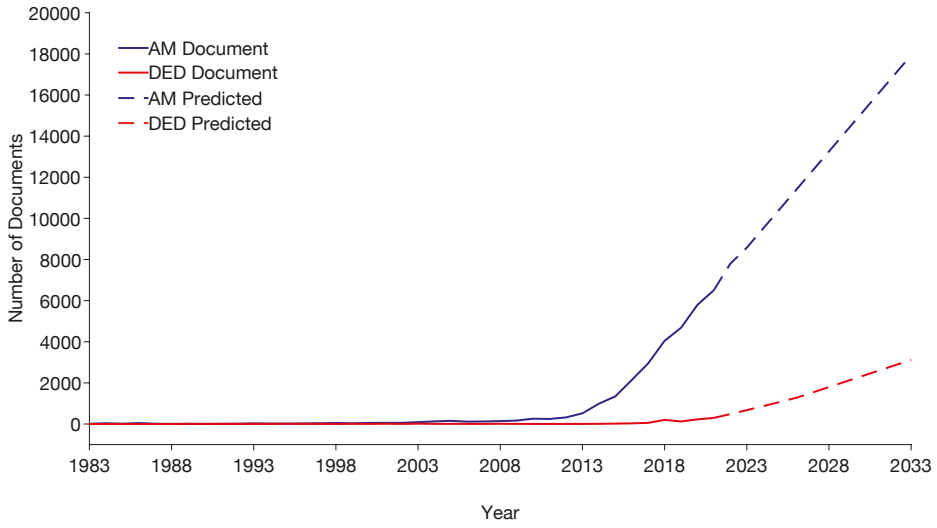

Fig. 1.2 Prediction of academic documents publication with "Additive Manufacturing" and "Directed Energy Deposition" as keywords. Data source from Scopus

Notably, these projections indicate an increasing number of publications on these subjects in the years to come, suggesting that AM and DED are, and will continue to be, hot topics in academic and industrial research for the foreseeable future.

1.3 Research Questionss

In the rapidly evolving field of AM, DED with laser beam, as thermal source, and metal powder (DED-LB/Powder), as a feedstock material, systems hold significant promise for efficient material deposition. However, to exploit the full potential of these systems for industrial applications, it is crucial to develop methodologies that ensure consistent deposition. One of the persistent challenges in this endeavor is the lack of robust process parameters that yield predictable results under various conditions. Achieving this level of consistency is critical for material efficiency and ensuring the mechanical integrity of the deposited components. However, it is also essential for comprehensive industrial adoption beyond isolated case studies.

Addressing these challenges requires an interdisciplinary approach that draws on statistical methodologies to develop evidence-based process parameters. One such statistical tool increasingly employed in engineering research is the Design of Experiments (DoE). The latter minimizes the need for resource-intensive trial-and-error methods by strategically planning experiments to obtain data-driven insights. The two main objectives of this work are summarized in the following research questions:
RQ1: To what extent can a specimen be deposited to meet specified properties leveraging on process parameters utilizing a DED system?
Within the intricate dynamics of DED-LB systems, many practitioners have often gravitated towards intuitive judgments. This often leads them to adopt methodologies that might seem rigorous, such as the one-factor-at-a-time approach. However, this can result in considerable use of resources without necessarily achieving optimal outcomes. It is essential to comprehend its underlying potential and limitations for effective application of DED technology. Consequently, this research promotes a methodical approach, focusing on how process parameters can be leveraged effectively to ensure that specimens are deposited to meet the desired properties.

RQ2: How do deposition behaviors vary under diverse conditions when employing DED-LB, and which factors determine its robustness?
Understanding the variability in deposition behaviors is paramount in the intricate

realm of DED-LB/Powder. Many users might lean towards a reductionist perspective on system behavior, but this research takes a more comprehensive stance. The primary objective of this work is to validate the hypotheses formulated in the previous research question and to assess its robustness. This was achieved through a sensitivity analysis, also called factor screening in the specific experimental terminology. By systematically delving into these interactions, we intend to significantly enhance the predictability and reliability of DED-LB processes, paving the way for efficient production and consistently high-quality results.

Chapter 2

An overview of the Directed Energy Deposition

The DED technique merits significant attention in the constantly advancing AM landscape. As delineated by the ISO/ASTM 52900:2021(E) standard [13], DED is an AM procedure wherein focused thermal energy is employed to fuse materials during deposition. Such versatility makes DED suitable for various applications, from manufacturing complex components to rapid prototyping and meticulous repair. Following the ASTM F3187-16 standard [14], the potential of the DED is in scenarios like component repair, expedited prototyping, and small batch fabrication.

Fig. 2.1 details the classification of single-step AM techniques as defined by ISO. Notably, two primary states of fusion are identified: melted and solid. The latter pertains to the Sheet Lamination technique. Under the melted category are two different feedstock materials: filament/wire and powder type. Another significant differentiation is how the material is distributed. This distinction is between powder bed techniques, where powder layers are laid on a platform, and those employing a deposition nozzle. Notably, the latter can feed material as a filament or powder. In recent years, the market has witnessed the emergence of hybrid systems that can deposit both forms of material. A notable example is the Ianus cell by Prima Additive (Torino, ITA) [15]. Furthermore, the type of thermal source is also categorized, with options being Electron Beam (-EB), Arc (-Arc), or Laser Beam (-LB). Based on the combinations of the categories mentioned above, the specific denomination of the process is ascertained.

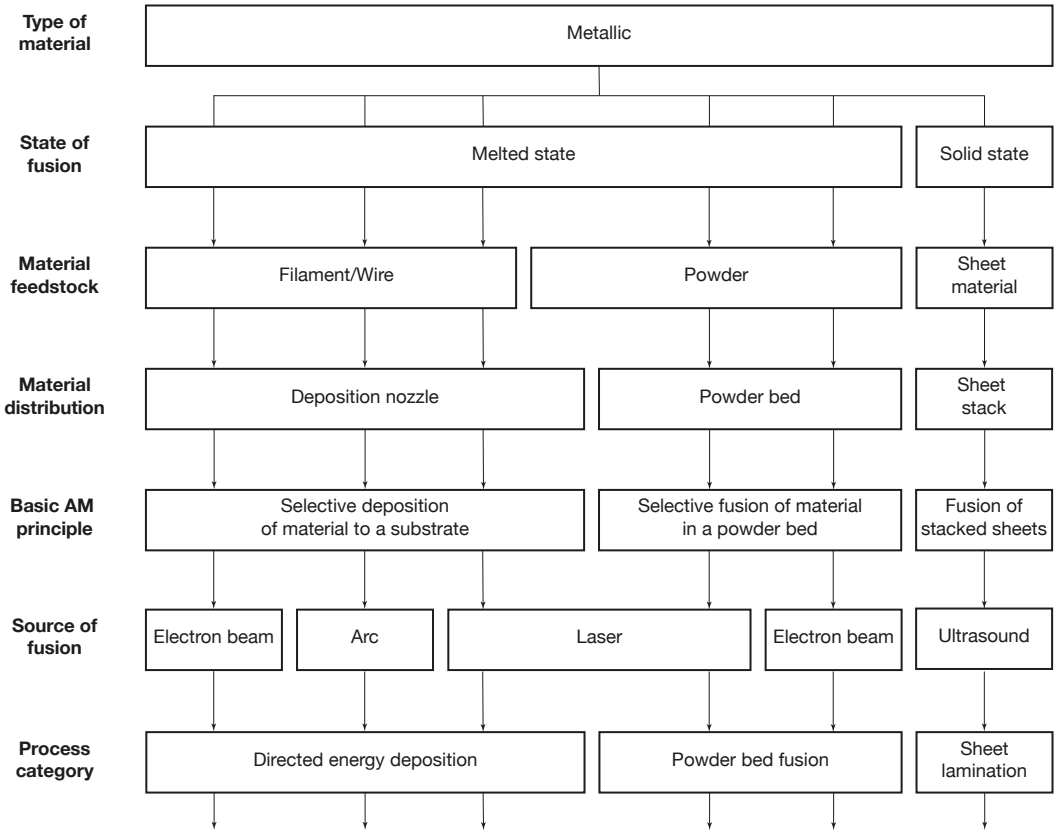

Fig. 2.1 Single-step AM processing principles for metallic materials [13]

The following sections will further explore the mechanics and physics underlying the DED method, particularly emphasizing DED-LB/Powder, which is the system configuration employed and analyzed in this work.

2.1 The physics beyond the process

The intricacies behind the DED technique are a mosaic of intertwined physical phenomena, each unique contributor to the overall process. Unravelling the nuances of this deposition method is a complex task due to the multitude of coupled micro-phenomena. Researchers often resort to computational models to accurately characterize each intricate facet of the process. These models encompass a multi-physics approach, integrating various physical interactions. In computational modeling, the DED process involves multi-physics simulation, simultaneously examining various system interactions. This approach uses mathematical models consisting of primary

and auxiliary equations and initial conditions. Typically, methods such as the finite element, the finite difference, or the finite volume are used for these simulations. The precision and accuracy of such models are inherently tied to their approximations. As one delves deeper into the complexities, the importance of these approximations grows, directly influencing the fidelity of the predictions made. Thus, the balance of simplification and accuracy becomes a crucial challenge in such endeavors.

Various researchers have ventured into DED physics to distill its complexities into a more straightforward framework. Amongst these, the model posited by Pinkerton [16] has been heralded for its comprehensibility and pragmatism.The simplified model (Fig. 2.2) dissects the DED-LB process into three interacting macro-processes, creating a structure that encompasses the core of the deposition mechanism.

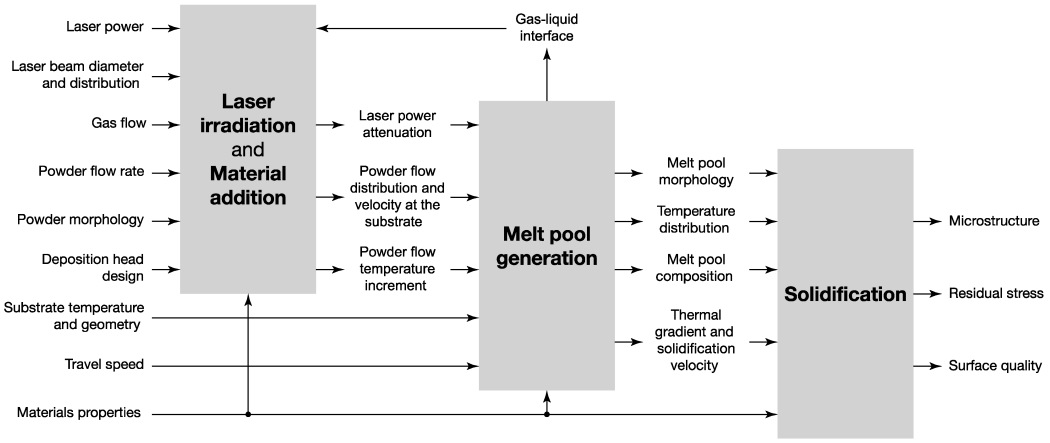

Fig. 2.2 DED-LB physics and process parameters [17]

This delineation not only elucidates the fundamental phenomenology but also aligns with the approach embraced in the current research. Each macro-process comprises input, some of which are adjustable by the operator, known as process parameters. In contrast, other unmanageable input arises from the specific setup of the system, the material properties, and the boundary conditions. Every process step interacts with or is influenced by the next or the previous, establishing an intricate system. In this complex configuration, manipulating a single input variable or parameter can intentionally or not modify one or more outputs. This aligns with the overarching objective of varying inputs to optimize the outputs, as pursued in the current research. In particular, the sequence involves the powder stream, the melt

pool, and the path formation (solidification) processes. The latter visibly delivers the material track, offering a tangible and measurable output.

2.1.1 Powder stream

Deposition head design

The DED-LB/Powder methodology is fundamentally anchored by the powder stream process, recognized as the primary among three main macro-processes. This mechanism defines how powder particles are introduced into the laser interaction zone. In later chapters of this dissertation, the current section will elucidate the various factors influencing the powder stream in terms of their intrinsic significance and exploration. The deposition head is one of the main protagonists in characterizing the powder stream through its integral component, the deposition nozzles. The deposition head is a complex assembly, combining laser optics, deposition nozzles, protective gas nozzles, and a series of sensors. While its configurations may vary, each brings its unique strengths and challenges. Various patented configurations in the market dictate the arrangement of powder delivery nozzles in the DED-LB process, namely the lateral, the coaxial, and the discrete coaxial configurations.

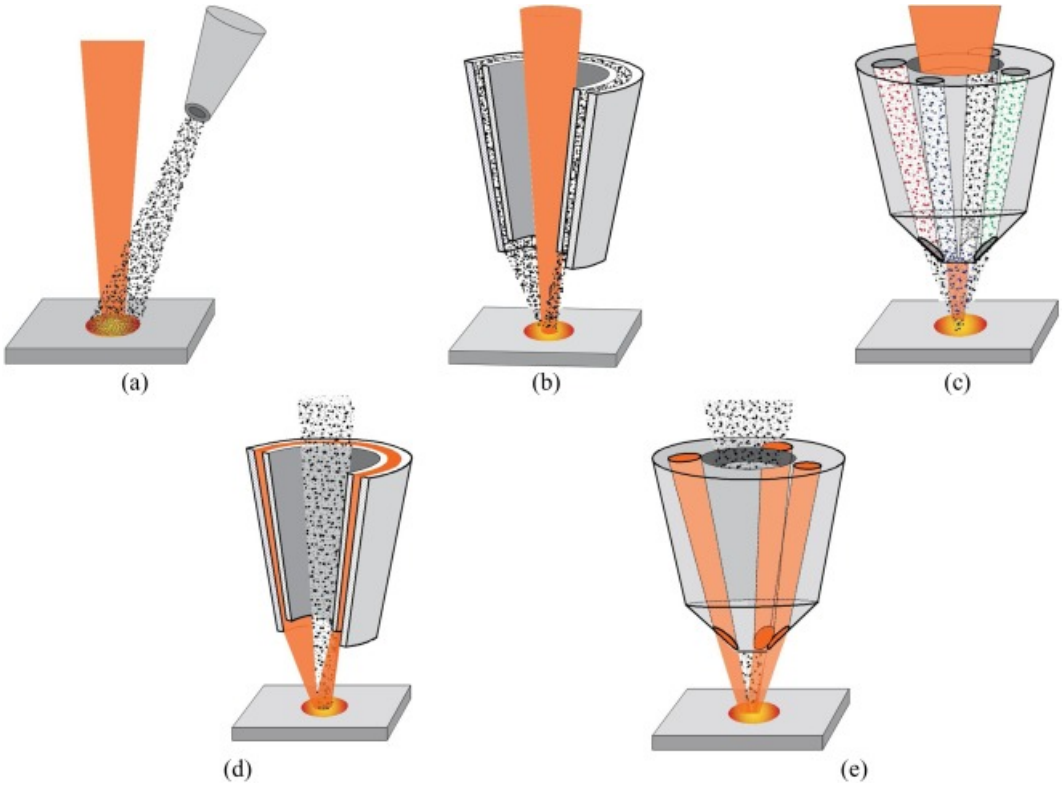

Fig. 2.3 Deposition head configuration: off-axis (a), continuous coaxial (b), discrete coaxial (c). Inverted laser position configuration: continuous coaxial (d) and discrete coaxial (e) [18]

The lateral or off-axis configuration stands out for its simplicity (Fig. 2.3(a)). In this arrangement, the powder feed nozzle is oriented at an angle to the heat source. Although this offers ease of setup, it brings about operational challenges. Specifically, the lateral approach can create asymmetries in the powder temperature, laser beam intensity, and melt pool shape, impacting deposition consistency and the final properties of the part. A significant hurdle with this setup is balancing powder catchment efficiency with surface finish, both influenced by the relative position between the nozzles, the melt pool and the scanning direction [19]. Nonetheless, the configuration proves beneficial in applications valuing straightforward setup.

Coaxial nozzle configurations (Fig. 2.3(b)) have emerged as a natural evolution of the lateral one. They are the most popular choice in the DED-LB process due to their ability to produce complex parts with consistent properties that overshadow the capabilities of lateral feed nozzles. The continuous coaxial nozzle, distinguished by its annular outlet, uses two coaxial cones to direct the powder stream towards the melt pool focal point. The angles of these cones can be adjusted to shift this focus.

Many such nozzles incorporate channels between the cones to ensure a convergent stream created by machining grooves in the inner cone. This design aims at a focused powder stream aligned with the laser beam and a uniform distribution [20].

Discrete coaxial nozzle configurations (Fig. 2.3(c)) employ a unique approach by utilizing multiple distinct channels, typically three to four, to convey the feedstock material directly to the melt pool. The specific orientation of these channels is designed to generate a convergent powder stream, and the subtleties of their positioning critically influence the flow characteristics and the intersection of the focal point of the stream with the laser beam. Like many intricate designs, these nozzles do not adhere to a single prototype, but exhibit various adaptations. However, foundational aspects such as the injection radius, the injection angle, the exit radius of the nozzles, and the stand-off distance remain integral in different versions. A notable feature of these nozzles is the ability to adjust the spatial arrangement of the powder jets relative to the deposited layer. When the rotation of the deposition head is manipulated, the feed position of the powder streams can be varied. However, this adaptability keeps these streams aligned with the laser. The relationship between the geometric parameters of the nozzle and the characteristics of the resultant powder stream is multifaceted.

For example, an increase in the specific dimensions of the nozzle, such as the diameter of the exit and the injection radius, tends to reduce the concentration of powder mass at the focal point. On the contrary, a higher injection angle minimizes the focal spot size, leading to a denser powder concentration. The stand-off distance, which defines the gap between the nozzle and the deposition surface, displays complex interactions with these geometric parameters. Interestingly, the orientation of the nozzle exerts minimal influence on the dynamics of the powder flow, since the powder concentration at the focal point remains largely invariant regardless of its angular position [21]. Furthermore, increasing the number of channels ($n_{channels}$) while maintaining a constant total cross-sectional area (A_t) enhances contact surfaces within the system. This is correlated with an observed increase in pressure drop. Mathematically, this phenomenon can be understood by considering that the radius of each channel decreases as the number of channels increases, given the constant area. The total perimeter P_t, which measures the contact surface, is then given by $P_t = 2\sqrt{n_{channels} \cdot \pi \cdot A_t}$. Significantly, P_t scales with $\sqrt{n_{channels}}$, substantiating the non-linear relationship between the number of channels and the pressure drop within

the system [22]. Thus, given unchanged process parameters, an increase in the number of conduits indicates a probable decrease in the mean powder velocity.

The described configurations are the most commonly used when dealing with powder-based systems. However, there are other coaxial configurations, typically employed for wire feedstock systems, named central feed nozzles. In these systems, the laser and powder channels are inverted in their positions. To prevent the wire from melting before reaching the substrate, the laser is positioned externally to the wire, supplied from the center of the deposition head. These configurations, depicted in Fig. 2.3(d) and Fig. 2.3(e)), can also be applied to powder-based systems, especially in hybrid cells.

The powder feeding mechanism is the second inherent feature of the chosen system. This mechanism can be broadly segmented into three key stages: powder metering, conveyance, and delivery. During the powder metering phase, emphasis is placed on the precise measurement of the powder from its primary storage, often a hopper, ensuring the appropriate quantity is dispatched to the melt pool. Multiple techniques are employed to ensure this accuracy, such as using specialized powder dosing systems to guarantee the correct mass flow rate. Additionally, numerical methods like Computational Fluid Dynamics (CFD) simulations are employed to predict and optimize process behaviors [23]. Alternatively, an experimental approach may also be taken to directly measure and validate the performance and behavior of the system. In the powder conveyance stage, the emphasis shifts to ensuring the transport of the accurately metered powder from its source to the delivery nozzle. The dominant method in this regard uses an inert carrier gas, typically argon, although other strategies such as vibration, auger mechanisms, and gravity chutes are employed in commercially available systems. The powder delivery stage, executed via a specialized nozzle, primarily concentrates the powder stream to a specific focal point. It is important to note that, while these stages might appear distinct, their functionalities frequently intersect and overlap.

Delving deeper into the powder metering and conveyance stages, various techniques emerge, which can be summarized in the following methods:

- **Screw/Auger:** a motor-driven Archimedean screw introduces a specific amount of powder into a gas chamber, from which an inert gas stream subsequently propels it to the delivery nozzle;

- **Vibration-Assisted:** a technique that employs vibratory feeders, capitalizing on mechanisms such as the sealskin and jerk methods. The sealskin method utilizes unequal friction coefficients in orthogonal directions to ensure effective material movement, particularly during relative motion between the track and the material. On the other hand, the jerk method operates on a principle of slow advance followed by a quick return, requiring specific non-linear and asymmetrical conditions for optimal material transport [24];

- **Gravity-Driven:** these systems might experience flow instabilities, especially in narrow chutes, leading to potential granular segregation. The phenomenon known as "Jamming" further complicates the flow by forming arch-like structures of particles that inhibit movement. This obstruction is highly influenced by particle shape rather than material properties and commonly halts granular flow.;

- **Pneumatic:** among the discussed methods, pneumatic powder feeders dominate DED applications. These systems exploit pressure differentials across a network of tubes to facilitate powder metering and transport;

- **Electrostatic:** implementing electric fields to govern granular flow has been previously explored. Specific voltage ranges can influence flow dynamics, resulting in distinctive flow patterns.

Powder characteristics

The physicochemical properties of materials substantially influence the amount of powder transported in the powder stream process. Several studies in the literature have examined different materials, but the focus of this section is different from what is shown. Given that each batch of material produced by a company presents unique challenges and must be characterized individually within the system in question, it is essential to identify a standard method for powder characterization. The most reliable standard for this purpose is undoubtedly ISO/ASTM52907-19 [25]. This standard details and recommends practices to characterize AM metallic powder consistently, reliably, and repeatably. The methodology of this standard will be used later in this study.

According to the ISO/ASTM52907-19 standard, maintaining meticulous documentation and traceability for metal powders is essential. Detailed records encompassing supplier details, product descriptions, storage instructions, and analysis dates are imperative. For example, variables can still introduce inconsistencies even when using the same powder from the same manufacturer, batch, and container. Suppose the container is opened multiple times or stored for extended periods, even under hermetic conditions. In that case, the powder may absorb moisture and form agglomerates that inevitably impact the flow rate. The latter is why powder that has been unused for an extended period still requires pre-treatment, as its characteristic granulometry tends to capture moisture.

Particle size distribution is a multifaceted area where diverse methods yield varied outcomes, from sieving to laser diffraction. It is customary to use standard indices such as *D10*, *D50*, and *D90* for a uniform representation of the data. In terms of the chemical composition, it demands rigorous analysis through techniques like atomic absorption spectrometry and X-ray fluorescence. One intriguing aspect is how powder recycling can subtly alter chemical characteristics, particularly oxygen levels. Densities, both apparent and tap, serve as useful metrics. They help to understand flowability and are pivotal in selecting appropriate testing methods. The density evaluation by a gas pycnometer is particularly revealing, shedding light on the true density and potential porosity of the material.

Morphology, heavily influenced by the powder production process, requires the adherence to established vocabularies, sometimes augmented by advanced imaging. Flowability is inherently complex, dictated by particle size, cohesion, and interparticle friction. Lastly, the standard underscores the criticality of ensuring the absence of contamination. Rigorous examination of representative powder samples can detect and mitigate purity concerns, safeguarding the integrity of the material.

Process parameters

The previously elucidated factors relate to the inherent characteristics of the system and the powder under investigation. Such characteristics remain invariant unless intentionally altered, such as by introducing a different type of powder, material or an alternative powder feeder system. Contrary to these fixed properties, which do not exhibit gradual transitions, the operator must adjust the process parameters according to the operational requirements. A process parameter can be defined as

a quantifiable element of input or transformative activities within a process that affects the resultant outputs. Process parameters in the context of the powder stream predominantly encompass those that modify the powder mass flow rate during the metering phase and are dependent on the specific system in question. Moreover, the role of the carrier gas is crucial in a pneumatic conveyance mechanism in DED-LB, and it is also explored in this doctoral research.

In AM techniques like DED, parallels can be drawn with traditional welding methods concerning shielding gas applications. Specifically, within a DED-LB system that utilizes pneumatic conveyance, the gas employed performs a dual role: facilitating the transportation of powders and shielding the molten pool. Consequently, it is designated as a carrier gas. Technically, the gases employed in conventional welding processes could be appropriated for this purpose, except for flammable gases such as oxygen and hydrogen. Different gases impart unique characteristics to the process, listed below in descending order of their use in DED-LB applications[26, 27]:

- **Argon (Ar):** the most popular shielding gas choice due to its inert nature. Suitable for many welding materials, including sensitive ones like aluminum and stainless steel, Argon enhances weld penetration;
- **Helium (He):** inert like Argon, introduces increased heat input to the joint, leading to wider and deeper penetration, particularly beneficial for thick-walled materials like aluminum or copper;
- **Carbon Dioxide (CO_2):** Often employed for short arc welding, CO_2 is cost-effective and especially suitable for welding galvanized steel. It presents specific challenges, however, including a propensity for increased spatter;
- **Nitrogen (N_2):** Nitrogen is versatile, serving as an alloying element and a shielding gas. In specific contexts, such as the welding of copper, it offers increased heat input without detrimental metallurgical effects [28].

Thus, once the most suitable type of gas has been selected, one of the process parameters that can be manipulated is the flow rate. This is typically regulated via laminar flow through the valves. Inevitably, this directly impacts the rate of powder transported in a system that employs pneumatic conveyance. Therefore, the type of gas and its flow rate are interrelated process parameters that significantly influence the powder stream phenomenon.

Noise sources

Referring to Fig. 2.2, there are specific process parameters that, although not directly related to the feeder system, can significantly influence the powder stream process. Notably, these parameters include the laser power, laser beam diameter, and the gas-liquid interface of the melt pool. All three share a common characteristic: they are heat sources and interrelate reciprocally. The beam diameter, inherent to the system, possesses a specific magnitude and distribution that invariably interacts with the laser power and the resultant melt pool. Expanding on this, the literature suggests that laser radiation significantly affects the velocity of the powder particles. It was demonstrated by Sergachev et al. [29] that when the laser is activated, the speed of these particles tends to increase. The interaction of the beam with the powder stream, influenced by factors such as standoff distance, leads to changes in the effective laser power due to the interplay of absorption, reflection, and scattering [30]. Furthermore, while powder in the DED-LB process customarily melts upon entering the melt pool, there exists potential for it to melt during its in-flight travel under certain conditions.

Lastly, noise sources can be understood as the factors or phenomena that remain elusive for manipulation and control. A quintessential example would be Boundary Conditions (BCs). The number of noise sources in the powder stream process escalates with increasing analytical detail. Notably, air viscosity is a crucial noise factor. In a fluid with high viscosity, the resistive forces against the motion of the body are more significant, consequently reducing its velocity (powder velocity in the DED-LB/Powder). Governed by temperature and pressure, the dynamic viscosity of air rises with increasing temperature, as delineated by the Sutherland model. While generally invariant under moderate pressure conditions, viscosity can be affected by compressibility effects at extreme pressures. Additional noise phenomena may arise from laminar flow effects, pressure decay within containment cylinders, and conduit turbulence. Powder conditions also play a crucial, albeit unpredictable, role in the powder stream. In summary, noise sources encapsulate all those uncontrollable phenomena that directly or indirectly impact the powder-stream process.

2.1.2 Melt pool

Substrate and powder stream interaction

Within the context of DED-LB, it is pertinent to acknowledge the foundational role of laser welding. While both laser welding and DED-LB share the commonality of generating a melt pool, their objectives diverge substantially. Laser welding is fundamentally aimed at the cohesive joining of two components without adding extra material. DED-LB, on the other hand, is designed not only to create a fused zone but also to introduce supplementary material, thereby facilitating layer buildup. This contrasts yet is similar to multi-pass welding techniques such as Gas Tungsten Arc Welding (GTAW) and Gas Metal Arc Welding (GMAW). The latter is commonly employed for its high productivity in controlled environments, while GTAW is adept at specialized conditions like underwater or thin-material welding. Despite these similarities in material addition, the mechanisms and engineering objectives in DED-LB differ substantially.

Mirroring the intricate dynamics inherent in laser welding, the genesis and dynamics of the melt pool in DED-LB are influenced by many factors, making it a multifaceted phenomenon to delineate. This process encompasses phase transitions from solid to liquid, reverting to solid upon incorporating additive material. Intricate thermo-fluid dynamics further compound the inherent complexities within the melt pool. Such dynamics are accentuated by turbulent regimes on the surface of the melt pool due to elevated velocities associated with the carrier gas [28]. Concurrently, the movement of the heat source across the substrate, which subsequently dictates the movement of the melted pool, is intertwined with heat transfer interactions between the substrate and its ambient environment. This brief description merely offers a superficial overview of the intricate processes transpiring during deposition.

Expanding upon the details, as encapsulated by Fig. 2.2, it is discerned that a paramount interaction exists between the melt pool and the powder stream process. Factors that remain relatively invariant encompass the materials of both the substrate and the powder. The chemical composition of the substrate and powder does not have to be identical, but they must be weldable with each other. Focusing on the substrate, it is postulated that its geometrical attributes play a pivotal role in modulating heat transfer phenomena. It is pivotal to delineate the three cardinal mechanisms underpinning heat transfer [31]:

- **Conduction:** refers to transferring heat across solid materials without mass movement;
- **Convection:** pertains to the transfer of heat facilitated by the movement of fluids, encompassing both liquids and gases;
- **Radiation:** involves heat transfer via electromagnetic waves, such as infrared radiation. While conduction and convection necessitate a material medium for their manifestation, radiation can transpire in a vacuum.

Under substrate geometry, surface conditions warrant consideration, specifically form tolerances and roughness [32]. Geometric tolerances, such as stringent requirements for substrate planarity, can critically impact the quality of the melt pool, thereby affecting the deposition process. Surface roughness, characterized as the presence of inherent or mechanically-induced micro-imperfections on the surface, such as variable grooves or scratches, is crucial in the modulation of laser source absorption and reflection due to its optical implications [33].

Shifting the focus to the powder component, its chemical composition and other qualitative properties, as previously outlined, have demonstrated tangible effects on melt pool behavior. Analyzing the interactions between the powder stream mechanism and melt pool generation, a correlation emerges between the attributes of the powder stream and the energy imparted to the melt pool. Noteworthy factors encompass the velocity of the powder particles at the point of impact, which correlates to kinetic energy, factoring in the average particle mass. Additionally, the temperature of the powder, a byproduct of absorbing a portion of the energy of the laser, inevitably results in laser power attenuation. Other considerations include the configuration of the powder stream upon interfacing with the substrate, the distribution of particles, and the laser beam energy distribution. In the literature, it is common to assume the laser power density distribution as Gaussian [34].

However, such assumptions can lead to approximation errors that may significantly impact the outcome. Hence, before adopting any approximation, conducting tests, making measurements, and comparing with the proposed model is imperative. This procedure, termed the principle of induction, will be extensively discussed in Chapter 3. These phenomena represent a subset of the intricate interplay between the melt pool and the powder stream. An additional yet critical mechanism is the

gas-liquid interface of the melt pool, which exerts a retroactive effect on the powder stream, altering the medium through which the powder is conveyed.

Process parameters

Although numerous authors have identified manipulable parameters affecting the melt pool – such as track scan spacing, powder feed rate, laser travel speed, laser power, and laser spot size – an energetic approach is often more insightful and concise. This inclination towards an energy-centric approach can be attributed to various reasons:

1. **Simplicity:** the energetic perspective simplifies the complex interplay between various factors by focusing on the overall energy interactions, providing a clearer insight into the process dynamics;
2. **Uniqueness:** instead of juggling multiple parameters that might interrelate in multifaceted ways, an energy-centric model concentrates on a singular, overarching factor, making the analysis more tractable;
3. **Incorporation of Multiple Factors:** by adopting an energetic perspective, several influencing factors are inherently accounted for, being encapsulated within the energy parameter. this minimizes the chances of overlooking pivotal aspects;
4. **System Independence:** the energy approach allows for a level of abstraction, making the analysis less tethered to the specificities of a given system and, thereby, more universally applicable.

Delving into the energetic approach, the focus rests on discerning how energy interacts with the material across its various manifestations. A crucial metric often employed in this context is the energy density [35]. The latter is crucial, particularly when predicting potential porosity within the deposited material. As the travel speed increases, the dwell time on the substrate decreases, leading to a more contracted melt pool. This results in accelerated cooling due to the reduced energy input. Instead of individually manipulating each parameter, which could inadvertently introduce secondary effects on the melt pool, an energy-centric perspective seeks to control its size, shape, and temperature distribution. Employing energy density as a guiding

metric makes it possible to maintain the desired pool characteristics. Dynamic adjustments, such as modulating laser power, can ensure an optimal solidification rate, resulting in the desired microstructure and properties [36].

Noise sources

Similar to the considerations for the powder stream mechanism, several factors can introduce variability in the dynamics of the melt pool. BCs have a pronounced effect on the melt pool. For instance, the convective heat exchange of the substrate is governed by Newton's law, where the outflowing heat flux is tied to the difference between the temperature of the substrate and the environmental conditions. Consequently, thermal interactions with the surrounding conditions are dictated in part by BCs, which affect the melt pool. Another complex factor to characterize is the flow of the carrier gas, which lowers the melt pool temperature through forced convection. Turbulent flow conditions predominantly influence this phenomenon due to the high velocities involved. Additionally, ambient humidity plays a role; moisture in the atmosphere can absorb some of the energy intended for the melt pool, leading to variations in its characteristics.

The mounting system used within the DED setup warrants attention. Typically metallic, these systems can inadvertently influence the heat exchange dynamics due to their inherent thermal properties. Mechanical discrepancies also contribute to noise. Potential misalignment between the substrate and the orientation of the laser beam can lead to uneven energy deposition. Furthermore, vibrations from the movements of the Computer Numerical Control (CNC) machine might introduce transient noise sources, which could affect the stability of the melt pool.

2.1.3 Track formation

The final macro-process identified within DED-LB is track formation, often called solidification. This process emerges as a culmination of the previous two mechanisms: melt pool generation and material incorporation through the powder stream mechanism. Their synergistic actions determine the shape and composition of the melt pool. The interplay of parameters governing these two mechanisms, coupled with the influence of noise sources and the inherent physical and geometrical attributes of the selected materials, results in a specific temperature distribution within

the component. The latter establishes a corresponding thermal gradient, which, in turn, dictates the solidification rate of the track.

The intricate interrelations of these mechanisms dictate the resultant microstructure, residual stresses, and surface quality of the deposition. In both contemporary academic and modern industries, efforts are predominantly focused on enhancing the mechanical properties of depositions by adjusting process parameters and monitoring specific characteristics of the powder stream or the melt pool. The primary goals are often to minimize porosity, contain residual stresses, and enhance the surface quality of the depositions. To this end, parameter maps frequently employ the concept of energy density (E), calculated based on laser power (P), scan speed (v), and laser beam diameter (D):

$$E = \frac{P}{v \cdot D} \tag{2.1}$$

This metric is often used to predict relative porosity and finds utility in predicting layer height when used in conjunction with powder density (F), which is a metric derived from the powder mass flow rate (Q_p):

$$F = \frac{Q_p}{v \cdot D} \tag{2.2}$$

Finally, the Global Energy Density (GED) is a frequently cited parameter in the literature that relates the powder stream to the melt pool, defined as follows:

$$\text{GED} = \frac{P}{Q_p \cdot v \cdot D^2} \tag{2.3}$$

The latter incorporates the energy density (melt pool) and powder flow rate (powder stream), representing the energy introduced per unit mass added [37].

2.2 DED defects

As previously described, the outcome of deposition using the DED-LB technique encompasses three major mechanisms. The end product is a solidified metal part anchored to its substrate. Given that the process is imperfect and governed by intricate variables, the result often exhibits one or more defects, which can also be categorized into three main areas. The root cause of these imperfections frequently stems from one or multiple factors, process variables, or parameters. Consequently,

experimental methods are used to decipher ways to mitigate or eradicate such flaws. A detailed subdivision and classification of these defects is evident in the literature. The comprehensive categorization by Liu et al. [38] has been adopted for this discussion.

2.2.1 Geometrical Defects

In DED geometrical defects arise from discrepancies between the CAD model and the actual part produced, resulting in deviations in form and dimensions. Such deviations can compromise aesthetic quality and structural integrity, potentially rendering the part unsuitable. Here is an overview of common geometrical defects:

- **Non-uniform Layer Thickness:** variations in deposited layer thickness across the building height can result in discrepancies in the final size of the part;
- **Surface Warping:** deformed top surface, marked by peaks and valleys, typically results from high volumetric energy density input from the laser;
- **Edge Defects:** appear as uneven edges where the material overlays or underlays. Such inconsistencies often arise at deposition path starts or ends or during abrupt nozzle direction changes;
- **Satellite Defects:** localized balled-up protrusions; these defects primarily occur at overlap points between deposition start and endpoints.
- **Dilution and Dimensional Discrepancies:** this happens when metal is deposited onto a different material; the resultant bead or track might deviate in dimension due to material interactions. Factors like melt pool size and solidification times influence the extent of dilution;
- **Material Shrinkage:** contraction of the layers leading to slanted edges. This phenomenon affects the outer geometry, demands post-processing, and might resemble staircase defects indicative of poor resolution;
- **Base Separation and Warping:** excessive heat, sub-optimal scan strategies, or inadequate heat dissipation can cause the bottom layer to warp or detach from the substrate, rendering the part unviable.

2.2.2 Morphological Defects

Morphological defects in DED stem from irregularities in the surface features and internal quality of the fabricated component. Such irregularities can alter the interaction of the part with its environment and its mechanical response under loading conditions. Here is an overview of common morphological defects divided into two different groups.

Surface Morphological Defects

- **Surface Waviness:** deviation of the top surface from being planar, exhibiting a wavy nature;
- **Excessive Surface Roughness:** affected by the combination of process parameters and build orientation;
- **Blobs and Zits:** minor imperfections may appear on the surface, especially at the start or end of a scan path.

Bulk Morphological Defects

- **Porosity:** a diminished effective density of the material by gas entrapment;
- **Delamination and Lack of Adhesion:** unintentional separation of the part from its base or between successive layers;
- **Large Voids:** typically larger than gas or lack-of-fusion induced porosities.
- **Bulk Inclusions:** foreign particles or impurities inside the part;
- **Non-uniform Grain Morphology/Texture:** variations due to non-uniform thermal distributions and other factors;
- **Heat Affected Zones (HAZ):** Formed due to the scanning strategy and heating from successive layer deposits;
- **Unmelted Powder on Surface/Subsurface:** a powder that only partially fuses;

- **Incomplete Melting in Compositional Transition Layers:** issues due to differences in elemental composition.

2.2.3 Microstructural Defects

Microstructural defects in DED arise from variations in the minute composition and arrangement of constituents within materials. Such variations can affect the mechanical, thermal, and electrical properties of the produced part, often compromising its performance and longevity. Here is an overview of common microstructural defects grouped in two distinct type.

Feature-related Defects

- **Discoloration:** caused by overheating, differential cooling, and oxidation;
- **Microstructural Inhomogeneity:** variations in microstructure based on thermal history and cooling rate;
- **Inter-/Intra-layer Cracking:** cracks formed during the solidification of the melt pool;
- **Tensile Behavior Anisotropy:** primarily induced by grain anisotropy.

Composite-related Defects

- **Brittle Intermetallics:** formed due to the cooling rate and/or intended compositional blend;
- **Undesired Phases with Degraded Properties:** such as the brittle Laves phase or martensite;
- **Elemental Segregation:** influenced by temperature's effect on solid solution solubilities.

There exist numerous potential geometrical, morphological and microstructural defects in DED processes. The key to mitigating such defects is thoroughly understanding the process and optimizing process variables. Consistency and repeatability

across machines are paramount to ensuring high-quality and defect-free produced parts.

2.3 DED applications

DED offers a wide range of applications to meet various industrial needs. From the fabrication of new components to the enhancement and repair of existing ones, the flexibility and precision of DED make it an increasingly vital tool in contemporary manufacturing practices. This section outlines the principal uses of DED by dividing them into categories: Manufacturing, Repair and Remanufacturing, Coating, and Functionally Graded Materials. This categorization aims to comprehensively understand the capabilities and innovative potential associated with DED technology.

2.3.1 Manufacturing

As AM methodologies exemplify, DED distinguishes itself from traditional manufacturing avenues through its unparalleled flexibility and material efficiency [39]. In aerospace applications, this technology facilitates the fabrication of intricate geometries without requiring specialized moulds or casting tools [36]. Despite size-related challenges in construction applications, DED provides an opportunity for the engineered tailoring of compositional and microstructural gradients, potentially offering mechanical properties superior to conventionally manufactured components [40]. Moreover, DED holds promise for mitigating greenhouse gas emissions commonly associated with construction processes [41, 42].

Beyond efficiency and speed, DED technologies offer significant geometric latitude, enabling the manufacture of structures that are either unfeasible or economically restrictive when employing traditional manufacturing methodologies. Such AM methodologies, like Double-Wire Arc Additive Manufacturing (D-WAAM) , can significantly increase the strength of the material by up to 20 % and hardness by 9 % compared to standard Ti-6Al-4V components. Furthermore, the in situ alloying capabilities, as demonstrated by Han et al. [43] in their investigation of Ti6Al-4V-xCu alloys, enable material customization that was not possible through traditional manufacturing techniques. These material advantages are attributed to multiple factors, including reduction in grain size and intrinsic in situ alloying capabilities

(a) Prima Additive Ianus (b) Meltio cell (c) MX3D Metal XL

Fig. 2.4 Robotic DED cells

of AM technologies [44, 45]. DED offers highly customizable solutions within the biomedical sector, allowing adaptability in material composition and implant geometries [46].

Emerging hybrid manufacturing systems that combine additive and subtractive technologies offer potential solutions to inherent limitations of DED, such as residual stresses and surface finish quality. Integrating post-processing techniques into the manufacturing chain promises to improve productivity and market competitiveness [47]. Compared to other metal AM methods, a salient advantage and distinguishing feature of DED technology is its adaptability to various Computer Numerical Control (CNC) machines. This flexibility ranges from straightforward configurations to complex five-axis systems. Recent trends indicate that companies such as Prima Additive, Meltio, and MX3D are capitalizing on this versatility by integrating DED systems onto robotic arms and coupling these with rotary tables. This innovative approach further expands the number of axes, enhancing overall system flexibility. Illustrative examples of such robotic DED cells can be observed in Fig. 2.4a, showcasing the configuration proposed by Prima Additive, in Fig. 2.4b, the Meltio robot cell, and in Fig. 2.4c featuring the Metal XL from MX3D. It is worth noting that these three systems have been specifically chosen for discussion as they represent distinct subcategories within the broader realm of DED technology: Ianus operates on both powder and wire feedstock, thus categorized as DED-LB/Powder-Wire; Meltio utilizes wire feedstock and is categorized as DED-LB/Wire; and Metal XL from MX3D employs the WAAM technique. This adaptability manifests in both the complexity of achievable shapes and significantly expanded build volumes afforded by these systems. For instance, Ianus cell offers a build volume of $(1600 \times 1200 \times 700)\,\mathrm{mm}^3$, Meltio features a build volume of $(2000 \times 1000 \times 1000)\,\mathrm{mm}^3$, and Metal XL from MX3D boasts a build volume of $(2200 \times 1400 \times 1300)\,\mathrm{mm}^3$.

2.3.2 Repairing and Remanufacturing

A significant advantage of DED technology resides in its ability to repair components that experience loss of functionality over their operational life. During the design phase, considerations are made for the anticipated service life. Components are subjected to wear, breakage, or technological obsolescence as time progresses. Factors such as impacts, plastic deformation, corrosion, fatigue, and extended thermal cycles can induce defects, including cracks and wear.

Traditionally, the standard approach has been to replace the affected product. However, particularly for high-cost or frequently-replaced components, two alternative strategies emerge: repairing and remanufacturing. Both strategies aim to avoid full product replacement. Remanufacturing is used to restore used components to a "like new" state, while repairing targets components that do not meet product specifications, exhibit manufacturing-induced defects or have sustained minor damage [48]. In particular, remanufacturing requires comprehensive reconditioning, often involving subsequent post-DED operations such as milling and turning. DED is optimally suited for both repairing and remanufacturing, leveraging the specialized capabilities of AM techniques and the flexibility and/or speed of a CNC system capable of managing multiple axes simultaneously (see Fig. 2.5).

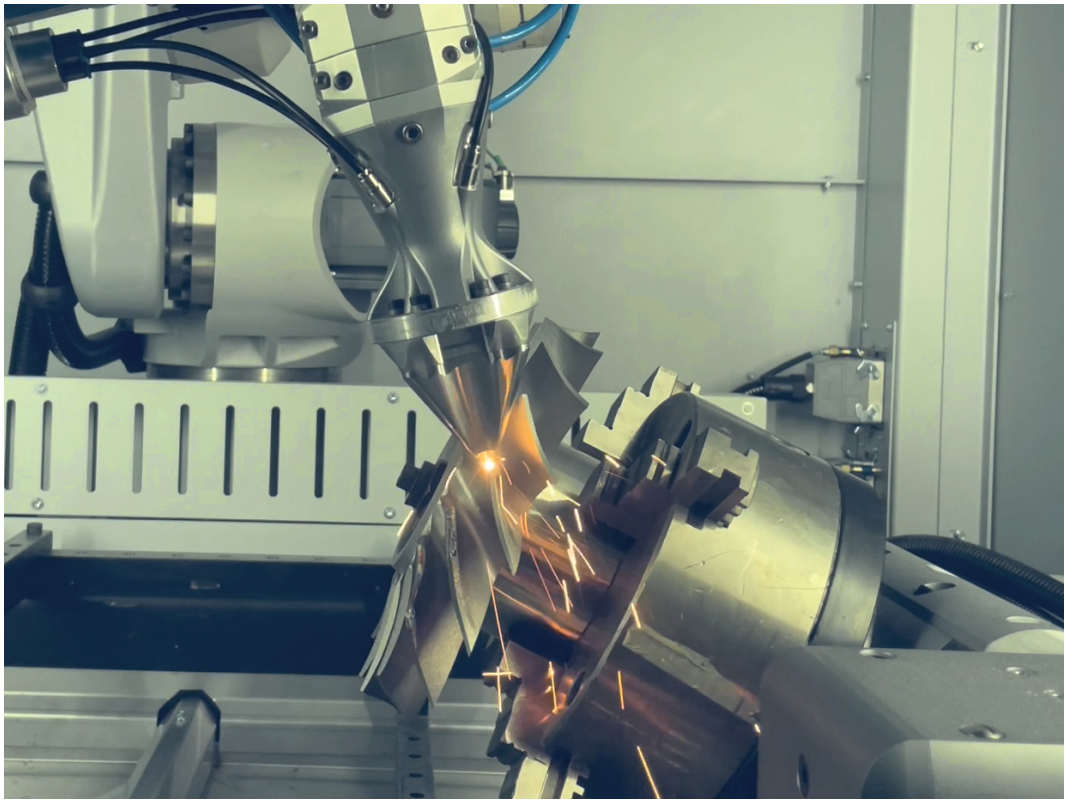

Fig. 2.5 Repairing process. Image credits Prima Additive [49]

The choice of repair rather than replacement can yield significant economic and environmental benefits. DED systems currently on the market can operate in large build volumes, outclassing other AM technologies. Some of these systems are integrated with chip removal systems, facilitating material deposition and removal. This dual functionality compensates for geometric and surface irregularities, ensuring precise control over layer growth on the Z-axis. Compliance with stringent mechanical robustness and hardness standards is imperative post-DED repair for specific components. The ASTM E8/E8M-21 standard often serves as a benchmark for tensile strength [50], while ASTM A370-20 is essential for steel components [51]. Hardness assessments generally adhere to the ASTM E384-22 standard [52]. It is critical to note that repaired components manifest a blended interface between the starting materials and newly added materials. As a result, testing protocols must adequately represent this hybrid zone [53]. Furthermore, since components undergoing repair or remanufacturing processes cannot be subjected to destructive tests, non-destructive testing (NDT) methods become highly relevant for characterizing different zones of the component.

Drawing in parallel with welding evaluation techniques, NDT methods such as industrial radiography or computed tomography (CT) scanning using X-rays or gamma rays, ultrasonic testing, liquid penetrant testing and magnetic particle inspection offer valuable insights. For example, a proper weld would reveal no cracks in radiographic tests, demonstrate the unobstructed passage of sound in ultrasonic tests, and show a clean surface in penetrant tests. Similarly, compliance with predefined welding parameters can be confirmed through real-time weld monitoring, ensuring the integrity of the weld prior to NDT and metallurgical evaluations. In recent years, there has been a growing adoption of nanoscale hardness tests. These are increasingly being employed to assess hardness and correlate these properties with the elastic response of the material, typically represented by Young's modulus [54]. Such advances in testing methods offer a more comprehensive understanding of material behavior, thereby enhancing the reliability of post-DED repair assessments.

The academic landscape abounds with studies exploring various dimensions of the reparative capabilities of DED. These scholarly contributions act as foundational pillars, illuminating the efficacy and adaptability of DED in a diverse array of material and operational contexts. For instance, a study by Sun et al. [55] investigates the implications of DED repair on AISI 4340 steel components, revealing intricate nuances of microstructural changes and their ensuing mechanical responses. Paydas et al. [56] focus on strategic choices during DED operations and their impact on the microstructural and hardness characteristics of the repaired Ti-6Al-4V components. Taken together, these academic insights underscore the versatile promise of DED in component repair, attesting to its potential for precision, adaptability, and quality assurance [53, 57].

2.3.3 Coating

DED processes offer significant advantages in the context of maintenance, repair, and maintenance applications by enabling the application of coatings to both original and damaged components. In forging tool applications, for example, a DED-bonded material can withstand thermal and fatigue loading without chipping [39]. Tools treated in this manner demonstrated up to four times greater longevity than those subjected to conventional treatments, resulting in considerable cost savings and minimized operational downtime. Moreover, DED has been employed to repair

components with complex geometries, such as impeller blades, extending the lifespan of critical machinery components.

DED processes are particularly beneficial for improving the surface properties of metallic parts through coatings. Several vital advantages characterize the DED technique in this application. Allows for a localized HAZ, thereby reducing thermal distortion. Moreover, computer-controlled laser scanning patterns enhance the reliability, repeatability, and flexibility of the coating process. Significantly, DED facilitates coating metallic parts with intricate geometries previously considered non-coatable using traditional methods [58]. The metallurgical bond between the coating layer and the part significantly strengthens and stabilizes the coating.

2.3.4 Functionally graded materials

DED technology enables the meticulous tailoring of specific attributes within localized regions of a component to optimize its functional characteristics and extend its operational longevity [59]. This fine-tuning can involve depositing varying materials or inducing compositional shifts within specific areas. Whether these modifications are intentional, manipulated by process parameters or accidental due to irregularities in the deposition, the result is a material with functionally graded properties, known as Functionally Graded Materials (FGM). In particular, the mechanical properties and in-vivo biocompatibility of porous Ti-6Al-4V scaffolds, a category of FGM, have been effectively optimized, as corroborated by numerous studies [60]. The generation of FGM by DED is accomplished through several techniques (see Fig. 2.6). The direct joining approach fuses Material A directly onto Material B, yet this method may induce internal stresses because of the abrupt change in material properties. An alternative method, the intermediate section technique, places a transitional layer of a third material, Material C, between Materials A and B to mitigate abrupt property alterations. The most sophisticated approach, the gradient path technique, crafts a transition region where the composition smoothly transitions from Material A to Material B, thereby reducing stress concentrations and potential failures [61].

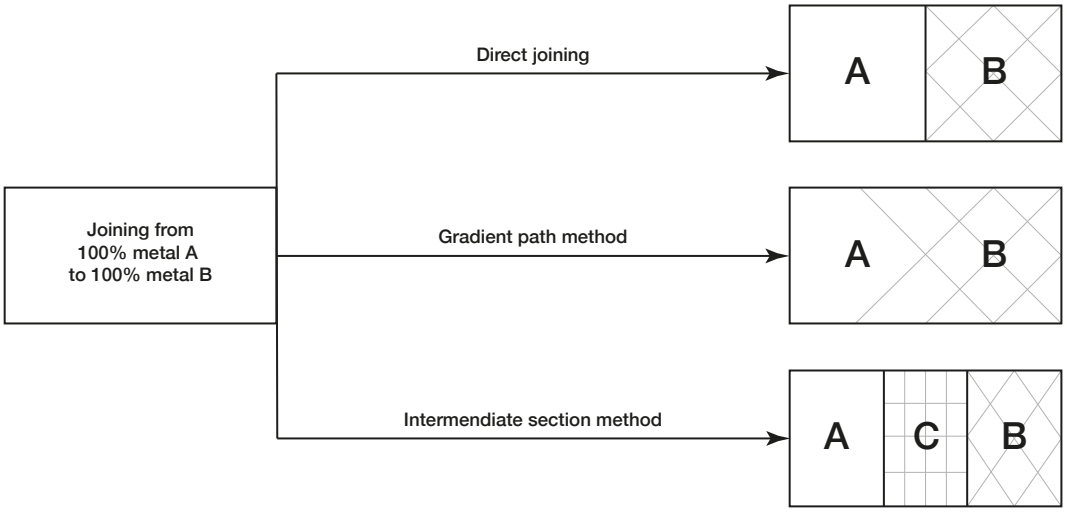

Fig. 2.6 Three FGM manufacturing strategies

The ability of DED to fabricate FGM proves especially valuable when materials with significantly different thermophysical properties need to be joined. Traditional joining methods often result in cracks that compromise performance [62]. In contrast, the DED process mitigates such challenges, enabling the creation of an alloy that incorporates the advantageous properties of its constituent materials.

Chapter 3

Overview of industrial experiments and the role of statistical methods

The dawn of the 20th century brought forth many scientific breakthroughs, and among them stood the pioneering contributions of Sir Ronald Fisher in the realm of industrial experimentation and statistical methods. Tasked with a complex challenge at the Rothamsted Experimental Station, now known as Rothamsted Research, Fisher faced the challenge of maximizing agricultural yield. His objective required testing an array of fertilizers in different quantities and at various application times throughout the year - an endeavor as simple in its intention as it was intricate in its execution.

The difficulties inherent in agricultural experimentation are manifold, with elongated timescales being a primary challenge. To put this into perspective, the duration from sowing to harvesting wheat spans up to eight months, depending on factors such as wheat variety and depending on environmental conditions [63]. Coupled with this is the need to manage multiple variables: a range of fertilizers, their respective doses, and the timing of their administration. Each of these components, when taken together, significantly amplified the complexity of the task at hand.

Navigating these complex waters, Fisher broke new ground by developing the Design of Experiments (DoE), adopting and developing factorial experiments, rather than experimenting with the less efficient one-factor-at-a-time (OFAT). This approach allowed for the concurrent exploration of multiple factors and their interrelationships. The latter marked a turning point in the efficiency and effectiveness of experimental design, drastically reducing the time and effort required to discern the factors influ-

encing yield and pinpoint the optimal conditions. During the Rothamsted period, Fisher also proposed and validated the Analysis of Variance (ANOVA). This statistical method allowed a more precise understanding of the effects and interactions of the factors considered [64].

Fisher's groundbreaking methodology revolutionized not just the field of agricultural research, but it prompted a paradigm shift across numerous other sectors. DoE, alongside ANOVA, became a fundamental component of agriculture experiments, industrial statistics, and finding applications in diverse fields such as manufacturing, health sciences, the pharmaceutical industry, and software engineering. Fig. 3.1 illustrates an application of this method in agriculture.

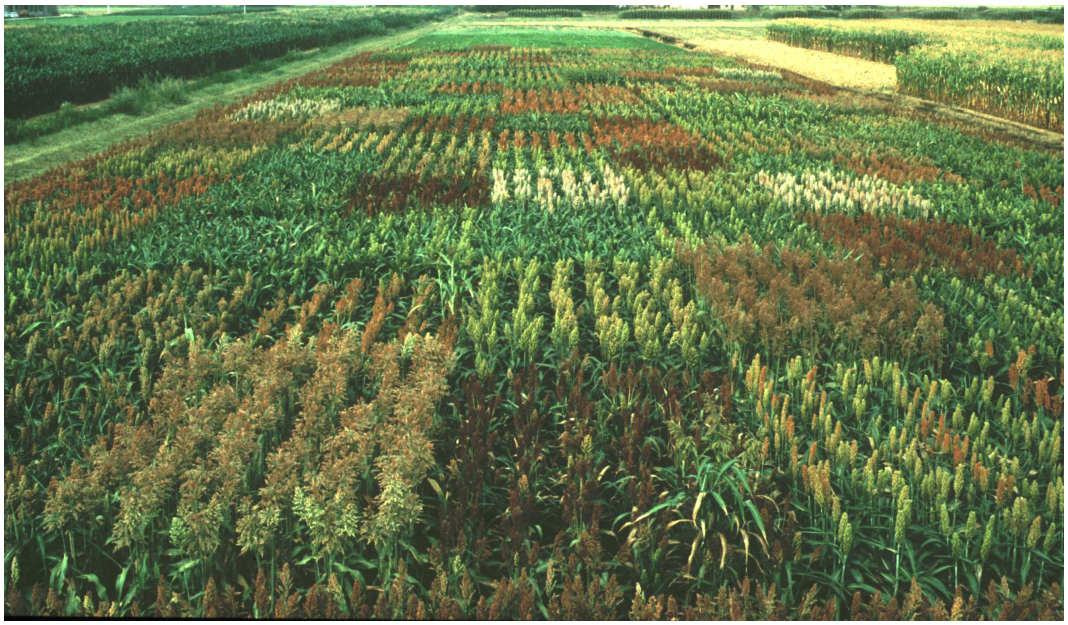

Fig. 3.1 An example of DoE in agriculture fields [65]

This chapter delves into essential topics to enhance comprehension of this thesis work, focusing on the role of industrial experimentation, specifically, the DoE and some basis of statistical methods. It presents critical components such as factorial designs, factor screening, and the response surface methodology, each vital for the application of DoE in AM.

3.1 Introduction to the utility of statistical methods in industrial settings

3.1.1 The deductive and inductive reasoning

Within the scope of scientific investigation, both inductive and deductive reasoning play a central role. Inductive reasoning, deriving from specific observations, seeks to make broader generalizations, whereas deductive reasoning starts with overarching theories, leading to specific conclusions. These modes of reasoning are seamlessly integrated into the scientific method. This method is the bedrock of contemporary research, rooted in the cyclical process of hypothesis formulation, prediction, experimentation, analysis, inference, hypothesis evaluation, and potential subsequent studies, as illustrated in Fig. 3.2.

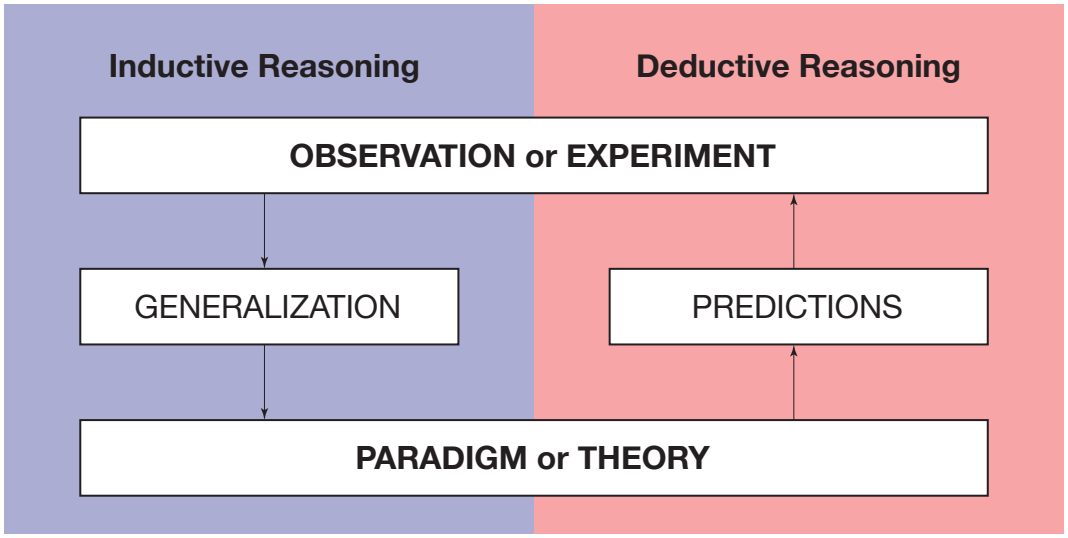

Fig. 3.2 Inductive reasoning process in the scientific method

The formulation of a research question is the first decisive step. Indeed, the research question is in the first chapter of this doctoral thesis. This question could emerge from observations that require an explanation or from finding solutions to open-ended queries. Existing evidence from previous experiments, scientific observations, and other scientists' work all shape the research formulation of the questions. The nature and quality of the question are pivotal as they directly influence the outcome of the investigation.

Hypothesis generation follows question formulation and is a conjecture that provides plausible explanations for observed phenomena. The hypothesis forms the basis for predictions, logical deductions made before knowing the outcome. If the results corroborate the predictions, the hypothesis receives preliminary support. The prediction process must distinguish the primary hypothesis from plausible alternatives, as similar predictions from different hypotheses do not provide exclusive evidence for either.

Testing encompasses the implementation of the experimental protocol, which should be articulated prior to test execution to prevent tampering and facilitate experiment reproducibility. During testing, the expected values derived from the hypotheses are compared to the actual experimental results, potentially leading to the hypothesis's validation or refutation.

Following the experimentation phase, a comprehensive analysis is performed. The latter evaluates the outcomes from the experimental results, interpreting and making sense of the collected data. The conclusions drawn from this analysis provide insights into the phenomenon under investigation and guide the subsequent steps of the investigation.

During this analytical phase, especially in cases of repeated experiments or large data sets, the use of statistical analyses becomes crucial. The application of statistical methods helps to ensure the validity and reliability of the results, allowing for a more nuanced understanding of the experimental data. These methods can identify patterns, trends, and correlations, providing a robust way to test the original hypotheses. Furthermore, they allow for estimating the degree of uncertainty or variability in the results, which is crucial in any scientific investigation. This rigorous analytical process is integral to strengthening or challenging the initial hypotheses, ultimately shaping the direction of future studies and experiments.

3.1.2 Occam's razor principle

Occam's razor is a philosophical and methodological guideline suggesting that the simplest one should be preferred when multiple hypotheses offer potential explanations for a phenomenon. This principle is not about the certainty that the simplest hypothesis is correct, but about its testability and practical efficiency.

"Pluralitas non est ponenda sine necessitate"

In the research landscape, the principle of Occam's Razor is a cornerstone, underpinning the formulation of theories and models that balance simplicity and effectiveness, hence curbing unnecessary complexity. This principle is widely used in numerical methods, where the challenge often lies in choosing the right degree of simplicity or complexity in a model. Rooted in the fundamentals of probability theory, Occam's razor finds its rationale. Each assumption within a model introduces potential avenues of error. Should an assumption not contribute to the model's precision, it merely amplifies the likelihood that the theory could be incorrect.

While the principle of Occam's razor directs the research towards a path of simplicity, it is crucial to understand that the claim for simplicity should not be overused. Indeed, if we were to simplify excessively, it would hinder our ability to explain complex phenomena such as non-linear ones [66]. The delicate balance of simplicity and complexity is eloquently encapsulated in Albert Einstein's quote:

"Everything should be as simple as it can be, but not simpler"

Furthermore, in the context of this work, a dual strategy has been adopted, entailing the adoption of simplicity for clarity of understanding while recognizing the necessity for complexity in explicating more complex phenomena. This equilibrium between simplicity and complexity has been integral to this research, ensuring the robustness and significance of the models and theories developed.

3.2 Basic Principles of Industrial Experimentation

Within the experimental design environment, a triad of fundamental principles commands significant attention, namely randomization, replication, and blocking. These principles, which embody the foundation of robust experimental methodologies, indisputably contribute to establishing the validity and reliability of experimental results.

To illustrate the concept of randomization, one might liken it to the rules of poker tournaments. The deck must be shuffled at the beginning of each hand. This shuffling process ensures randomness and fairness, blocking any potential advantage that could

be gained from observing previous hands or counting cards. The connection between these two contexts is aptly summarized by Sir R. Fisher, who famously stated:

"Designing an experiment is like gambling with the devil: only a random strategy can defeat all his gambling systems"

This comparison highlights the fundamental importance of randomness as a strategy that maintains integrity and defeats all bias systems in experimental design and poker. Randomization is the assignment of experimental material and the determination of the order of individual experiments at random rather than in a precise sequence. The latter helps ensure that observations are independent, which is crucial for accurate statistical analysis. By eliminating the influence of outside factors that could skew results, randomization ensures that the requirement for independently distributed random variables is met. While some experimental scenarios may pose challenges for implementing certain aspects of randomization, a comprehensive approach ensures that each unit has an equal chance of encountering interference, thereby reducing the risk of confounding effects.

"The three R of experimenters are:
Replication, Replication, Replication!" J. Andrews

Replication refers to the independent repetition of each factor combination in an experiment. This principle allows for estimating the experimental error and provides a basic unit of measurement to determine if observed differences are statistically significant. Replication also facilitates a more precise estimate of parameters, such as the mean response for one of the factor levels. For a valid experiment, measurements should be conducted in more than one experimental unit. Replication demonstrates the reproducibility of the measure, ensures that any intrusions affecting a single experimental unit do not cause significant bias, assesses the precision of the experiment by measuring the variability among replicates, and increases the precision of the experiment.

"Block what you can, randomize what you can't" G. Box

Blocking, an essential method in experimental design, refines the accuracy of comparisons by controlling nuisance factors. Creating homogeneous blocks where

these factors are constant enables an unbiased evaluation. This approach uses blocking to neutralize significant nuisance influences, with randomization managing the rest, thereby improving the estimation accuracy of effects, even amidst uncontrollable factors like environmental conditions and material variations. Organizing comparisons within these blocks optimizes outcomes, yielding valuable insights into the impact of influential factors [67].

3.2.1 Implementing a structured approach for designing industrial experiments

Experiments can be used to improve productivity and quality or reduce costs, but these problems can be more complex and multifaceted than they seem. Designing and conducting industrial experiments requires a meticulous and structured approach. This section delineates a seven-step procedure for effectively planning, conducting, and analyzing industrial experiments. Adherence to this methodology ensures reliable results and optimizes the use of invested resources. This procedure has been strictly followed in the work presented in this thesis to avoid wasting resources and time and ensure consistent and reliable results.

The initial step in conducting an industrial experiment involves identifying and defining the problem to be studied as a basic requirement of inductive reasoning. This stage may not be as straightforward as it seems, as it requires discerning when a situation necessitates an experimental approach. Formulating clear and specific questions that the experiment aims to answer contributes to the overall clarity of the experimental objectives.

The second step is the selection of the right response variable. The latter is crucial to the experimental process and should provide meaningful and useful information about the process being studied, often represented by a number, for example, the average or standard deviation of the measured characteristic. Consideration should be given to the capability of the gauge or measurement system, as inadequate capability can limit the detection of process effects on the response.

The third step involves choosing the factors that could influence the process or the performance of the system. The selection of factors to include also necessitates determining the range or region of interest for each, which may adjust as the experiment progresses and more information is learned about the critical variables. An

iterative process of reviewing and selecting factors often leads to the most effective experimental design. At this point, the pre-experimental planning procedure ends, and considerations and choices made from now on will irreversibly affect the outcome of the experiment:

"To consult the statistician after an experiment is finished is often merely to ask him to conduct a post mortem examination.
He can perhaps say what the experiment died of" Sir R. Fisher

The fourth stage strongly depends on prior considerations about the response to be measured, like the number of factors and levels, available resources such as feedstock materials, time, specialized workforce, tools for production and measurement procedures. These resources can include feedstock materials, time, specialized personnel, and production and measurement tools. Based on these considerations, the specimens for production are selected. This selection is driven by raw material availability, the most suitable experimental design, and the required number of replications to achieve a specific outcome. The latter is often gauged by the statistical power of the experiment, which is related to the Type II error.

The fifth stage is the execution of the experiment. The latter includes monitoring the process to ensure adherence to the plan, checking factor settings before each run, and anticipating potential mistakes, especially human errors.

The sixth stage exploits the data analysis collected using appropriate statistical methods, providing objective rather than judgment-based conclusions. Hypothesis testing and confidence interval estimation procedures can provide insights into the experimental data, helping to formulate empirical models representing the relationship between the response and the important design factors.

The seventh, but not always the last part, stage requires the intervention and critical judgment of the experimenter who followed the entire process necessary to conclude the analyses. It is decided to conclude the experiment, expand and replicate the plan, or change the assumptions or the initial procedures.

The process is iterative and requires adaptation as new information is gathered. This suggests that designing an experiment is part of a continuous learning process. Importantly, it should be noted that the bulk of the effort (approximately 80 %) is typically invested in the first four steps. In comparison, the remaining stages require about 20 % of the time, granted the preliminary stages were meticulously planned

and executed. The goal is to conduct a well-designed experiment that efficiently uses resources and yields reliable results.

3.2.2 Comparisons

In the fifth stage of industrial experiments, the experimentation and response acquisition phase, the focus is on recording response changes with precise, repeatable, and reliable procedures. The act of measurement in engineering is fundamentally a comparison, wherein a numerical value is assigned to a quantity by comparing it with a conventionally chosen known as the unit of measure. This process is realized through a measurement system designed to quantify physical variables allowing a degree of precision unattainable by unaided human observation. The preferred methodology for evaluating and expressing uncertainty should be globally applicable, internally consistent, transferable, and provide a realistic confidence interval for the measurement result [68].

Industrial experiments aim to determine if there is a significant change in response as a factor changes. For example, in a study involving DED-LB, a pivotal aspect could be ascertaining whether the mechanical properties of manufactured parts vary based on changes in the composition of the employed metal powder. In the analysis procedure, which represents the sixth stage of experimentation, a model is adopted to compare the data objectively. This process begins with formulating the null hypothesis (H_0) and the alternative hypothesis (H_1). The H_0 proposes no differences in the responses, implying they can be assumed equal. In contrast, the alternative hypothesis posits that the responses cannot be assumed equal. These hypotheses are then tested using a statistic at a specified significance level (SL). For our case, the samples must be independent and randomly selected. In hypothesis testing, two types of errors may be committed:

- Type I Error (α), where the null hypothesis is rejected despite being true;
- Type II Error (β) where the null hypothesis is not rejected despite being false.

An essential metric often used is the power of the test. The latter is defined as $1-\beta$; the power of a test represents the likelihood of correctly rejecting the null hypothesis when it is indeed incorrect [69].

In this context, comprehending the diversity of approaches to assess the hypothesis becomes essential. These methods are pivotal in affirming or negating the foundational assumptions of models. These tests provide an objective outcome, offering indispensable support in interpreting the results of an experimental study. Therefore, these methodologies aid in statistical reasoning and fuel informed decision-making based on experimental findings. It is worth mentioning here a few prominent tests:

- ***Z*-test:** applied when the data distribution approximates a normal distribution, and the population variance and standard deviation are known. It should be noted, however, that the Central Limit Theorem allows for applying the Z-test even when the population variance is unknown, provided the sample size is sufficiently large.

- ***t*-test:** typically employed when the data exhibits a normal distribution, but the population variance remains unknown. Various forms of the t-test exist, such as the independent t-test and the paired t-test, each with unique assumptions and applicability. For large sample sizes, the requirement for normal distribution may be relaxed.

- **χ^2-test:** contrary to a common misconception, the χ^2-test test is not strictly non-parametric. Instead, it is a distributional test commonly used for evaluating categorical variables. Different variants of the χ^2-test test may have specific distributional requirements.

- **Analysis of Variance (ANOVA):** utilized for comparing the means across more than two groups, ANOVA operates under the assumption that the data are sampled from normally distributed populations and that the variances of these populations are equal, an assumption known as homoscedasticity.

- ***F*-test:** used to compare variances across two distinct populations, the F-test also makes underlying assumptions about the data. These include the assumptions of normality and homoscedasticity, similar to the ANOVA.

While these methods provide a concrete foundation for statistical analysis, it should be noted that this brief exposition needs to delve into the mathematical intricacies of these procedures. Instead, the objective here is to offer an overview, arming the reader with a basic understanding of the tools available for statistical analysis and the scenarios where each could be most effectively applied. The choice

of test is contingent on the nature of the data and the specific questions the research aims to answer. Despite the complexities these tests entail, their proper use can provide invaluable insights, facilitating an improved understanding of the studied phenomena. In this thesis work, the *t*-test, ANOVA, and ANCOVA have been extensively utilized. Therefore, additional details on these specific tests have been provided in Appendix A for the reader's benefit.

3.3 Factorial designs

Factorial designs originated from the ideas of Gilbert and Lawes, serving as an alternative to the commonly used OFAT approach. However, Fisher first recognized and fully exploited their potential, especially in agriculture. Compared to OFAT designs, factorial designs offer a more comprehensive, precise, and reliable view of how the response reacts to stimuli (factors) given an equivalent number of tests when two or more factors are under investigation.

"No aphorism is more frequently repeated in connection with field trials, than that we must ask Nature few questions, or, ideally, one question, at a time. The writer is convinced that this view is wholly mistaken.
Nature, he suggests, will best respond to a logical and carefully thought out questionnaire; indeed, if we ask her a single question, she will often refuse to answer until some other topic has been discussed" Sir R. Fisher

From Fisher's perspective, the system, which could be Nature in agriculture, is interrogated via a factorial design approach. The responses elicited by the system are subsequently scrutinized through statistical testing. Factorial designs confer multiple benefits, including orthogonality - a vital precondition for fractionation and blocking. Moreover, it facilitates estimating effects (with the associated errors) and evaluating interactions between factors, a crucial aspect not assessable with OFAT designs. Various design types have been advanced, providing a wide array of choices. With the assistance of software packages like R, JMP, and Minitab, it is feasible to construct designs optimally fitted to the particular case under examination. This work will initially focus on a 2^2 design, the simpler version of the 2^k designs, to facilitate a more comprehensive understanding before transitioning to broader cases.

The 2^2 full factorial design is particularly suited for systems influenced by two specific factors, named A and B. Within this framework, both factors are systematically explored at two levels ("low" and "high" or "$-$" and "$+$"). For the sake of calculations within the design, the factors are systematically scaled, assigning the low level a value of -1, and the high level a corresponding value of $+1$ (coded values). By deploying a mere four experimental conditions, this design enables an incisive investigation of the main effects of factors A and B and their interaction (AB). The capital letters represent these effects: A for the first factor influence, B for the second, and AB for their interaction. The average effect of a factor is determined by analyzing the alteration in response caused by a change in that factor's level, considering the impact of other influencing factors. Through the Fisher-Yates notation [70], specific symbols represent the summation of response observations across all replicates for particular combinations of treatment levels.

The standard order and notation (1), a, b, and ab signify these totals, reflecting the relationships between factors and their levels, making it easier to calculate effects and interactions within the experimental framework. This can be summarized in the design matrix as shown in the Table 3.1. By utilizing the columns of the table,

Table 3.1 Matrix Model

St. Order	Treatment	Effect		
		A	B	AB
1	(1)	-1	-1	+1
2	a	+1	-1	-1
3	b	-1	+1	-1
4	ab	+1	+1	+1

the main effects can be calculated quite simply. Indeed, the contrasts are obtained through the dot product between the treatment columns and the various effects, including both main and interaction effects. The resulting values provide the main effects by dividing these contrasts by $2n$, where n is the replication. For example, to estimate the main effect of A:

$$A = \frac{1}{2n}\{[a-(1)]+[ab-b]\} \tag{3.1}$$

The same procedure can be used for B:

$$B = \frac{1}{2n}\{[b-(1)]+[ab-a]\} \tag{3.2}$$

and finally, for the interaction:

$$AB = \frac{1}{2n}\{[ab-b]+[a-(1)]\} \tag{3.3}$$

As depicted in Fig. 3.3, the difference in average responses between the right and left sides of the square gauges the effect of factor A. In contrast, the effect of factor B is calculated by the difference between the top and bottom averages. The interaction effect AB is determined by contrasting the average of the right-to-left diagonal combinations with the left-to-right diagonal ones within the square.

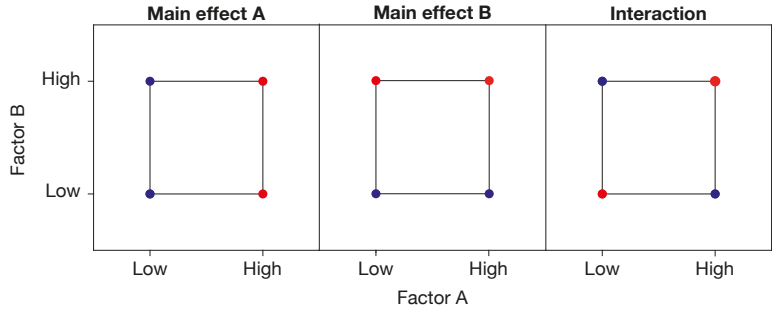

Fig. 3.3 Effects estimation

The contrast (or equally the effects) are precious for assessing the direction and magnitude of the factors, yet ANOVA must support them. The latter provides the significance of the factors in the investigated process. Specifically, calculating the SS for all the terms involved in the model is essential. These can be utilized to obtain the MS, which enable the performance of the F-test. Due to its orthogonality properties, SS estimation becomes particularly easy for factorial design:

$$\begin{aligned} \mathrm{SS_A} \frac{(\mathrm{Contrast_A})^2}{4n} \\ \mathrm{SS_B} = \frac{(\mathrm{Contrast_B})^2}{4n} \\ \mathrm{SS_{AB}} = \frac{(\mathrm{Contrast_{AB}})^2}{4n} \end{aligned} \tag{3.4}$$

Thus, one can obtain the SS_{Error} by calculating the SS_{Total} derived from the summation of the difference of each squared observation minus the total mean squared. This is the fundamental principle of ANOVA, namely, to decompose the variability into various parts and compare them:

$$SS_{Error} = SS_{Total} - SS_{Model} = SS_{Total} - (SS_A + SS_B + SS_{AB}) \tag{3.5}$$

where SS_{Model} is the SS of the model. After calculating the SS, representing the total variability within the data, it is possible to derive the ME for further analysis. The ANOVA method is then employed to dissect this total variability into distinct components, specifically differentiating between the variability between treatments and the variability within treatments. The F statistic is central to this process, and it is computed as the ratio of the mean square for the factor (representing the variability between treatments) to the MS_{Error}. Following an F distribution, the critical F value (upper tail) for α is identified for both the main effects and the interaction. This value is determined based on the degrees of freedom associated with each source of variation. This value aids in assessing the analysis, highlighting the significant factors that influence the process under investigation.

3.3.1 Coded variables

In factorial design analyses, the employment of coded design variables, typically confined between -1 and +1, is favored over natural or engineering units. This preference is grounded in the following:

- **Enhanced Interpretability:** Utilizing coded variables often yields heightened clarity and interpretability compared to original units.
- **Orthogonality & Comparative Precision:** Coded designs ensure orthogonality of variables. Such an arrangement allows for the uniform estimation of model coefficients, rendering them directly comparable. These dimensionless coefficients signify the effect of a unitary change in the respective design factor, facilitating the determination of relative effect magnitudes [71].

Transitioning between coded and uncoded designs can be swiftly accomplished through straightforward algebraic procedures.

3.3.2 Evaluation of model adequacy

Upon implementing factorial designs, a subsequent inquiry arises into the goodness of the derived model to empirical observations. Several metrics have been established to facilitate a rigorous evaluation of this fidelity. Foremost among these is the Coefficient of Determination (R^2), which quantifies the proportion of the total variability in the observed data accounted for by the model. Although a value approaching 1 indicates an optimal representation, caution is advised in models with increased complexity due to including numerous predictors. For this reason, the Adjusted R^2 has been introduced. As models grow intricate with the addition of predictors, the risk of overfitting becomes more prevalent.

$R^2(adj)$ compensates for this by adjusting for the number of predictors, thereby providing a more nuanced model fidelity assessment. However, the adequacy of a model is only partially contingent on its performance with familiar datasets. The model's capacity to predict unseen data is of paramount importance. In this realm, the Predicted $R^2(adj)$ and the concept of predicted residual error sum of squares (PRESS) are utilized. $R^2(pred)$ offers a projection of the variance the model may account for in novel contexts, with deviations from R^2 serving as indicators of its predictive robustness [72].

In addition to the metrics mentioned above, the Standard Deviation and the Coefficient of Variation (CV) are also employed. The former offers a measure of the dispersion of residuals, while the latter compares unexplained variability to the mean of the response variable, thereby providing insights into potential model inadequacies. Furthermore, the residuals, which are the discrepancies between observed and predicted values, warrant analysis. Within the scope of Residual Analysis, many techniques find their relevance. Notably, the inspection of histograms of residuals serves as a preliminary tool to discern their normality. Should the histogram depict a semblance to a normal distribution centered around zero, it suggests the plausibility of the normality assumption.

However, it is also recognized that normality determination through such a method may introduce uncertainty for smaller sample sizes. This shortcoming is mitigated by resorting to a normal probability plot of residuals. A linearity in this plot accentuates the likelihood of residuals following a normal distribution. Moreover, the issue of outliers must be relegated to more than mere footnotes. Outliers,

or values that diverge significantly from others can exert undue influence on an analysis, potentially skewing outcomes and inferences. The genesis of these outliers could range from computational inaccuracies to unique experimental circumstances. Methodologies such as examining studentized residuals emerge as potent tools in this regard. When most of these residuals lie within three standard deviations from zero, those defying this range are flagged as potential outliers and must be treated as it (discarded or fitted).

The homogeneity of variances across groups is another pillar that demands scrutiny. Non-uniform variances can mandate corrective measures, which might encompass data transformations. Furthermore, an imbalance in sample sizes across groups might introduce complexities, notably if one group demonstrates a vastly distinct variance [73].

In conclusion, while factorial design is an essential methodological approach in experimental settings, its efficacy is augmented when complemented with rigorous evaluation of model adequacy. The overarching objective remains to construct both explanative and predictive models, mirroring the complexities of empirical observations.

3.4 Introduction to factor screening

In modern manufacturing, where resources are limited or associated with high costs, efficient experimentation is mandatory. Before advancing into the optimization realm, it is imperative to delineate the problem in question rigorously. A thoroughly defined problem is a cornerstone for ensuing experimental procedures, ensuring the efficient deployment of resources. Notably, while there is an inclination towards gradient-based methods in optimization endeavors, it must be acknowledged that these methods often operate within a pre-specified process parameter window. Indeed, to achieve global optimization, it often becomes imperative to search outside this predefined boundary; otherwise, there is the inherent risk of settling for suboptimal solutions or becoming trapped in local optima. Several strategic methodologies, such as simulated annealing, genetic algorithms, and momentum-based gradient descent, have been devised to circumvent these challenges, drawing upon principles from probability, evolutionary biology, and physics, respectively [74].

When transitioning from numerical (algorithmic) optimization to experimental setups, a distinct perspective arises. Owing to the intrinsic variability and unpredictability inherent in empirical data, these models work as mere approximations, accentuating the robust design experimentation indispensability. Factor screening designs, in this milieu, play an instrumental role. Their cardinal objective is to discern and categorically isolate factors significantly impacting the response. By meticulously categorizing these influential input, practitioners can strategically allocate resources to the domains most significantly affecting the response. The array of factor screening designs available encompasses [75]:

- **2-level Fractional Factorial Designs:** primarily focused on linear terms, these designs cater to a limited factor count, ensuring efficiency with fewer runs.
- **Plackett-Burman Designs:** tailored for scenarios demanding analysis of many factors, these designs emphasize linear terms. They manage to strike a balance between exhaustive factor study and resource efficiency.
- **Definitive Screening Designs:** when a more intricate understanding, encompassing quadratic terms and two-way interactions, is desired, these designs are the go-to. They provide comprehensive insight into the process, capturing the complex relationships between factors and responses.

In this work, specialized designs have been utilized to address specific challenges. Subsequent sections will detail these methodologies, enabling a clear understanding of their application and relevance to the research.

3.4.1 Aliasing

Fractional factorial designs and blocking principles are pivotal in screening experiments to identify factors with pronounced effects amidst many under consideration. These experiments are generally conducted in the early stages of a project when numerous initial factors under investigation exhibit minimal or no effect on the response. Following identification, factors with significant impacts are subjected to further detailed examination in subsequent experiments.

The projective properties of factorial design play a core role in this strategy. They come into play mainly when certain factors exhibit negligible or null effects.

The projection property enables collapsing a larger factorial design into multiple smaller ones, thus economizing resources without sacrificing analytical accuracy. For instance, a single replication of a 2^k factorial design can be transformed into two replications of a 2^{k-1} factorial design or even four replications of a 2^{k-2}. The sparsity of effects principle supports the strategy, suggesting that the process or system is governed mainly by main effects and low-order interactions among several variables [76]. Therefore, less than half of the effects are expected to be active. The advantage of factorial designs increases with the number of factors, notwithstanding potential challenges linked to the growing number of trials. Furthermore, these designs are instrumental in sequential experimentation. Combinations of runs from two (or more) fractional factorials can progressively construct a larger design, enabling estimation of the factor effects and interactions of interest.

Throughout the application of these designs, the concept of aliasing remains crucial. This phenomenon arises when the effect of one factor, or an interaction, is indistinguishable from another due to the structural design. As fractional factorial designs test only some possible combinations, some effects become confounded or aliased with others, which may lead to information loss and complications in interpretation. Also, the blocking strategy is utilized to address the aliasing issue and enhance trial uniformity. Despite the challenges and costs associated with blocking, it effectively distributes contrasts for various estimates across blocks. Finally, the resolution of a design serves as a measure of the extent of aliasing present. For instance, resolution III designs exhibit aliasing between main effects and two-factor interactions. Conversely, in resolution IV designs, the main effects are free from aliasing, though two-factor interactions may still be confounded. Consequently, with their reduced aliasing, higher-resolution designs become desirable as the degree of fractionation permits.

3.4.2 Single Replicates design in factor screening

The experimental design choice becomes crucial in factor screening experiments. Factorial designs of type 2^k have their treatment combinations grow exponentially with increasing factors. The latter can impose a significant challenge, especially when resources are constrained. As a pragmatic solution, single replicates of 2k designs emerge as a viable alternative to fractional designs. Though both designs have limitations, the single replicate strategy retains many of the desirable properties

of the full factorial design, with the added benefit of being more resource efficient. Furthermore, these designs can be reproduced, collapsed, extended, and augmented with a center point for enhanced error estimation. Given the inherent uncertainty in ensuring minimal experimental error in such scenarios, aggressively spreading out the factor levels is prudent. This tactic aims to mitigate the risk of capturing noise rather than genuine effects (see Fig. 3.4), especially in fluctuating responses.

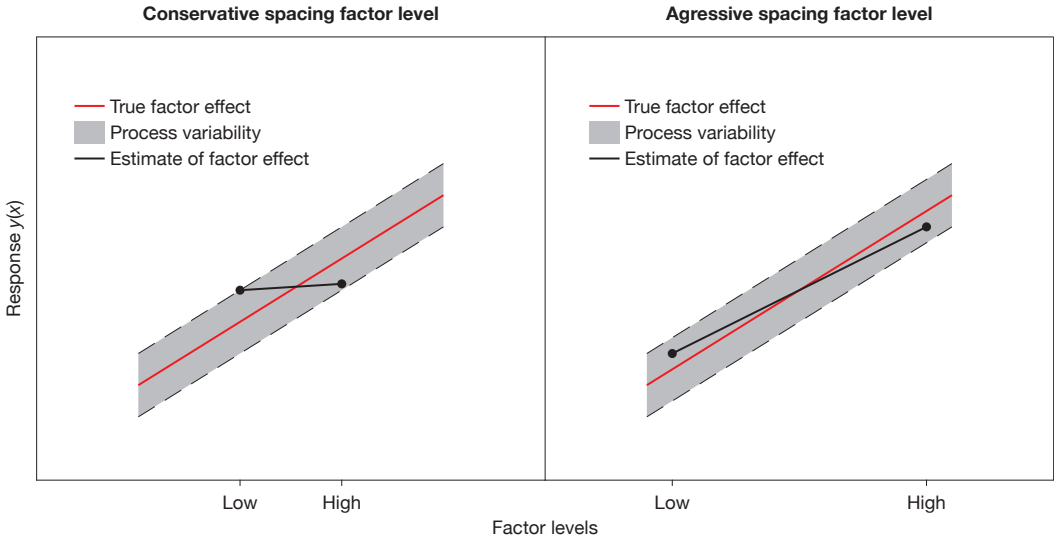

Fig. 3.4 The influence of selecting factor levels in a non-replicated design. Image adapted from [71]

Methods like examining the normal probability plot of effect estimates have been advocated to ensure interpretation precision [77]. Additionally, Lenth's method has been recognized for its effectiveness and ease of implementation in analyzing unreplicated designs [71]. Although replications stand as a cornerstone in the DoE, these specific designs prove invaluable when navigating research with limited or prohibitive resources, ensuring the advantages of factorial designs remain uncompromised.

3.4.3 Addition of central points

In 2^k factorial designs inherently assumes the linearity of factor effects. While interaction terms might be incorporated to represent some response curvature, there are scenarios where a second-order model might be more apt. To safeguard against

second-order curvatures and obtain an independent error estimation, central points can be introduced into the 2^k design. These points do not impact the typical 2^k effect estimates. For instance, a discrepancy between the means of the factorial and central points might allude to quadratic curvature. If detected, the design can be augmented with axial runs, leading to the so-called central composite design (CCD), primed for fitting a second-order model across various factors. Critical considerations for central point employment encompass:

- Utilizing ongoing operational conditions as the central point in ongoing experiments;
- Validating the congruency of central point responses with historically observed responses;
- The non-random sequencing of central point replicates to ascertain process stability;
- Employing central points to evaluate variability in experiments with unknown process variability;
- Applying central points in scenarios with both quantitative and qualitative factors.

3.4.4 Determining the appropriate sample size in experimental designs

In experimental design, the critical decision revolves around determining the appropriate sample size (n), which essentially dictates the number of replicates to be undertaken. An experimenter's objective to discern specific magnitudes of effects largely influences this choice. As highlighted in Fig. 3.5, aiming to detect smaller effects inevitably escalates the overall experimentation cost.

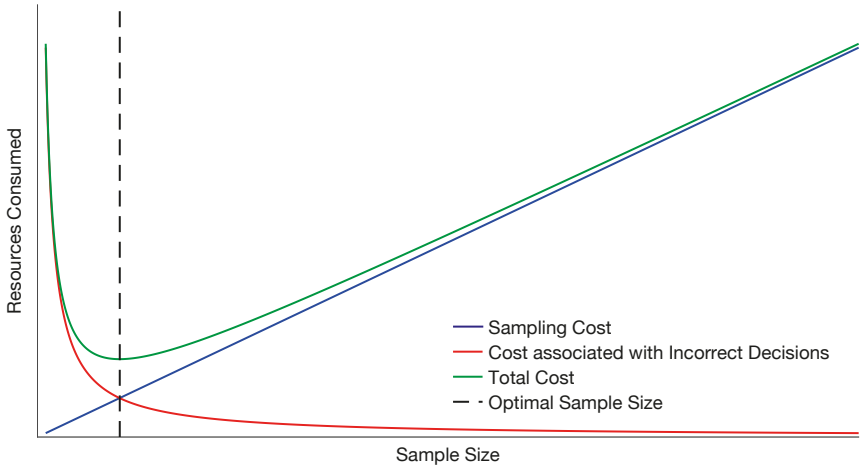

Fig. 3.5 Cost vs. sample size. Image adapted from [78]

The Operating Characteristic (OC) curve offers a graphical representation of Type II error probability against a variable indicating the deviation from the null hypothesis. In contrast, the Power Curve maps out the strength $(1-\beta)$ of the test concerning this same parameter. Modern software tools enable the seamless creation of these curves, acting as invaluable aids for experimenters. Such tools guide them towards selecting an optimal number of replicates, ensuring the design is tuned to discern potential critical differences in treatments. Selecting the right sample size is influenced by multiple factors:

- **Effect Size (ES):** While this is intrinsically problem-specific, a common benchmark for experimenters is to detect effects that are double the error standard deviation, often referred to as a *Huge* ES [79];
- **Power of the Test:** While the desirable power is dictated by the specific scenario, achieving a power of at least 0.80 or 80 % is a widely accepted benchmark [71];
- **SL:** This parameter sets the threshold for the risk associated with incorrectly rejecting the null hypothesis.

In scenarios like screening experiments, the ramifications of a Type I error (wrongly marking a factor as influential) are typically more benign than those of a Type II error (missing out on an impactful factor). Consequently, experimenters are often willing to accept elevated Type I error rates. When traditional metrics like standard deviation

remain unknown (often due to resource constraints or financial considerations), Cohen's relative ES becomes a pivotal tool in determining sample size. To bolster the accuracy of this approach and sidestep potential pitfalls associated with solely relying on Cohen's method, Mathews suggests employing a composite method strategy for sample size estimation [78].

In screening experiments, the consequences of committing a Type I error, which involves incorrectly identifying a factor as active when it is not, are often less significant than committing a Type II error, where an active factor goes undetected. An erroneously identified active factor can typically be rectified in subsequent research, rendering the repercussions of such a Type I error relatively minimal. In contrast, overlooking an active factor can lead to more severe complications, as the omitted factor may never be reconsidered in future investigations. Consequently, within the context of screening experiments, higher Type I error rates, such as 0.10 or 0.20, are sometimes deemed acceptable by researchers [71].

3.5 Response surface methodology

The Response Surface Methodology (RSM), a confluence of mathematical and statistical techniques, has been meticulously designed to optimize, develop, and enhance processes. Rooted in the pioneering work of G. Box and K. Wilson in 1951 [80], this methodology emerged as an invaluable tool in product development. With the advent of modern computers, RSM has garnered increasing prominence within the contemporary industry. The computational prowess of modern-day computer systems has facilitated the full exploitation of RSM capabilities. Notably, these advances have empowered the visualization of the response surfaces in two and three-dimensional spaces, thereby revolutionizing the understanding of complex processes.

The efficacy RSM in addressing various challenges is well-recognized within the academic and industrial spheres. Traditionally, the issues it addresses can be delineated into three primary domains. Firstly, RSM assists in drafting and charting a response surface over a specific region of particular relevance or interest. Secondly, it serves as a crucial tool in the pursuit of response optimization, pinpointing conditions that maximize, minimize, or target the response. Lastly, RSM facilitates the meticulous selection of operating conditions, especially when there is a necessity to

consider multiple responses concurrently. This multifaceted approach ensures that the methodology remains pertinent across many industrial applications.

3.5.1 Correlations

Before delving into regression methodologies, it is imperative to elucidate the concept of correlation, a foundational principle within statistical analysis. Correlation quantifies the extent of a linear relationship between two variables. One of the primary graphical techniques for visualizing this association is the scatterplot. This graph depicts the values of the two variables as points within a coordinate system, facilitating the visual identification of both the direction (either positive or negative) and the strength (ranging from weak to robust) of the relationship between the scrutinized variables. The Pearson correlation coefficient (PCC), often denoted by r, provides a metric for this linear relationship. The general equation is:

$$r = \frac{1}{n} \sum_{i=1}^{n} \frac{x_i - \bar{x}}{S_x} \times \frac{y_i - \bar{y}}{S_y} \tag{3.6}$$

where n is the sample size (paired data), x_i and y_i are individual observations, while $\bar{x}$ and $\bar{y}$ represent the mean values of x and y, respectively. The value of r spans between -1 and 1:

- Values approaching 1 denote a robust positive correlation: as one variable escalates, the other also exhibits an inclination to rise.
- Values nearing -1 signify a robust negative correlation: an augmentation in one variable typically results in a decrement in the other.
- Values proximate to 0 suggest a weak or non-existent linear correlation.

However, it is quintessential to underscore that a high magnitude of correlation between two variables does not insinuate a causal relationship between them. For instance, a pronounced correlation between shoe size and a reading test score does not necessarily posit that shoe size influences reading proficiency. In certain scenarios, the Spearman correlation coefficient might be more apposite, especially when the relationship between the variables is non-linear or pertains to ordinal variables. In summation, correlation proffers invaluable insights regarding the relationship

between two variables, and a thorough grasp of this notion is paramount before advancing to more intricate analyses such as regression.

3.5.2 Regressions

In RSM, regression models serve as fundamental tools for analyzing the relationship between a dependent variable (response) and independent variables (factors). These tools complement the ANOVA, which identifies active factors and seeks a systematic trend in the response through a mathematical function. These mathematical models try approximate the unknown functional relationship between the variables. Especially when the specific form of this relationship is not pre-established, one frequently encounters scenarios in the scientific realm where experimental data are employed to elucidate physical phenomena. However, given the rarity of physical phenomena exhibiting very high polynomial orders, prudence in selecting these orders is advocated, as highlighted by Occam's Razor principle in section 3.1.2. While these techniques are powerful, it is always better to approach these problems with criticism: media stat virtus. For this reason, a simple regression technique will be illustrated, aiming to equip readers with the necessary knowledge and tools to fully comprehend the results presented in this work. It should be noted that to fit polynomials of order higher than the first, excluding the interaction, 3^k factorial designs or multi-level designs can be used.

In general, the operations that need to be executed sequentially are the graphical representation of the experimental data, enabling an informed and justified choice of the model one wishes to adopt to explain the data.

"The first thing you should do is plot the data!" D. C. Montgomery

Subsequently, one of the available techniques calculates the parameters of the model. Finally, the adequacy of the model is assessed by analyzing one or more parameters. The initial phase is crucial and often hinges on the data analyst's expertise, and this step significantly aids the subsequent phase. For the second phase, a simple example is introduced, which aptly encapsulates the mathematical method and fits well in many practical scenarios.

Regressions can take various forms, such as quadratic, logarithmic, exponential; however, these are not referred to as nonlinear regression [81]. Given k factors,

denoted as $(x_1, x_2, \cdots, x_k)$, and after conducting n laboratory tests, the objective is to ascertain a linear relationship with the response y and the following equations are obtained:

$$\begin{aligned} y_1 &= \beta_0 + \beta_1 x_{11} + \beta_2 x_{12} + \cdots + \beta_k x_{1k} + \varepsilon_1 \\ y_2 &= \beta_0 + \beta_1 x_{21} + \beta_2 x_{22} + \cdots + \beta_k x_{2k} + \varepsilon_2 \\ &\vdots \\ y_n &= \beta_0 + \beta_1 x_{n1} + \beta_2 x_{n2} + \cdots + \beta_k x_{nk} + \varepsilon_n \end{aligned} \tag{3.7}$$

that it is most practical to write the equations 3.7 in form of matrix and vectors:

$$\mathbf{y} = \begin{pmatrix} y_1 & y_2 & \cdots & y_n \end{pmatrix}^T \tag{3.8}$$

$$\mathbf{X} = \begin{pmatrix} 1 & x_{11} & \cdots & x_{1k} \\ \vdots & \vdots & \ddots & \vdots \\ 1 & x_{n1} & \cdots & x_{nk} \end{pmatrix} \tag{3.9}$$

$$\beta = \begin{pmatrix} \beta_0 & \beta_1 & \cdots & \beta_k \end{pmatrix}^T \tag{3.10}$$

$$\varepsilon = \begin{pmatrix} \varepsilon_1 & \varepsilon_2 & \cdots & \varepsilon_n \end{pmatrix}^T \tag{3.11}$$

where Eq. 3.8 is the responses vector, Eq. 3.9 is an $(n \times k+1)$ matrix of the factor levels and Eq. 3.11 is the error vector. The vector in Eq. 3.10, consisting of the regression coefficients, is unknown in this system. Consequently, the relationship can be compactly expressed as:

$$\mathbf{y} = \mathbf{X}\beta + \varepsilon \tag{3.12}$$

The least squares method (LQM) generally fits regression models to sample data because the problem is stochastic and not deterministic. The latter aims to minimize the sum of squares of the errors between the observed data and the fitted model. Without going into too much detail, as a result, this procedure provides the regression model:

$$\hat{\mathbf{y}} = \mathbf{X}\hat{\beta} \tag{3.13}$$

where $\hat{y}$ and $\hat{\beta}$ are the response and regression coefficients, respectively. The difference between the measured responses and the model responses produces the residual:

$$\varepsilon = \mathbf{y} - \hat{\mathbf{y}} \tag{3.14}$$

At this point, the SS of the residual is calculated:

$$\mathrm{SS}_{\mathrm{Residuals}} = \sum_{i=1}^{n} (y_i - \hat{y}_i)^2 \tag{3.15}$$

Finally, the variance of the model is determined by its degrees of freedom $(n-k)$. The final step involves analyzing and evaluating the derived model through residual analysis. It is standard practice to plot the residuals on a normal probability graph. It is a good model quality indicator if the residuals are approximately normally distributed and do not show systematic factors. Residuals typically should be distributed randomly, given that the data originate from stochastic processes. If the residuals display issues, several strategies can be adopted. A straightforward approach is to increase the polynomial degree in the regression model. However, this method must be used judiciously, as emphasized repeatedly, because regression analysis aims to differentiate the systematic part from the random one. Therefore, one should consider the physical phenomenon, ensuring that the degree of the polynomial remains as low as feasible to achieve residuals devoid of systematic irregularities and patterns. Further, various issues inherent to experimental procedures, such as outliers, can arise through residual analysis.

3.5.3 Lack of fit test

In advanced statistical methodologies, the SS of residuals is partitioned into two primary components during an ANOVA, the lack-of-fit (LOF) and the pure-error (PE). The former is integral to the F-test, assessing the fit of a proposed model against the null hypothesis. Mathematically represented as:

$$\mathrm{SS}_{\mathrm{Error}} = \mathrm{SS}_{\mathrm{PE}} + \mathrm{SS}_{\mathrm{LOF}} \tag{3.16}$$

The text$\mathrm{SS}_{\mathrm{PE}}$ is derived by assessing the variability inherent in repeated observations across each independent variable level. Conversely, text$\mathrm{SS}_{\mathrm{LOF}}$ quantifies the divergence between observed values and those predicted by the model. Notable

magnitudes of this divergence may intimate potential non-linearity in the model. The adequacy of linearity of the model is assessed via the statistic F, a ratio of the mean square for lack of fit (textMS$_{\mathrm{LOF}}$) to the mean square for pure error (textSS$_{\mathrm{PE}}$). Adherence to linearity is indicated should F conform to a specified F-distribution [82].

In summary, this test serves as an instrumental tool in the rigorous evaluation of model adequacy, guiding the potential exploration of alternative, more fitting models.

3.5.4 The 3^k Factorial Designs: Implementation in the current study

The 3^k factorial design was specifically harnessed for the optimization of a process parameter in this research, a topic that will be meticulously dissected and elaborated upon in Chapter 5. The 3^k factorial design delineates experimental frameworks comprising k factors at low, intermediate, and high levels. There are salient reasons to adopt the 3^k design. While it may appear as an intuitive choice for encapsulating quadratic relationships between variables, it is essential to acknowledge that its efficiency can be contingent on specific scenarios. From a mathematical perspective, this design allows for the construction of a regression model, which can be illustrated as:

$$y_1 = \beta_0 + \beta_1 x_1 + \beta_2 x_2 + \beta_{12} x_1 x_2 + \beta_{11} x_1^2 + \beta_{22} x_2^2 + \varepsilon \tag{3.17}$$

Compared to the 2^2 design, the quadratic terms x_1^2 and x_2^2 are included with their respective regression coefficients. Alternate methodologies offer superior efficacy in specific applications. However, a 2^k design supplemented with center points could provide a more streamlined approach [71].

3.5.5 Stepwise regression method

Following an in-depth, comprehensive discourse on regressors, it becomes imperative to address the intricacies of the stepwise regression method. Among all the potential parameters, the stepwise methodology aims to pinpoint a concise subset that elucidates the predominant portion of the observed variance. Such a meticu-

lous selection process is pivotal, as it circumvents complications associated with overdetermination and multicollinearity.

Historically, the hierarchical traditional approach, which sequentially considered lower-order terms before the introduction of higher-order counterparts, has been superseded by a more parsimonious methodology. A standard non-hierarchical stepwise method with an SL of 10 % for the Alpha-to-Enter and Alpha-to-Remove values in this doctoral research has consistently been favored, primarily due to its propensity to yield more streamlined models, following Occam's razor principle. The culmination of this rigorous process is the acquisition of the Reduced Model of the experiment, a representation that, albeit not necessarily optimal, is undeniably coherent and pragmatic.

With advanced computational tools, techniques such as the stepwise and best subset procedures have facilitated multiple regression analysis. In its robustness, the stepwise routine commences by selecting the independent variable that showcases the strongest correlation with the dependent variable. Subsequent steps involve including or excluding variables based on their marginal contribution, consistently reassessing the significance of variables, thereby ensuring refinement of the model. This procedure persists until no additional variables can feasibly be incorporated or excised [69].

In conclusion, while computational aids have greatly enhanced model construction, pivotal decisions inherently rely on both technical and statistical criteria. Such judgments must be partially relegated to automated procedures, underscoring the need for an astute analytical approach.

Chapter 4

Powder stream characterization

4.1 System description

The interdepartmental Integrated Additive Manufacturing center at the Politecnico di Torino (IAM@PoliTo) is a prominent reference in advanced research about additive manufacturing. Steadfast in its commitment to forging a multidisciplinary platform for additive manufacturing, this center addresses the extant challenges associated with machinery, materials, and pioneering applications. Central to its ethos is the ambition to seamlessly incorporate additive manufacturing within the industry 4.0 paradigm, leveraging the rich reservoir of expertise amassed over the years.

Within the ambit of this distinguished institution, the system and materials elucidated in the present research have been directly sourced from IAM@PoliTo. This exposition constitutes a modest yet salient segment of the extensive gamut of investigations and endeavors underway at the center, underscoring the significance and preeminence of IAM@PoliTo in the global AM landscape. In reference to the classification, the system under examination falls within the DED category, wherein a laser is employed to melt metallic powder onto a substrate. Consequently, following the ISO guidelines, this system is designated as DED-LB/Powder/SS-316L.

4.1.1 Machine specification

The study emphasizes the powder feeding system, specifically the CS 150 by Optomec (Albuquerque, NM, USA), depicted in Fig. 4.1.

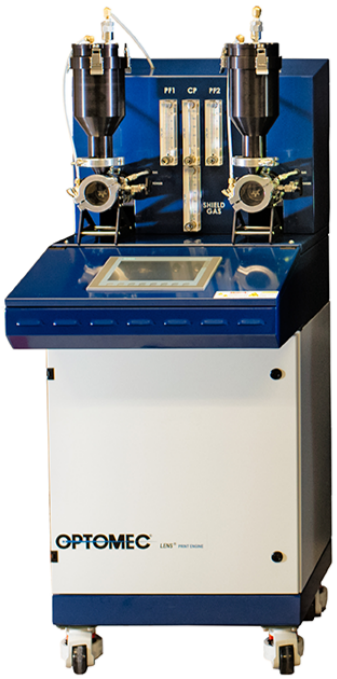

Fig. 4.1 Optomec CS 150 powder feeder system

By blending innovation with functionality, the system seamlessly integrates the principles of a rotating disk and a pressurized gas-enhanced gravity hopper. Within this system, two crucial operational variables stand out. The first is the carrier gas flow rate, V_{cg}, measured in L·min^{-1}, and the second, the disk rotation speed, ω, is gauged in rotations per minute (rpm). It should be noted that according to the International System of Units (SI) and ISO 80000-3 [83, 84], ω should ideally be expressed in s^{-1} or equivalently in Hz. However, this would introduce complications in intuitively understanding the rotation values. The relationship between Hz and rpm is given by:

$$\text{Hz} = \frac{\text{rpm}}{60} = 0.01\bar{6}\,\text{rpm} \tag{4.1}$$

Given these considerations, this work opts to use rpm as the unit of measurement for ω to maintain clarity and ease of interpretation. Argon was the preferred carrier gas for this research, leading to its notation as V_{Ar}.

Through exploration of the inner workings of the powder feeder, it operates on a fundamental, yet ingenious mechanism. The feeder employs a rotating disk punctuated with evenly spaced holes, which moves against a stationary disk with a single hole aligned with the gas inlet. Adjacently, there is a conduit tailored for

powder transport. As the disk rotates, the holes align at intervals with the stationary disk hole and the powder outlet, capitalized on the Venturi effect to streamline the powder through the outlet. The powder stored in the hopper descends due to gravity into this metering system, with a stepper motor governing the rotation of the disk. The interaction between the size and number of holes, combined with the ω and the V_{cg}, turns in the mass flow rate of the powder, Q_p. The efficient operation of the powder feeder system is based on a consistent supply of carrier gas, stored in a cylinder system, and supplied at a pressure of (5.0 ± 0.6) bar. A lamination valve ensures V_{cg}, with its rate precisely controlled using a manual Sho-Rate flow meter from Brooks (Hatfield, PA, USA). The latter is a Glass Tube Variable Area Flow Meter that offers an accuracy of 5 % and a repeatability of 0.25 %.

Continuing with the research equipment, the AM system is the Laserdyne 430 (Fig. 4.2, supplied by Prima Additive (Torino, ITA).

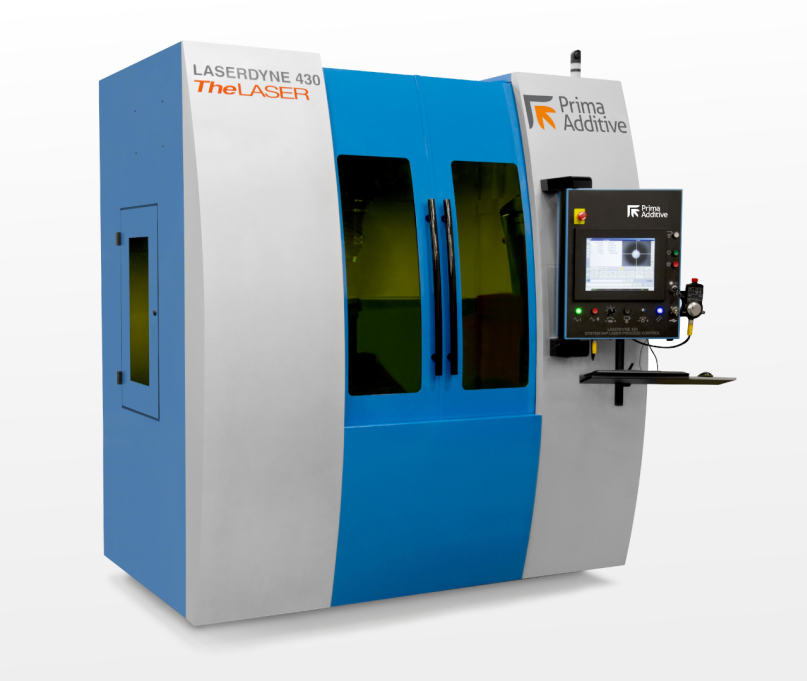

Fig. 4.2 Prima Additive Laserdyne 430 DED-LB system

This DED-LB system, fully integrated into a CNC framework, boasts a roto-tilting table that increases its five-axis deposition capability. The deposition head, constructed through a blend of additive manufacturing techniques and meticulous grinding, houses four distinct nozzles suited for powder flow, each presenting a

nominal radius, r_{nozzle}, of (0.50 ± 0.01) mm. Moreover, the system is equipped with the CF 1000 fiber laser by Convergent Photonics (Turin, ITA), it features a fiber laser delivering a robust maximum power of 1 kW, with a D of (2.00 ± 0.01) mm and a wavelength range of (1075 ± 3) nm. Furthermore, all experiments conducted in this study followed the guidelines set by Prima Additive, which recommends depositing at a standoff distance of 8 mm from the substrate. All the specifics of the system used in this study are presented in Table 4.1.

Table 4.1 Laserdyne 430 datasheet

Parameter	Value
Building volume	$(585 \times 400 \times 500)$ mm^3
Laser type	Yb fibre laser
Wavelength	$(585 \times 400 \times 500)$ mm^3
Max. Power	1 kW
Max. travel speed	250 mm·s^{-1}
Beam diameter	(2.00 ± 0.01) mm
Nozzles configuration	discrete
Number of nozzles	4
Radius of the nozzle	(0.50 ± 0.01) mm

Within the Laserdyne 430 system, it is critical to highlight the restricted mobility of the deposition head, which operates exclusively along the Z-axis of the system. This design decision carries paramount significance. Analyses have shown that alterations in the configuration of the head within the system do not influence the Q_p. Such flow consistency might be at risk if the deposition head had rotational capabilities, which could lead to changes in the powder feeding tube configuration. Introducing rotation can manifest in bends, elbows, and other structural shifts, represented by increased pressure loss coefficients in the governing flow equation for pipes, namely the Darcy-Weisbach equation [85].

4.1.2 Feedstock material

The feedstock material used in this research is a commercially sourced gas-atomized pre-alloyed MetcoAdd 316L-D austenitic stainless steel powder supplied by Oerlikon (Freienbach, SWI). This powder possesses a nominal particle size distribution of D_{10} = 49.2 µm, D_{50} = 60.9 µm, and D_{90} = 74.6 µm. This distribution was rigorously

assessed using a Mastersizer 3000 laser diffraction particle size analyzer by Malvern Panalytical (Malvern, UK) and is shown in Fig. 4.3.

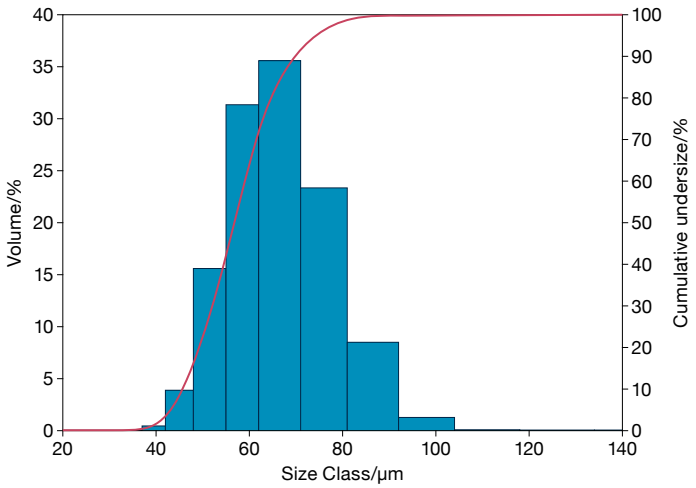

Fig. 4.3 Particle size distribution

The corresponding micrograph of the powder, evident in Fig. 4.4a, showcases predominantly spherical particles, albeit with some observed defects such as satellites, agglomerates, and elongated forms.

Table 4.2 KERN ANJ-NM/ABS-N Characteristics [1]

Max. Capacity	Readability	Repeatability	Linearity
320 g	0.1 mg	0.2 mg	0.3 mg

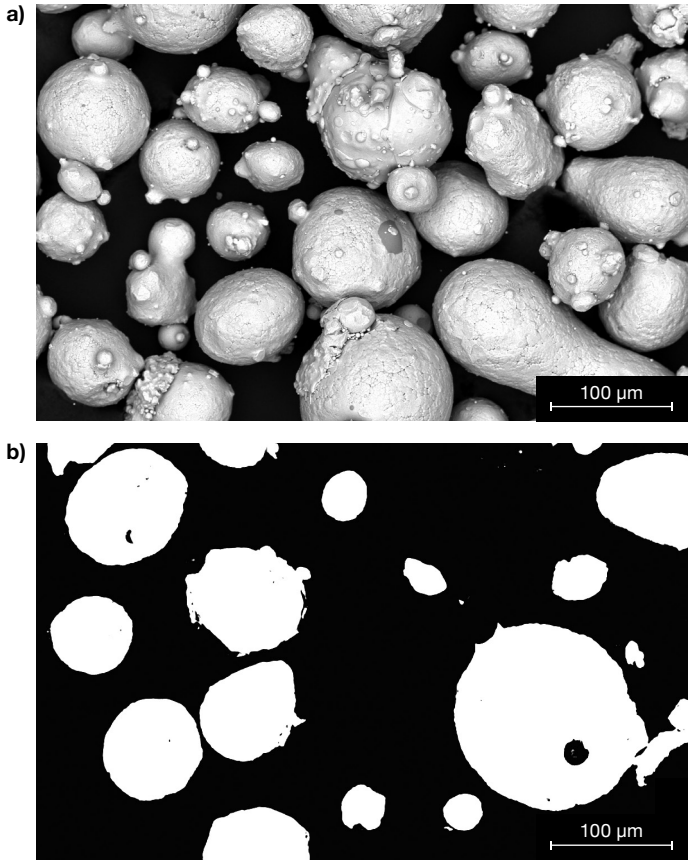

Fig. 4.4 (a) SEM micrograph of 316L powder. (b) Optical micrograph of cross-section of 316L powder

Moreover, a detailed and precise two-step method was employed to determine the average density of the powder. Initially, the mass of the powder sample was precisely gauged using the ANJ-NM/ABS-N balance by KERN (Gottlieb, GER), with characteristics listed in Table 4.2.

This step was followed by assessing the sample volume with the Ultrapyc 5000 pycnometer by Anton Paar (Graz, AUT), detailed in Table 4.3. This instrument employs an iterative technique until a minimal variance of 0.01 % is achieved, and helium (He) is employed as a medium. Consequently, these combined measurements

Table 4.3 Anton Paar Ultrapyc 5000 Characteristics for 10 cm^3 Cell Size [2]

Readability	Accuracy	Repeatability
0.1 mm^3	0.03 %	0.015 %

furnished an average density of $(7.896 \pm 0.005)\,g{\cdot}cm^{-3}$ at $(20.000 \pm 0.001)\,°C$. For a comprehensive description of the methodologies and processes employed to calculate the associated uncertainties, refer to Appendix B. Further insights into the powder were procured by examining its cross-section with the DMI 5000 M optical microscope by Leica Microsystems (Wetzlar, GER), revealing the existence of pores as illustrated in Fig. 4.4b. The bulk properties of the powder adhered to the stipulations of ISO 4490 for flowability and ISO 3953 for tap density [86, 87]. In practical tests, a 50 g sample of the powder transitioned through a Hall funnel within (13.26 ± 0.08) s. Moreover, Carr's compressibility index was registered at 8.3 %, signifying exceptional flowability.

4.2 Experimental plan

4.2.1 Recognition and statement of the problem

The motivation for this analysis emanates from a previous experiment that employed a factorial design of the 3^k type. In that experiment, a counterintuitive response surface was found. As the V_{cg} increased, there was an unexpected decrease in the Q_p. Given the restrictive nature of the ranges in the preceding experiment and the understanding that the subsequent exploration would primarily demand time and gas without incurring hefty costs, it became evident that a more comprehensive investigation into this phenomenon was warranted.

This study seeks to delineate the Q_p transport phenomenon that leads to reducing the Q_p as the V_{Ar} rise, and subsequently the response surface, within the DED-LB system configuration by scrutinizing the input parameters of the powder feeder system and also monitoring and analyzing the boundary conditions, BCs, that, though uncontrollable, are observable and serve as covariates. Parameters that evade direct manipulation encompass attributes like powder morphology, type of material, and some system configurations. BCs remain monitorable, thus allowing their influence

on Q_p to be gauged. Prominent BCs potentially affecting Q_p include attributes of the chamber such as temperature, pressure, and relative humidity. The interplay of these factors is visually represented in the cause-effect diagram, showcased in Fig. 4.5.

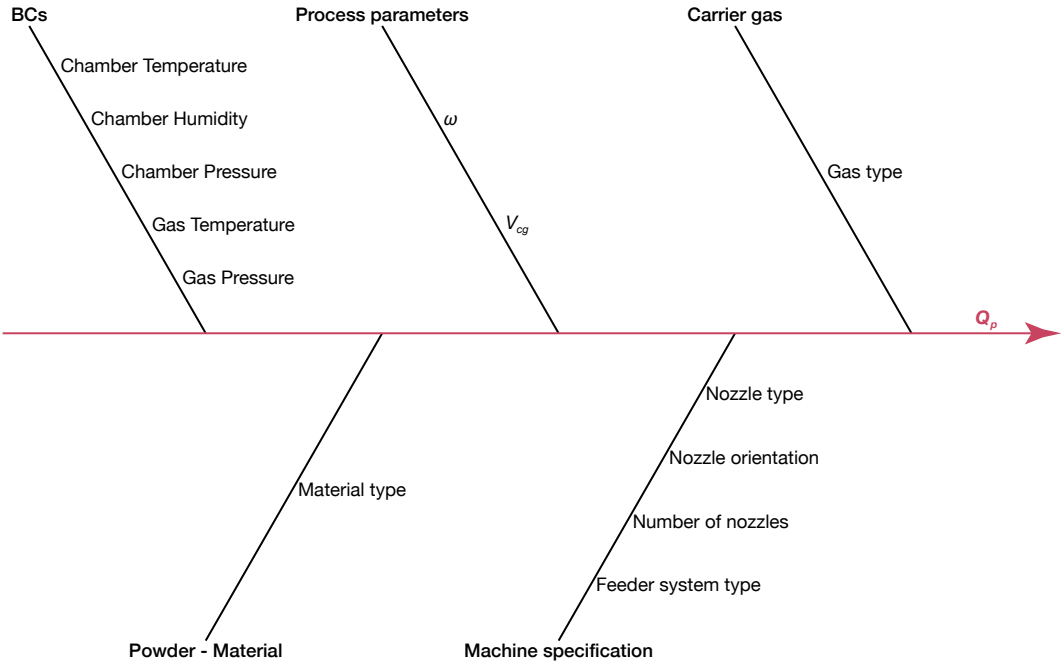

Fig. 4.5 Q_p cause-effect diagram

It should be emphasized that, given that a prior study has been conducted on this system using the same powder but with a more limited design, this investigation positions itself between a confirmation and discovery experiment. On the one hand, it aims to validate findings consistent with previous observations or theories, ensuring that system behavior aligns with established expectations. On the other hand, it delves into exploring potentially new phenomena and factor ranges, venturing into the realm of discovery.

Boundary conditions monitoring system

A tailored monitoring system was designed and assembled to accurately observe BCs. This system incorporates two ESP32 microcontrollers; the first is the Sender, dedicated to data acquisition and elaboration, and the second is the Receiver, to acquire the data from the Sender via a web server. The Bosh BME280 sensor is integrated into this setup. The sensor (BME280) gauges air temperature (T_{Air}),

pressure (p), and air relative humidity (H_R). The operational range, resolution, and accuracy of the BME280 are ideal for measuring boundary conditions within the construction chamber, as delineated in Table 5.

Table 4.4 Bosh BME280 Characteristics

Parameter	Range	Unit	Accuracy
T_A	-40 to 85	°C	± 1.0
P	30 to 110	kPa	± 1.0
H_R	0 to 100	%	± 0.12

To ensure the stability and protection of the monitoring system, it resides in an IP55 box within the construction chamber. Only the Bosh BME280 sensor remains exposed, with a custom made perforated nylon (PA12) component fabricated by selective laser sintering (SLS), providing a shield against powder dispersal. The H_R is one of the monitored parameters due to its dependence on atmospheric pressure and temperature. From an experiential perspective, determining absolute humidity offers greater practical relevance. Absolute humidity (H_A) can be derived from the volume of steam present in a unit mass of dry air, as delineated by Cengel and Ghajar [88]:

$$H_A = \frac{0.622 \cdot H_R \cdot p_v}{p - H_R \cdot p_v} \tag{4.2}$$

Here, H_A signifies absolute humidity in g·m^{-3}, H_R is in %, p_v represents the saturation vapour pressure contingent on temperature, and p indicates pressure. It is paramount to note that the units selected for the components of the equation must be consistent to achieve the desired result. The only variable left undefined is the saturated vapour pressure. Although the Clapeyron equation provides a pathway for determining this parameter, the semi-empirical Antoine equation, derived from experimental data and Clapeyron's formula [89], offers a more straightforward approach. Within the scope of this research, the three-parameter Antoine equation, pertinent between 0 and 100 °C, was employed:

$$\log_{10}(P) = A - \frac{B}{C + T} \tag{4.3}$$

where P represents the vapour pressure in mmHg, T is the temperature measured in °C, and A = 7.96681, B = 1668.21, and C = 228 are recognized as Antoine constants for water [90]. The data acquisition process was carried out at a sampling rate of

1 Hz, according to the sensor data refresh rate. The information was subsequently processed employing the simple moving average methodology, which stands as a fundamental Moving Mean technique [91, 92]. This procedure facilitates the attainment of the average BCs over the experimental duration, eliminating the need for extensive data storage and offering an efficient data analysis avenue.

The code implemented in the Arduino IDE in detail is shown in Appendix C; in particular, the first part is the Sender, and the second is the Receiver code. In particular, the results of the model were rounded off, reflecting the resolution of the sensor and the standard deviation inherent to the regression.

4.2.2 Response variable evaluation

The objective of this research is to measure the unknown response variable, specifically Q_p, within the given system, which is affected by two primary quantitative factors and possibly by BCs. Quantifying Q_p presents challenges due to the dispersion tendency of the powder, influenced by the velocity of the carrier gas and its very small particle size. Additionally, achieving a steady state for the system requires attention. A customized experimental setup was devised to address these complexities, ensuring that the powder was collected during steady-state and within a specific timeframe.

The powder mass was measured using the KERN ANJ-NM/ABS-N balance, which possesses a 320 g maximum load capacity. On the basis of prior familiarity with the system and the capacity of the balance, we allotted a preparatory duration of one minute to pass from a transient state to a complete steady-state powder flow. Following this, two minutes were designated for steady-state powder collection. The acquired weight was divided post-experiment by the test duration to determine Q_p.

The procedure to measure Q_p incorporated the following steps:

1. Two separate beakers were arranged adjacently on the table (refer to Fig. 4.6). The first beaker was designated to collect the powder dispersed during the transient phases, which was used to initiate and stop the powder stream. Meanwhile, the subsequent beaker was set to collect powder during the steady-state phase;

2. The powder amassed in the latter beaker was quantified using the precision balance, and the result was computed as the proportion of weight to time.

After the measurements, the powder from both beakers was collected and prepared for potential future reuse, although it was not utilized within this experiment.

Fig. 4.6 Experimental setup

For this investigation, the hoppers were consistently replenished with virgin powder to prevent any bias in the experimentation. Additionally, the powder level in the hoppers was meticulously maintained above 70 % of their maximum capacity. This precaution was adopted to mitigate potential errors from the weight force that the powder exerts on the conduit that channels the powder into the measuring chamber. Although this phenomenon was constrained within certain limits, its elimination remained elusive. However, through complete randomization of the experimental procedures, any effects of this phenomenon were diffused throughout the tests. The emptied beakers were then repositioned on the table, ready for the subsequent measurement cycle.

Particular emphasis was placed on the design of the beaker collection system. Constructed using ABS through the FFF technique, this system was specifically tailored to serve the needs of this experiment. Two coloration was utilized for the beakers to ensure effortless differentiation between the steady-state and transient phases, thereby minimizing the potential for operational errors during the experiment.

4.3 Choice of experimental design

In the present study, technical constraints have been established for the powder feeder system. Specifically, the upper limits are 24 rpm for ω and 10 $\mathrm{L{\cdot}min^{-1}}$ for V_{cg}. Although the theoretical lower limits for both factors are 0, such values would result in no powder flow, making them practically infeasible. The exploration ranges for these variables were determined based on insights gained from previous experiments. For ω, a range of (2 to 22) rpm was selected, intentionally steering clear of the peak limit of 24 rpm due to complications associated with powder spattering within the metering chamber. Meanwhile, for V_{cg}, a range of (2 to 8) $\mathrm{L{\cdot}min^{-1}}$ was chosen, an extension of the ranges explored in earlier studies.

Evaluations of Q_p resulted in minimal material consumption, argon gas being the exception; the powder was systematically collected, sieved, and reintegrated. For a comprehensive analysis of how ω and V_{Ar} affect Q_p at the nozzles, a methodological design was adopted that incorporates four levels for V_{Ar} and six for ω, arranged uniformly, as presented in Fig. 4.7 and summarized in Table 4.5.

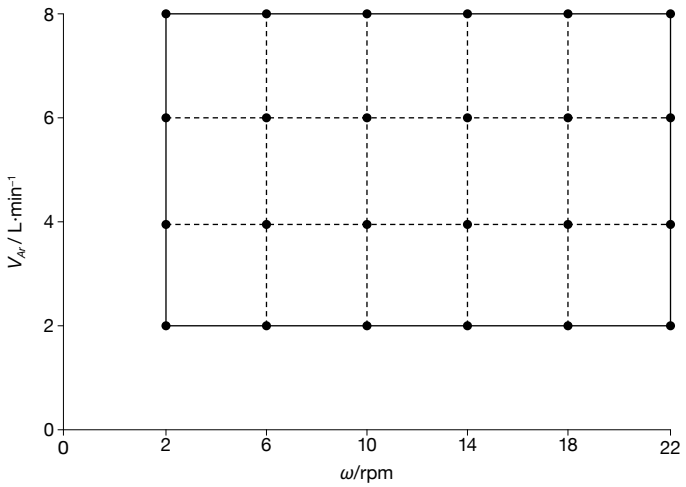

Fig. 4.7 Factorial design with levels and values

Table 4.5 Process variables values used in the planned experimentation

Factor	Values
ω/rpm	2 – 6 – 10 – 14 – 18 – 22
V_{Ar}/L·min^{-1}	2 – 4 – 6 – 8

In a balanced fixed multilevel full factorial design, the capacity to discern a distinction between treatments is contingent upon the levels of each factor. Notably, given that ω possesses more levels, the power of the experiment plan is predominantly contingent on this factor [78, 93]. For the calculation of the sample size, a two-step approach was employed. In the initial step, the necessary sample size was calculated a priori to detect the chosen ES with a specified power and SL. Notably, it was presumed that the main effects and interactions were equally important. Table 4.6 summarizes the results obtained for a *Very Large* ES, a 5 %, minimum power of 80 %, and inclusive of the two covariates. The chosen software was G*Power 3.1.9.4, a free tool developed by Heinrich-Heine-Universität Düsseldorf [94].

At this point, the calculated minimum sample size was divided based on the selected factorial design. Considering the importance of the interaction between the two main effects alongside the main effects themselves, a sample size greater than 69 was chosen. For ease of allocation in the design replications, a sample size of 72 was ultimately selected. This size was based on 24 unique points—derived from 6 levels of the first factor and 4 levels of the second factor—and was allocated to

Table 4.6 *A priori* computed sample size for *Very Large* ES, 5 % SL, and 80 % minimum power

Effects	Groups	df	Sample Size
V_{Ar}	$24+2$	3	41
ω	$24+2$	5	47
$\omega \cdot V_{Ar}$	$24+2$	15	69

Table 4.7 *Post hoc* computed power

Effects	df	Critical F	Power/%
V_{Ar}	3	2.8	99
ω	5	2.4	97
$\omega \cdot V_{Ar}$	15	1.9	83

allow for 3 replications per point, yielding 72 tests. Subsequently, the power of the F test was calculated to identify all factors considered and is presented in Table 4.7. The results obtained for the chosen sample size are satisfactory with respect to the hypotheses formulated.

4.4 Analysis and discussion

The experiment was carried out in a single day. Within this period, covariates were acquired, namely temperature (T_A) and absolute humidity (H_A). A blocking strategy was deemed unnecessary because the experiment was carried out in one day by a single operator and with powder from a single container. It should be highlighted that a software package determined the test sequence pseudo-randomly based on the methodology introduced by von Neumann [95]. To mitigate potential errors related to the gas flow regulation system, in each test V_{Ar} was first maximized. Subsequently, during the transient phase, it was adjusted to the precise rate, following the guidelines provided by Montgomery [71]. In this manner, errors arising from issues such as sensor blockage or residual pressure in the pipelines were avoided. Each test consistently used the same upstream argon pressure for the feeder system.

Table 4.8 ANCOVA for Q_p/(g·min^{-1})

Source	df	Contribution/ %	Adj SS	Adj MS	F	p-value/ %
Model	25	99.37	3153.64	126.145	291.78	<0.1
Covariates	2	5.93	0.76	0.379	0.88	42.3
T_A	1	2.66	0.45	0.455	1.05	31.0
H_A	1	4.54	0.53	0.532	1.23	27.3
Linear	8	79.97	2504.51	313.063	724.13	<0.1
ω	5	47.45	981.03	196.205	453.83	<0.1
V_{Ar}	3	32.52	865.53	288.508	667.34	<0.1
2-Way Inter.						
$\omega \cdot V_{Ar}$	15	13.47	427.41	28.494	65.91	<0.1
Error	46	0.63	19.89	0.432		
Total	71	100				

4.4.1 ANCOVA analysis

The data (see Appendix D) were assessed using ANCOVA, and within the experimental ranges observed, neither temperature nor absolute humidity seems to influence Q_p as depicted in Table 4.8. Therefore, these covariates will not be incorporated into subsequent phases of this study, and all results presented will be in the context of a temperature of $(27.4 \pm 2.1)\,^{\circ}$C and an absolute humidity of $(11.4 \pm 0.1)\,$g·m^{-3}. However, tracking these BCs may prove beneficial in the long term, and these data will be retained for potential research. The model yielded a standard deviation, S, of 0.6, an $R^2(adj)$ of 99.4 %, which means that the model explains almost 99 per cent of the variability of the data and an $R^2(pred)$ of 98.5 %, which is an indicator of how well the model could predict new observations. The distribution of the residual plots is almost normal, which suggests that terms of an order higher than the first may need to be included in the model to explain the data adequately. Four notable outliers are observed in tests (Standard Order) 13, 37, 38, and 52; these are presented in Table D.1 in Appendix D. These last are evident at 14 rpm in combination with lower V_{Ar} rates (2 L·min^{-1} and 4 L·min^{-1}). Randomization of the experiment ensures that there are no discernible patterns or variations in the residuals. Analysis indicates that linear terms predominantly influence the total Adjusted SS, with the ω factor having the most substantial impact. The primary effects and their interactions are statistically significant for the selected SL, as validated by their p-values.

In Fig. 4.8, factorial plots of the main effects are presented. A clear trend is observable, whereby an increase in ω corresponds to an almost linear enhancement in the response. In particular, between (18–22) rpm, the response shows a reduction, diverging from the trend. Furthermore, with respect to the increase in V_{Ar}, the findings corroborate those from previous experimentation, demonstrating an inverse relationship with Q_p. As V_{Ar} increases, a decrease in response is evident. Regarding the interaction, as illustrated in Fig. 4.9, it is more pronounced at lower V_{Ar} levels, whereas it becomes almost negligible at $8\,\mathrm{L{\cdot}min^{-1}}$.

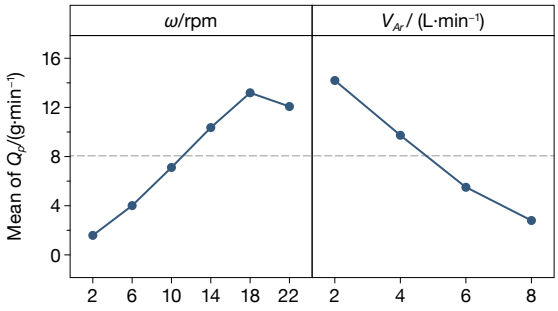

Fig. 4.8 Main effects factorial plots for Q_p

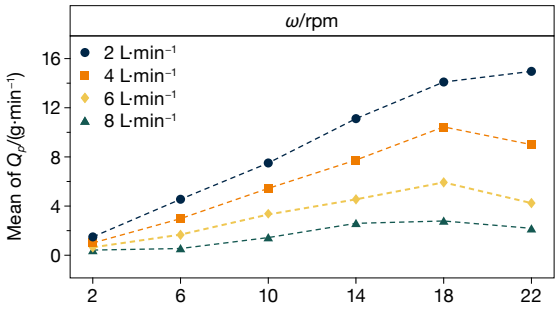

Fig. 4.9 Interaction plot for Q_p

For a more comprehensive understanding of the effects, visualization via a normal probability plot (NPP) using the Johnson's method is presented in Fig. 4.10. This plot elucidates the distinctions among the means of the effects at different factor levels. A distinct variability in the data is observed as the factor levels alter, particularly noticeable between the levels (2–10) rpm (see Fig. 4.10, a). In contrast, the range between (14–22) rpm levels displays consistent means and variances, a fact previously underscored in the factorial plot of the main effect (Fig. 4.8).

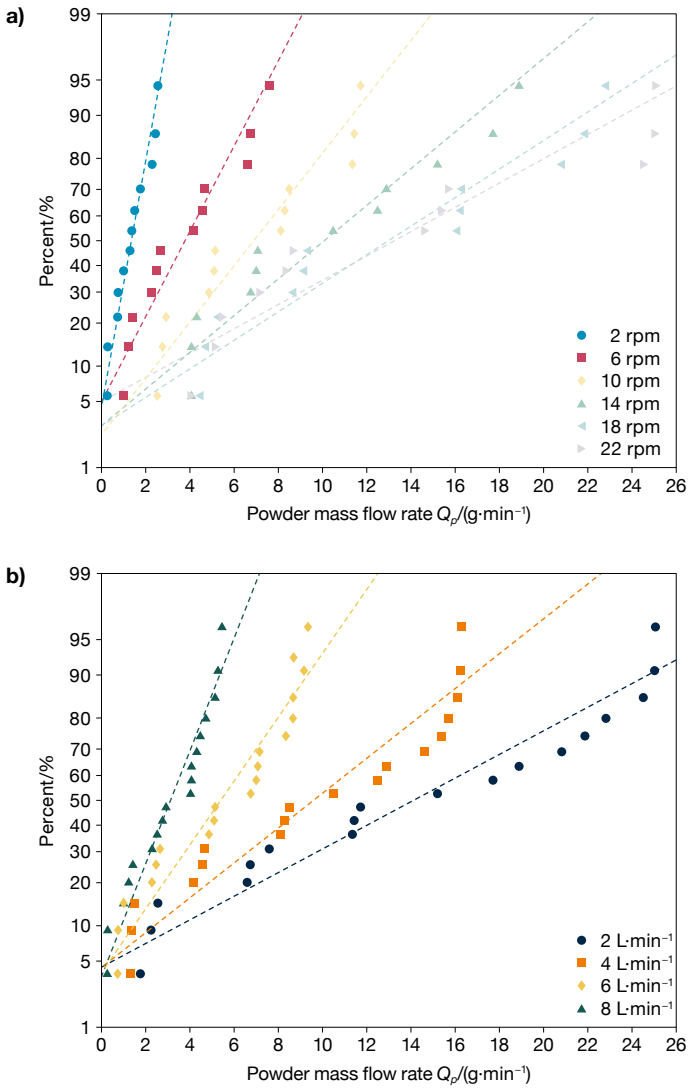

Fig. 4.10 Factorial main effect probability plot (Johnson's method) vs. ω (a), and versus V_{Ar} (b)

Such observations imply the non-adherence to the assumption of homoscedasticity. The physical phenomena at play are not consistent across all evaluated factor levels. This variability suggests that, at high ω levels, there may not be a consistent behavior that governs the volume of powder that passes through the metering system.

A physical threshold might exist for the scrutinized powder to pass through the disk holes at such velocities. Regarding the V_{Ar} factor, the onset of high turbulence in the pipes and then in the measuring chamber, at higher levels (spanning 6 to 8) has been substantiated, as evidenced by significant flow meter oscillations observed

during the experiment, which complicate the transportation of the powder. It is worth noting that while the standard deviation displays variations between the levels of ω and V_{Ar} the CV, as detailed in Table 4.9 and Table 4.10, exhibits minimal fluctuation. This trend signifies that data dispersion increases with increasing mean responses, implying that the relative variability of data remains almost constant at all levels. This observation may indicate that the variation in machine behavior is primarily driven by changes in levels rather than the variability of internal data that affects the different behaviors [96].

Table 4.9 Descriptive statistics of Q_p/(g·min^{-1}) for ω levels

ω/rpm	N	Mean	SE Mean	St. Dev	CV/%
2	12	1.35	0.23	0.79	58.62
6	12	3.78	0.66	2.29	60.62
10	12	6.89	1.00	3.47	50.31
14	12	10.08	1.54	5.32	52.77
18	12	12.98	1.98	6.84	52.72
22	12	13.25	2.32	8.04	60.67

Table 4.10 Descriptive statistics of Q_p/(g·min^{-1}) for V_{Ar} levels

V_{Ar}/L·min^{-1}	N	Mean	SE Mean	St. Dev	CV/%
2	18	14.11	1.95	8.27	58.56
4	18	9.59	1.32	5.60	58.43
6	18	5.39	0.72	3.06	56.68
8	18	3.12	0.41	1.73	55.46

4.4.2 RSM analysis

In this section, the primary objective is to derive a response surface that is both simplistic and sufficiently explanatory of the data. The 22 rpm level for ω has been omitted from this analysis based on prior discussions. The response was analyzed using the standard stepwise methodology for linear, quadratic and interaction terms, allowing for removing less effective terms to simplify the model without losing information. A non-hierarchical approach was employed to maintain a more conservative model, with a 10 % SL as the Alpha-to-Enter and to Remove. This way,

less effective terms can be removed from the model, making it more straightforward without losing information. The regression model emerged after four iterations after concluding the regression optimization process. It results in an S of 0.7, an $R^2(adj)$ value of 98.7 %, and a predicted $R^2(pred)$ value of 98.5 %.

The ANOVA of the regression modelis reported in Table 4.11 shows that the model fits the data well, as the LOF test yields a p-value greater than the SL chosen, then is not significant. Moreover, a close examination of residuals, representing the disparities between observed values and their corresponding model predictions, affirms the robustness of the model.

Table 4.11 ANOVA for the regression model for $Q_p/(\mathrm{g{\cdot}min^{-1}})$

Source	df	Contribution/ %	Adj SS	Adj MS	F	p-value/ %
Model	4	98.79	2048.25	512.06	1118.11	<0.1
Linear	2	85.71	1777.21	888.60	1940.31	<0.1
ω	1	50.56	1048.37	1048.37	2289.18	<0.1
V_{Ar}	1	35.15	728.83	728.83	1591.44	<0.1
Square						
$V_{Ar} \cdot V_{Ar}$	1	0.36	7.48	7.48	16.33	<0.1
2-Way Inter.						
$\omega \cdot V_{Ar}$	1	12.71	263.57	263.57	575.52	<0.1
Error	46	0.63	19.89	0.432		
LOF	15	0.37	7.73	0.52	1.18	32.5
Pure Error	40	17.46	0.44			
Total	59	100				

The normal distribution of residuals was corroborated through the NPP followed a linear trend. Furthermore, the Anderson-Darling test (ADT), reveals that the null hypothesis, which states that residuals adhere to a normal distribution, cannot be rejected at a 5 %. Further validation is evident in the residual plot against the fitted values. Here, the residuals form a horizontal band close to the zero line, and no evident patterns are discernible. Upon evaluation of these results, the predictive capacity of the model is notably high. The subsequent response surface equation, expressed in coded units, was derived. Henceforth, this equation will be employed to characterize the powder flow within the scope of this investigation.

$$Q_p/(\mathrm{g{\cdot}min^{-1}}) = 6.574 + 5.911 \cdot \omega - 4.676 \cdot V_{Ar} + 0.794 \cdot V_{Ar}^2 - 3.977 \cdot \omega \cdot V_{Ar} \quad (4.4)$$

Accompanying standard errors and detailed results are furnished in Table 4.12. For a comprehensive visual interpretation, the contour plot of the response surface is shown in Fig. 4.11.

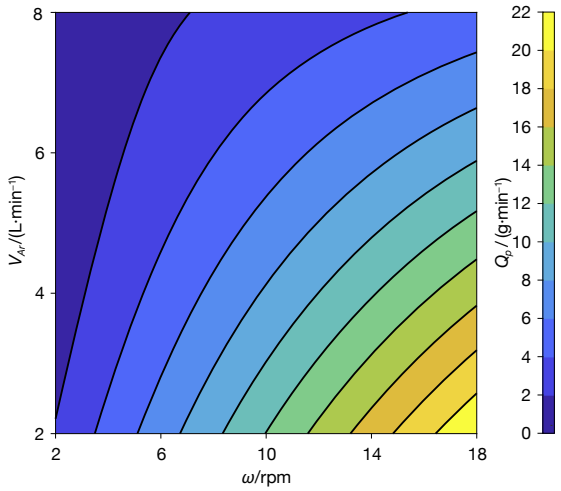

Fig. 4.11 Q_p contour plot of the response surface

Table 4.12 Estimates of parameters of the model in coded units

Variable	Parameter	Coef	SE Coef
Constant	β_0	6.574	0.140
ω	β_1	5.911	0.124
V_{Ar}	β_2	-4.676	0.117
V_{Ar}^2	β_{22}	0.794	0.197
$\omega \cdot V_{Ar}$	β_{12}	-3.977	0.166

4.5 Conclusions

This research thoroughly investigated the behavior of 316L powder Q_p within the CS 150 system coupled with the Laserdyne 430. The study utilized an intricate DoE, accounting for numerous factor levels while meticulously addressing potential noise sources. Through a rigorous application of ANCOVA, three discrete powder transportation mechanisms were identified:

1. Beyond a rotational speed of 18 rpm, the efficiency with which disc rotations transport powder starts to reduce. **This indicates that the mechanical limitations of the system do not necessarily align with its physical constraints**;

2. Upon exceeding a V_{Ar} of $6\,\mathrm{L{\cdot}min^{-1}}$, the system exhibits turbulence which negatively influences the response. **From an economic and environmental sustainability standpoint, it is advisable to operate at lower V_{Ar} levels to achieve the same Q_p rates**;

3. At a V_{Ar} of $2\,\mathrm{L{\cdot}min^{-1}}$, the velocity of the powder stream exiting the deposition head is diminished, resulting in an imprecise formation at the standoff of the deposition head, which in turn means the powder possesses inadequate energy for optimal transportation. **Clearly, the powder lacks the requisite kinetic energy upon exiting the nozzle, leading to poor focalization at the standoff.**

Moreover, the analysis unveiled certain operational ranges, contingent upon specific factor levels, that define the performance boundaries of the examined system. A pivotal finding within these boundaries is the capability of the system to achieve Q_p values ranging from $(0.3$ to $21.9)\,\mathrm{g{\cdot}min^{-1}}$, emphasizing the flexibility and adaptability of the system with the given powder. Results from the study align with previous observations in which, within a vertical powder supply configuration, an increase in the value of ω typically augments the Q_p for specified V_{Ar} levels.

The study further highlighted that with an increase in V_{Ar}, the range of potential Q_p values contracts. From an operational perspective, utilizing excessively high V_{Ar} levels is less than optimal, given the minimal variation in Q_p upon adjusting the ω factor. Distinct Q_p ranges were discerned when alterations in factor levels were synchronized.

This comprehensive analysis accentuates the benefits of a well-constructed DoE and underscores the significance of a holistic approach that considers all variables and noise sources over extended periods. To the best of current understanding, this work is a pioneering effort to explore the diverse phenomena intrinsic to this particular powder feeder system, especially when integrated with a boundary condition monitoring apparatus. Experimental data revealed a spectrum of transport physics phenomena with potential implications on the accuracy and volume of Q_p.

While the foundational assertions in this research are backed by statistical analysis, reservations exist, particularly about the breadth of covariance and the evaluated

effect size. Future efforts are encouraged to focus on more refined V_{Ar} level ranges, incorporate additional replications, and consider alternate DoE methodologies to reduce the standard error inherent in the regression coefficients, enhancing the robustness of the response.

Chapter 5

Melt pool and track formation: modeling and experiments

5.1 Relationship between powder stream and track formation

In the current research, emphasis is placed on a comprehensive understanding of the powder stream, as discussed in the preceding chapter. The objective is to optimize the delivery of powder to the melt pool, ensuring accurate track construction. Without a real-time feedback mechanism to verify the current construction height during the fabrication process, a reliable and robust strategy becomes increasingly vital. Knowledge acquired through such strategies could be advantageously integrated into systems with feedback mechanisms to enhance the overall quality of the deposition. The latter necessitated a departure from traditional methodologies, which rely on single-track analyses to determine the thickness of the layer.

In this research context, the height of prismatic specimens is directly employed to infer the height of the track, facilitating a correlation between the volume of powder dispensed and the geometric parameters of the track. This approach culminated in the introduction of a pivotal dimensionless parameter, R, represents the ratio of the volumetric flow rate of powder dispensed from the deposition head, represented as $V_p = Q_p/\rho_p$, to the expected track to be constructed in a given time frame, symbolized as V_{track}. The track volume per unit of time can be roughly estimated as

the product of track height ΔZ (defined by the Z-increment of the deposition head at each new layer), D, and v. The mathematical representation of this relationship is given by:

$$R = \frac{V_p}{V_{\text{track}}} = \frac{Q_p}{\Delta Z \cdot v \cdot D \cdot \rho_p} \tag{5.1}$$

where ρ_p is the powder density, and assuming that the density of the deposited material is equivalent to the powder density, the expression for R can be simplified as:

$$R = \frac{Q_p}{Q_{track}} \tag{5.2}$$

where Q_{track} is the deposited mass rate of the track. The units of measurement for both terms in R must be consistent to ensure that R remains dimensionless. The ideal scenario would have R equals 1, signifying an optimal powder-to-track ratio without losses. Given the nuances in real-world applications, modifications to the initial equation became essential. Consequently, a multiplicative coefficient κ (greater than or equal to 1) was introduced and multiplied by the factor R to account for powder losses in the process, expressed as a percentage. Henceforth, R will be consistently held at 1 for this work, allowing modifications to be exclusively centered on κ.

In this work, O_e is treated as a qualitative rather than quantitative factor for two pivotal reasons. First, it allows for the simple linkage between the powder mass flow rate and the intended track geometry to be constructed. Second, it correlates the tool path— the deposition head in this context—with the virtual geometry one aims to create, which is prismatically shaped. Given these premises, it becomes intuitive to conceive that a layer can be constructed in multiple passes or sub-layers by overlapping tracks. These tracks must have a height lesser than the layer to meet the geometric constraints. To address this and lend a unique and original approach to the problem, a qualitative scheme was chosen over a quantitative one.

Accordingly, layers can be constructed by overlapping 1, 2, 3, or 4 tracks or without any overlap. Depending on overlap values, such as 75 %, 66.7 %, 33.3 %, or 0 %, the requisite number of tracks needed for a given layer width is multiplied by factors of 4, 3, 2, or 1, respectively. Conclusively, the Q_p relationship is conveyed through the system of equations, including the prediction of Q_p based on the deposition rate,

the Q_p function of $V_A r$ and ω, and the minimum and maximum limit values of Q_p:

$$\begin{cases} Q_p = \kappa[R \cdot \Delta Z \cdot v \cdot D \cdot \rho_p \cdot (1 - O_e)] \\ Q_p = f(Q_{Ar}, \omega) \\ 0.3 \leq Q_p/(\text{g}\cdot\text{min}^{-1}) \leq 21.9 \end{cases} \tag{5.3}$$

where O_e can range from 0.75 to 0. Hypothetically, it could also assume a value of 1; however, this implies that the tracks are entirely overlapping, resulting in the construction of a single wall. Such a scenario is not considered in this study, although the equation system could be adapted for this purpose. Therefore, when employing a value of 0.75 for O_e, it indicates the intention to construct the layer by overlapping the tracks by 75 %, requiring four passes. Subtracting this value from 1 reduces the mass flow rate by 75 %, effectively utilizing only 25 % of the flow rate to construct the layer. In contrast, if a value of 0 is used, meaning that there is no overlap, the entire flow rate necessary to construct the layer would be utilized.

This system of equations 5.3 adeptly provides Q_p as a function of the deposition rate, which is intrinsically tied to the process parameters, especially v. In addition, it includes the characteristics of the fixed system (D), the density of the chosen powder, and the specifics of the powder feeder system, along with its operational constraints. In particular, O_e is treated as a qualitative factor rather than a quantitative numerical value and all the units of the parameters are chosen in such a way as to be consistent and to be oriented to obtain Q_p in the desired units ($\text{g}\cdot\text{min}^{-1}$).

5.1.1 Challenges in the initial experimental design: setting the stage for carrier gas flow optimization

During the experimental phase of a complex factorial design focused on screening mechanical and physical properties (height of the specimens, density, porosity, and hardness), certain problems arose. Several key factors come into play in the DED-LB process, such as laser power, P, travel speed, v, powder mass flow rate, Q_p, carrier gas flow rate, V_{cg}, overlap efficiency, O_e, layer thickness, ΔZ, and scanning strategy. Among these, Q_p, P, and v are closely related. For example, increasing v has a similar effect to decreasing P. Moreover, if P or Q_p increases, the deposition track becomes thicker. In contrast, a faster v means that the laser spends less time in one spot, resulting in a smaller melt area and quicker cooling [36].

Given these dynamics, the study focused on the specific energy density, E. This parameter, a representation of energy applied relative to the laser spot diameter, offers a perspective independent of the system. The vital role of this energy lies in its connection to the melting interaction between the powder and the substrate, which impacts a range of properties. The E is calculated by dividing P by the product of v and the diameter of the laser spot. Although unlimited power combinations and v can yield the same specific energy value, the system operates at a maximum power of 1 kW. With the increased risk associated with higher operating temperatures in equipment dependent on heat sources, the power was set at 80 % of this maximum, according to the guidance of Cengel and Ghajar [88]. Therefore, variations in v were made to achieve the desired levels of E. This strategic emphasis on E as a factor over P and v provides a comprehensive understanding of the attributes and results of the process.

The second factor, ΔZ, represents the Z-increment of the deposition head for each subsequent layer. Achieving a layer thickness that aligns with ΔZ is pivotal, especially in scenarios without a feedback control system, which highlights the need for precise melt pool positioning [97].

The third factor examined in this study is V_{Ar}, representing the carrier gas flow rate, specifically that of Argon. This parameter is crucial to understanding the transport behavior of the powder and its subsequent deposition dynamics.

The fourth factor considered in this study is the dimensionless coefficient κ, introduced to account for the excess powder that does not contribute to the generation of the track, thus capturing deviations from the ideal scenario of no powder loss.

The last factor, O_e, is illustrated in Figure 5.1, is determined by the ratio of the distance d between the centers of consecutive tracks to D [98]. O_e stands out due to its independence from specific machine features. Instead, it is defined by the nominal diameter of the laser, positioning O_e as a universally applicable parameter. In summary, the qualitative factor O_e transforms the factorial design 2^4 into a 2^3 for two approaches, with or without track overlap. This distinction is crucial as one of the fundamental assumptions of this study is the adoption of a halved E and Q_p when constructing with O_e at 50 %, precisely because with each laser pass, 50 % of ΔZ is effectively deposited. This hypothesis is grounded in one of the most important texts in AM: *'In practice, multiple overlapping scan lines create different melt pool dynamics than single scan tracks. If the laser returns to a spot on a return pass prior*

to solidification from the previous pass, it has a similar effect to a longer dwell time (lower scan speed)" [36].

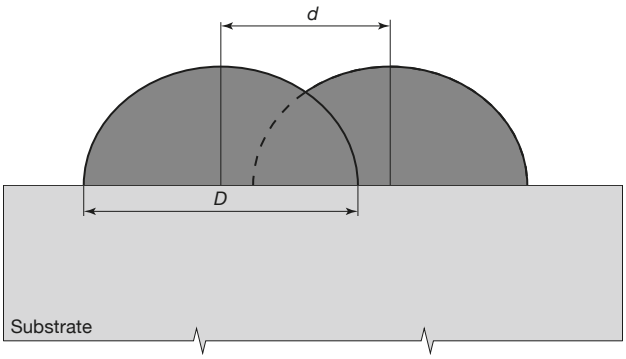

Fig. 5.1 Overlap efficiency (Oe)

The experiment involved the fabrication of 40 specimens spread over four substrates, identified as blocks. Prismatic specimens with dimensions of $(10 \times 10 \times 15.6)\,\mathrm{mm}^3$ were built on a substrate measuring $(120 \times 120 \times 7)\,\mathrm{mm}^3$. The height of 15.6 mm along the Z-axis was strategically selected to yield an integer number of layers for various ΔZ values. This choice helps to observe the growth effects of the specimen while avoiding interference of the deposition head during fabrication. Specifically, a Single Replicate design was employed with a central point for each block, considering five prominent factors, namely E, ΔZ, V_{Ar}, κ, and O_e. Prima Additive, the supplier of the DED system under investigation, provided process parameters that informed the selection of the central points. The details of the levels adopted in this experiment are detailed in Table 5.1. Since the factor O_e is qualitative

Table 5.1 Summary of process variables and their levels

Process variable	Values	Center point
$E/\mathrm{J{\cdot}mm^{-2}}$	46 – 60	53
$\Delta Z/\mathrm{mm}$	0.4 – 0.6	0.5
$V_{Ar}/\mathrm{L{\cdot}min^{-1}}$	2 – 6	4
κ	1.00 – 1.50	1.25
$O_e/\%$	0 – 50	/

rather than quantitative, it does not possess central points in the traditional sense used for numerical factors. This specialized design has a IV resolution, and the emerging alias confounds between Blocks 1, 2, and 3 with the interactions of ABC,

CDE, and ABDE. In this factor screening phase, the alias structure proves adequate. Following the sparsity principle, the focus primarily shifts to the main effects and the two-way interactions. This choice is further justified by the absence of replications, a limitation dictated by the particularly limited and high-cost resources available.

During the construction of the first block in the experimental phase, an issue was observed with the growth height of specific specimens. Four of the ten specimens examined exhibited sub-optimal growth, attaining merely half of the predicted height. Based on the previously established methodological approach, this anomaly was not associated with the powder quantity spread on the melt pool. Measurements, taken using a dedicated gauge system from the substrate to the specimen top, were essential to counterbalance potential substrate distortions and geometric anomalies. The data, which illustrates the actual height values and the growth percentage compared to nominal values, can be found in Table 5.2. A shared characteristic among all underperforming specimens was the low V_{Ar} level of $2\,\mathrm{L{\cdot}min^{-1}}$.

Table 5.2 First block Height values

Std. Order	Run Order	Position	E/ $\mathrm{J{\cdot}min^{-1}}$	ΔZ/ mm	V_{Ar}/ $\mathrm{L{\cdot}min^{-1}}$	O_e/ %	κ	Height/ %
1	**10**	**5**	**46**	**0.4**	**2**	**0**	**1.00**	**42.9**
2	**4**	**10**	**60**	**0.6**	**2**	**0**	**1.00**	**44.2**
3	3	7	60	0.4	6	50	1.00	101.3
4	8	2	46	0.6	6	50	1.00	100.0
5	2	1	60	0.4	6	0	1.50	110.9
6	6	9	46	0.6	6	0	1.50	103.2
7	**9**	**6**	**46**	**0.4**	**2**	**50**	**1.50**	**56.4**
8	**5**	**8**	**60**	**0.6**	**2**	**50**	**1.50**	**53.2**
9	1	3	53	0.5	4	0	1.25	80.8
10	7	4	53	0.5	4	50	1.25	83.7

Given these discrepancies, the experiment was halted to conduct thorough analyzes to identify, isolate, and rectify the root causes. A subsequent trial was performed on the opposite substrate side, avoiding the blocking nuisance effect that two substrate differences could cause, and also saving precious resources and money. The run order was randomized while maintaining the order of the specimen position, facilitating a better assessment of the variations of the specimen due to position. Four replications were available for both low and high gas levels. The objective was to determine whether there was an improvement in response by increasing the

low and intermediate V_{Ar} levels from 2 and 4 to 4 and 5 (L·min^{-1}) and maintaining the high level at the same. The results showed an improvement in response in all the increased low V_{Ar} levels (Table 5.3 and Fig. 5.2). Adjustments to the V_{Ar} level showed notable improvements in response.

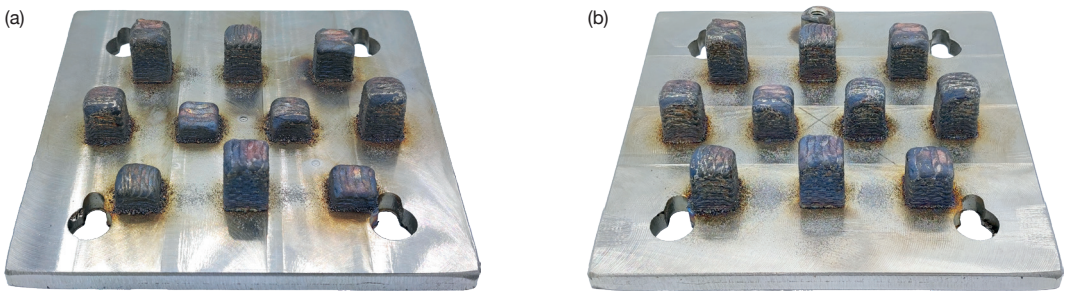

Fig. 5.2 Comparison between (a) First trial and (b) Second trial

Table 5.3 Second trial of the first block Height values

Std. Order	Run Order	Position	E/ J·min^{-1}	ΔZ/ mm	V_{Ar}/ L·min^{-1}	O_e/ %	κ	Height/ %
1	**3**	**5**	**46**	**0.4**	**4**	**0**	**1.00**	**84.0**
2	**6**	**10**	**60**	**0.6**	**4**	**0**	**1.00**	**79.8**
3	8	7	60	0.4	6	50	1.00	105.1
4	4	2	46	0.6	6	50	1.00	101.0
5	2	1	60	0.4	6	0	1.50	110.6
6	5	9	46	0.6	6	0	1.50	105.1
7	**1**	**6**	**46**	**0.4**	**4**	**50**	**1.50**	**101.1**
8	**10**	**8**	**60**	**0.6**	**4**	**50**	**1.50**	**94.6**
9	7	3	53	0.5	5	0	1.25	97.8
10	9	4	53	0.5	5	50	1.25	97.4

Moreover, to rigorously evaluate these observations, a two-sample t-test at 95 % SL between the two trials was conducted on the specimen height at low V_{Ar} levels, assuming equal variances between treatments. The subsequent analysis revealed a pronounced difference in the response between the two carrier gas levels. With a p-value less than 0.01 %, the null hypothesis was rejected, leading to the conclusion that enhancing the carrier gas level impacted the height of the specimens. This finding is also supported by the boxplot in Fig. 5.3.

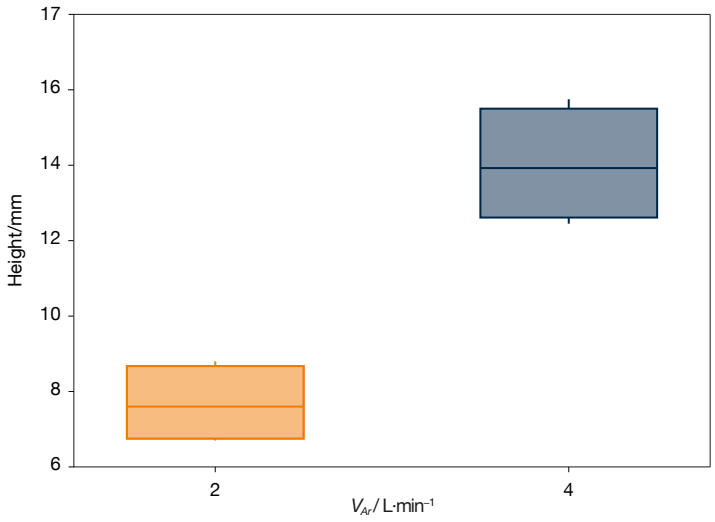

Fig. 5.3 Boxplot of the Height with respect to the V_{Ar} levels

In contrast to previous evaluations that primarily focused on measuring the mass flow rate, Q_p, the current study has shifted its attention to the actual deposition process. Consequently, the relationship between the V_{Ar} rate and the growth of depositions comes to the forefront. The initial hypothesis suggested a significant influence of V_{Ar} on the velocity of in-flight powder, which, in turn, could affect the quality of the melt pool and deposition outcomes [36]. Reducing V_{Ar} rates may compromise the melt pool's energy balance, potentially leading to the observed deposition anomalies. This phenomenon underscores the multifaceted interaction between powder stream characteristics and their translation into effective depositions.

Given these complexities, the study proposes a restructured experimental design that emphasizes the fine-tuning of V_{Ar} and κ values. The aim is to ensure the specimens attain their expected heights while addressing the newly observed factors pertinent to the deposition process. While the current investigation adopts a black-box approach, it paves the way for future research endeavors to explore the physical mechanisms that govern these interactions in greater detail.

5.2 Optimization of carrier gas flow level

5.2.1 Response variable evaluation

In assessing specimen height using the Equator^{TM} 300 precision gauging system by Renishaw (Wotton-under-Edge, UK), two distinct strategies were employed to address challenges associated with AM techniques. The first strategy aimed to compensate for the distortions typically observed in substrates of the DED method. A datum plane was interpolated by acquiring four proximal points to the specimen of interest. This locally established plane was a reference, compensating for inherent substrate distortions and ensuring accurate height determinations. The subsequent strategy addressed the complexities of quantifying the upper surface of specimens. Given the challenges, such as undulations resulting from laser traversal and pronounced surface roughness, a proper probe equipped with a large ruby sphere tip was chosen to offset these irregularities. Five reference points on the upper surface of the specimen were acquired, with four positioned at the periphery and one centralized. The average distance from these points to the established local datum accurately represented the height of the specimen.

5.2.2 Choice of experimental design

The methodology was strategically formulated in this research endeavor to delve into the intricate interconnection between powder velocity and its ensuing repercussions on the melt pool temperature without monitoring it directly. A salient aspect of this exploration is to discern how these temperature variations subsequently influence the height growth of the specimen during deposition processes. The primary hypothesis is based on the assumption that the velocity of the powder particles at their exit from the nozzle is similar to the velocity of the carrier gas:

$$v_p = v_{Ar} = \frac{Q_{cg}}{4 \cdot \pi \cdot r_{rozzle}^2} \tag{5.4}$$

where v_p is the velocity of the powder, v_{cg} is the velocity of the carrier gas, while the denominator on the right side of the equation signifies the sum of the area of the four nozzle apertures of the deposition head. Upon colliding with the melt pool on the substrate, a powder particle transfers completely his kinetic energy, E_k. This

supposes an inelastic collision in which E_k is completely transformed into thermal energy [99, 100]. The kinetic energy a particle holds prior to impact is represented by:

$$E_k = \frac{1}{2} \cdot m_p \cdot v_p^2 \tag{5.5}$$

where m_p represents the average mass of the powder, after the collision, this energy becomes zero as it merges with the melt pool, converting entirely into heat. To calculate the resulting temperature change, ΔT, in the melt pool after these impacts, the following equation is used:

$$E_k = m_{meltpool} \cdot c \cdot \Delta T \tag{5.6}$$

where $m_{meltpool}$ denotes the mass of the melt pool and c is the specific heat of the metal in a liquefied state. The individual contribution of a singular particle to the temperature variation becomes insignificant when juxtaposed with the entirety of the melt pool.

A 3^2 factorial experimental design was contemplated to embrace such potential quadratic phenomena. Among all potential factors that might influence the height of the specimens, V_{Ar} has been identified as the primary factor under investigation, complemented by the coefficient κ. All parameters not under investigation were retained at their central points, except for O_e, which was set at 50 % due to its qualitative nature. Furthermore, V_{Ar} levels were chosen to be in the vicinity of $5\,\mathrm{L{\cdot}min^{-1}}$ to approximate 100 % of the desired height. The factor levels of the experiment are detailed in Table 5.4.

Table 5.4 Process variables values used in the planned experimentation

Process variable	Values
V_{Ar}/L·min^{-1}	5 – 6 – 7
κ	1.00 – 1.25 – 1.50
E/J·mm^{-2}	53
ΔZ/mm	0.5
O_e/%	50

Three replications were selected to fully utilize the plate due to the availability of only one AISI 316L substrate of $(250 \times 250 \times 10)\,\mathrm{mm^3}$ dimensions. The distance required to avoid collisions of the deposition head between each specimen depends on

the height of the specimen itself. Therefore, a compromise had to be reached between the number of specimens to saturate the substrate, their dimensions, and the ensuing experimental power. A total of 27 cubic specimens measuring $(10 \times 10 \times 10)\,\mathrm{mm}^3$ were then built on the same substrate, and a *post hoc* power was calculated for both *Very Large* and *Huge* ES, as shown in Table 5.5.

Table 5.5 *Post hoc* computed power

Factor	df	Critical F	Power/%	
			Very Large	*Huge*
V_{Ar}	2	3.6	72	99
κ	2	3.6	72	99
$V_{Ar} \cdot \kappa$	4	2.9	57	97

5.2.3 Analysis and discussion

The experiment was conducted in one day to ensure uniform conditions (see Table E.1 in Appendix F). BCs were carefully monitored and analyzed using ANCOVA, focusing on the measured heights compared to the desired ones. Exploiting the RSM, the aim is to understand better how these factors affected the response and to achieve the desired specimen height within specific confidence limits. A fully randomized strategy was employed during creating and placing specimens on the substrate. This methodology aimed to mitigate potential systematic effects arising from several variables. One significant factor is the initial temperature of the substrate at the commencement of each deposition. Moreover, as each specimen is deposited, there is a direct alteration in the thermal characteristics of the substrate. Specifically, the thermal capacity undergoes modification, an outcome rooted in the principle that thermal capacity is derived from the product of specific heat and mass [88]. Concurrently, geometry changes in the substrate occur. Due to the deposition of specimens, the changing geometry influences the distribution of heat across the substrate and its heat exchange with the ambient convection heat transfer. An increase in free surface area generally can augment the rate of convective heat exchange [101]. Therefore, adopting this randomized strategy is pivotal in ensuring that such dynamic thermal and geometrical changes do not skew the experimental data.

Table 5.6 ANCOVA for Height/%

Source	df	Contribution/ %	Adj SS	Adj MS	F	p-value/ %
Model	10	85.37	4268.89	426.889	9.34	<0.1
Covariates	2	62.81	1781.11	890.553	19.48	<0.1
T_A	1	62.69	234.54	234.54	5.13	3.8
H_A	1	0.12	0.63	0.63	0.01	90.8
Linear	4	19.11	933.33	233.333	5.10	0.8
V_{Ar}	2	17.74	817.62	408.811	8.94	0.2
κ	2	1.37	62.86	31.432	0.69	51.7
2-Way Inter.						
$V_{Ar} \cdot \kappa$	4	3.45	172.60	43.151	0.94	46.4
Error	16	14.63	731.53	45.720		
Total	26	100				

The ANCOVA (Table 5.6) model yielded an S of 6.7 and an $R^2(adj)$ of 76.23 %, signifying the proportion of total variability in the data explained by the model when adjusted for the number of predictors. Moreover, only the V_{Ar} factor and covariate T_A influence the response at the selected SL. Furthermore, this suggests that the temperature inside the construction chamber correlates with and impacts the Height of the specimens. Specifically, as the temperature increases, there is a slight rise in the response.

In the context of this study, while the factorial plot did not provide significant insights due to only the V_{Ar} factor being influential, it was observed that, as in the first two tests, an increase V_{Ar} results in higher specimens. However, delving deeper using the Johnson transformation method and visualizing the data on a NPP sheds light on the response variability as the factor levels change. Specifically, for the factor V_{Ar}, the nonnormal distribution is evident at higher flow levels, highlighted by two unique clusters marked with orange triangles for 7 $L \cdot min^{-1}$ in Fig. 5.4. Such an irregular pattern, coupled with the broad spread of the data, points to the process's unpredictability and subsequent inconsistencies in the response.

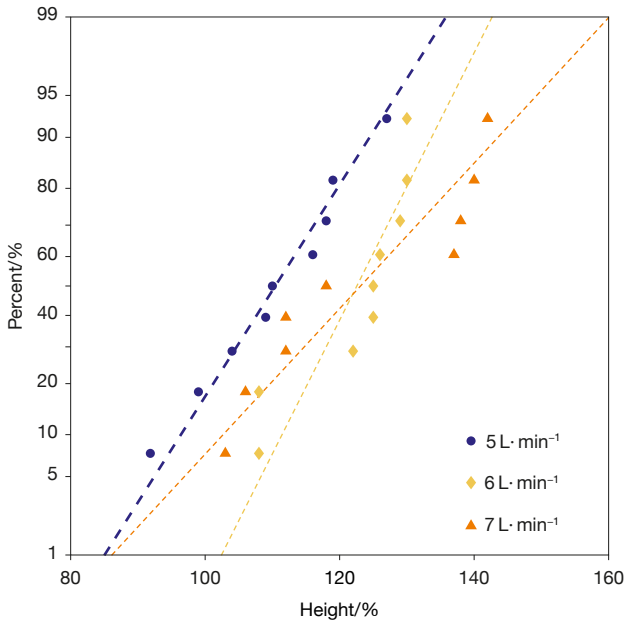

Fig. 5.4 V_{Ar} factorial plot (Johnson's method)

The next step of the analysis is focused on obtaining a model of the relationship between the process parameters and the response. A comprehensive quadratic model was selected, and a standard stepwise regression was executed to derive a model encompassing solely significant factors. The thresholds for Alpha-to-Enter and Alpha-to-Remove were designated at 10 %, facilitating the incorporation of terms nearing the 5 % SL. The result presents a linear regression formula consistent with the described methodology, incorporating the factor V_{Ar} and the covariate T_A, the latter taken only as a linear term. The regression model is:

$$\text{Height} / \% = -167.4 + 8.67 \cdot T_A + 0.2554 \cdot T_A \cdot V_{Ar} \tag{5.7}$$

It is essential to note that this equation holds within the temperature range of $(27.7 \pm 0.1)\,^{\circ}\text{C}$. Given its limited validity range, a more streamlined model was derived using the same approach without lack-of-fit. This resulted in the following regression equation in coded values, with the coefficients and their standard errors detailed in Table 5.7

$$\text{Height} / \% = 118.7 + 6.34 \cdot V_{Ar} \tag{5.8}$$

Table 5.7 Estimates of parameters of the model in coded units

Variable	Parameter	Coef	SE Coef
Constant	β_0	118.7	2.37
V_{Ar}	β_1	6.34	2.90

Given that the objective of the experiment is to achieve 100 % of the desired height, an examination of the regression equation reveals that at $5\,\mathrm{L{\cdot}min^{-1}}$, a value of (107 ± 4) % is attained. Extrapolating this data suggests that the 100 % value would be achieved at $4.04\,\mathrm{L{\cdot}min^{-1}}$, outside the resolution capability of the instrument. Given the significant variability in the data and considering that the top surface will be processed further, it was conservatively decided to set the V_{Ar} value at $5\,\mathrm{L{\cdot}min^{-1}}$. Consequently, any subsequent adjustments to reach the target height will be made solely based on other factors.

5.2.4 Conclusions

The primary objective of this research was to optimize the combinations of V_{Ar} and κ to determine the ideal height of deposited specimens in the DED system while maintaining all other process parameters constant. Utilizing a 3^k full factorial design allowed the assessment of the relationship between influential factors and the response, advancing from methodologies used in earlier studies. Advanced analytical techniques like ANCOVA, the Johnson plot, and stepwise regression within the RSM provided invaluable insights during data analysis. A series of significant outcomes emerged from this study:

- The height of the specimens predominantly depends on V_{Ar};
- The temperature inside the construction chamber, represented as T_A, appears to have some influence on the results. However, its definitive impact remains to be determined due to the restrictive range within which it was assessed;
- An evaluation of flow levels revealed no discernible difference between 6 and $7\,\mathrm{L{\cdot}min^{-1}}$;
- The lack of V_{Ar} quadratic effects challenges the initial hypothesis about kinetic energy;

- Parameters under which material deposition occurs most efficiently have been identified.

Drawing from these findings, especially the insights provided by the regression equation, the V_{Ar} factor will be maintained at a consistent $5\,\mathrm{L{\cdot}min^{-1}}$ for future experiments. Through its systematic approach, this research enhances the existing knowledge surrounding DED systems. The method introduced, which emphasizes the intricate relationship between key parameters and the resulting response, has the potential for a broad application in DED manufacturing. However, potential challenges and limitations must be recognized for further studies. The limited sample size and the use of one substrate need attention. Further explorations should consider the interplay of internal temperature and humidity within the construction chamber, especially in more varied operational ranges. In summary, this study sets a precedent for further research in this domain, suggesting refinements of the existing methodology and its potential application to diverse materials and systems.

5.3 Factor screening on mechanical characterization

5.3.1 Recognition and statement of the problem

In this research segment, the primary objective is to evaluate the robustness of previously obtained results from experiments related to powder stream and carrier gas optimization levels. There are several methodologies to achieve this; the most conventional approach involves intentionally perturbing the system to evaluate how the responses vary within the specified perturbation ranges. The purpose of this section is to serve as a connective bridge, synthesizing the insights gleaned across different experimental outcomes.

5.3.2 Responses variable evaluation

For this investigation, square-based prismatic specimens with dimensions of $(12 \times 12 \times 15.6)\,\mathrm{mm^3}$ were employed. The height of 15.6 mm in the Z-direction was deliberately chosen to ensure divisibility, resulting in an integer number of layers for selected ΔZ levels. This dimension highlights the effects of specimen growth while

preventing interference with the deposition head during construction. The dimensions of the specimen were meticulously selected to meet all response measurement prerequisites, ensuring the unhindered execution of the operations and analyzes.

Height, the first response variable, was assessed by precision gauge. Measurements were carried out locally for each specimen to accommodate potential substrate distortions, as detailed in Section 5.2.1. After height measurements, the top section of each sample was sectioned 14 mm from its substrate. It was then detached from the platform at a height of 1 mm using electrical discharge machining of wires (W-EDM). Subsequently, the lateral surfaces of these samples were removed using the Brillant 220 precision cutter by QATM (Mammelzen, GER). Following these processes, the aim is to obtain prismatic samples with approximate dimensions of $1\,\mathrm{cm}^3$.

A polishing process was followed to mitigate the potential effects of surface oxidation on subsequent density evaluations. Sample densities were determined using the ANJ-NM / ABS-N precision balance and the Ultrapyc 5000. The samples were then sectioned and embedded within the acrylic resin. After a standardized polishing regimen utilizing semi-automated rough grinding, followed by manual mirror-like polishing, image analysis rendered them suitable for porosity estimations. During this phase, 25 representative micrographs from each specimen were procured using the DMI 5000 M optical microscope by Leica (Wetzlar, GER) at a magnification factor of $100\times$. The images were analyzed using ImageJ, a public domain image processing tool developed by the National Institutes of Health. This software is renowned for its versatility and extensibility in scientific image analysis.

To conclude the series of tests, the microhardness of the samples was quantified using the JVS DHV-1000 digital micro-Vickers instrument (Licheng District, Jinan, China). Measurements were taken at two distinct positions, the first at the bottom (2 mm from the substrate) and the second at (2 mm from the substrate). This was executed using a 0.5 kgf load and a dwell time of 15 s (HV/0.5/15) [102], in accordance with the recommendations stipulated by ASTM International [103].

5.3.3 Choice of factors, levels, and ranges

Based on findings from the study on the *Optimization of carrier gas flow level* in Section 5.2.1, the equation system transitions to:

$$\begin{cases} Q_p = \kappa \cdot [R \cdot \Delta Z \cdot v \cdot D \cdot \rho_p \cdot (1 - O_e)] \\ Q_p = f(Q_{Ar} = 5\,\mathrm{L{\cdot}min^{-1}}, \omega) \\ 0.7 \leq Q_p/\mathrm{g{\cdot}m^{-1}} \leq 12.5 \end{cases} \tag{5.9}$$

The levels of experimentation, shown in Table 5.8, were selected such that the central point was aligned with those adopted in previous experiments. Only the levels of the factor κ slightly deviate from the central point of the previous experiment. Setting V_{Ar} to $5\,\mathrm{L{\cdot}min^{-1}}$ and ensuring that all specimens surpass the 100 % Height threshold, an excess of powder ranges between 25 % and 40 %. This criterion is pivotal in this study to determine whether a specimen is deemed successful or not. In addition, the ranges were adequately and assertively expanded to ensure pronounced responses. The 16 combinations of process parameters must also adhere to the constraints of the system, which are predominantly influenced by the powder stream. Indeed, the boundaries set from $(0.7$ to $12.5)\,\mathrm{g{\cdot}min^{-1}}$ for powder also serve as manufacturing limits; the system cannot achieve deposition at a rate beyond these limits. Furthermore, when factor κ is taken into account, the productivity of the system is further negatively impacted. Therefore, the production limits are not only limited to the constraints of the powder feeder, but are also dependent on the proportion of powder utilized in the construction (buy-to-fly ratio).

Table 5.8 Summary of process variables and their levels

Process variable	Low level	High level
$E/\mathrm{J{\cdot}mm^{-2}}$	46	60
O_e/%	0	50
κ	1.25	1.40
$\Delta Z/\mathrm{mm}$	0.4	0.6

In this experiment, three BCs were monitored due to their potential as disturbance phenomena. In addition to conditions inside the construction chamber, such as air temperature and absolute humidity, the substrate temperature, T_T, at time zero prior to each deposition was observed. Monitoring the temperature of the substrate is

essential. After each deposition, some residual heat remains, making it difficult to maintain uniform conditions throughout subsequent depositions. The K-type thermocouple is used to measure temperature. However, the temperature reading can be influenced due to its limited precision, accuracy, and fixed position on the substrate, especially if it is near a recently deposited specimen. Given these limitations, the substrate temperature is not used as a covariate in the analysis but rather as a monitoring system. To maintain consistency, each new deposition is started when the substrate temperature is close to the previous trial temperature, allowing for a slight variance of up to 5 °C.

5.3.4 Choice of experimental design

A two level 2^k full factorial design confounded in p blocks was chosen. Further examination uncovers that the total number of blocks is four, corresponding to the substrates. The ensuing design exhibits resolution III due to the two-way interaction BC being confounded with Block1. The two generators in this setting are the interactions BC and ABD. Such an arrangement leads to an alias structure that confounds the BC, ABD, and ACD interactions with the blocks, creating challenges in discerning whether the impact on the response comes from one interaction.

A crucial choice made during the process involved confounding κ with O_e. As substantiated in the preceding section, this decision is based on the understanding that O_e does not significantly alter one of the responses. Regrettably, for other responses, no tangible information is available. However, since this approach primarily aims at factor screening, analyzing up to the double interaction suffices. This strategy also uses the principle of effect sparsity, ensuring that the most significant influences are captured while discarding the least impactful ones.

Several critical considerations are paramount to determining the required sample size. Among these, the nominal dimensions of the specimens warrant meticulous examination. Of equal importance are the dimensions of the substrate and the precise positioning of specimens on it. Moreover, the factorial design in question significantly influences this determination. Concurrently, an assessment of the upper limit of specimens can be accommodated on each substrate without introducing interferences or complications in construction and subsequent procedures. According to the recommendations of Mathews [78], the sample size was determined using

at least two distinct methods. Given the resource constraints, conducting a pilot study to evaluate data variability proved infeasible, except for the Height response. Recognizing this limitation, several measures were taken to enhance the reliability of the experiment. The transition from a Single Replicate approach with central points to a factorial design incorporating multiple replications was instrumental. Additionally, covariates were taken into account to provide a more robust analysis. Then, the simplified formulation can be used to determine the sample size for testing the main effects:

$$n \cong \frac{1}{2^{k-2}} \left(z_{\frac{\alpha}{2}} + z_{\beta} \right)^2 \left(\frac{\sigma_{\varepsilon}}{\delta} \right)^2 \tag{5.10}$$

where n is the number of replications, k is the number of factors, $z_{\alpha/2}$ is the standard normal distribution Z-score with tail area $\alpha/2$ related to Type I error, z_{β} is the standard normal distribution z-score with tail area β related to Type II error, and σ_e/δ is the inverse of ES [93]. Z-scores were preferred over t-scores as the error degrees of freedom are sufficient to support this approximation. With an α level of 0.05, a β level of 0.2, and a *Large* ES, a total of 3 replications are necessary. It is crucial to maintain a more stringent ES in a screening design to ensure effective identification of the impact of factors on responses.

The second methodology used the G*Power software for the assessment. Power evaluations on both main effects and interactions were carried out within this computational framework, incorporating an experimental design that encompassed three replications derived from prior computations. Two covariates were incorporated into the model, excluding six terms (one two-way interaction, four three-way interactions, and a single four-way interaction). With a *Large* ES and a SL of 5 %, it was observed that both main effects and interactions share an equivalent degree of freedom. *Post hoc* power values corresponding to these conditions are meticulously presented in Table 5.9.

Table 5.9 *Post hoc* computed power

Factor	Group	df	Critical F	Power/%
Main	9+2	1	4.1	77
2-Way Interaction	9+2	1	4.1	77

5.3.5 Analysis and discussion

Each block contained twelve specimens for the study that underwent a designated treatment and was deposited entirely within a single day. Blocking can be conceptually applied to materials (substrates), distinct days, and operators. Adopting this approach is one safeguard against potential nonuniformities across tests. It is noteworthy that, upon completion of the polishing process for density measurement, all specimens exhibited volumes that were remarkably similar to each other. During the design phase, the goal was to achieve a volume of approximately $1\,\mathrm{cm}^3$ for density evaluation. The specimens obtained displayed a volume range of $(0.91 \pm 0.01)\,\mathrm{cm}^3$. This outcome is highly commendable given the extensive manual operations involved, such as cutting and polishing.

The 2-Way interaction ($\kappa \cdot O_e$) was naturally excluded from the analysis since it is completely confounded with Block1. Then factor plots and interaction plots of significant factors were constructed. Reduced models were derived using the standard stepwise method with Alpha-to-Enter and Alpha-to-Remove designated at 10 %, and response surface plots of the reduced model were generated.

The arrangement of the experiment is presented in Table E.2 (see Appendix F), divided into columns in Standard Order, Run Order, Platform Position, Block, E, ΔZ, O_e and κ. The data collected are depicted in Table E.3, which presents the results of the experiment: Height, Density, Porosity, Hardness, thermocouple temperature (T_T), air temperature (T_A), and absolute humidity (H_A). For a more concise notation of the specimens, a system was adopted in which the block number is first identified, followed by a hyphen, and then the specimen number (Run Order). This results in a designation format of Block#-S#.

Height assessment

The ANCOVA results on Height are detailed in Table 5.10. The model yielded an S of 1.0, an $R^2(adj)$ of 87.53 %, and an $R^2(pred)$ of 75.41 %. The analysis of residuals shows that they mostly follow a normal pattern. This is supported by the ADT, which indicates that the residuals are normally distributed. The plot comparing residuals and fitted values spreads the data evenly around the zero line without any noticeable trends. The latter suggests that there is consistent variance across the data. Lastly, no specific trends are observed in the observation order. These observations

Table 5.10 ANCOVA for Height/%

Source	df	Contribution/ %	Adj SS	Adj MS	F	p-value/ %
Model	14	91.24	375.413	26.815	24.56	<0.1
Covariates	2	4.32	4.407	2.204	2.02	14.9
T_A	1	2.05	4.044	4.044	3.70	6.3
H_A	1	2.27	0.990	0.990	0.91	34.8
Blocks	3	8.53	5.462	1.821	1.67	19.3
Linear	4	74.43	304.783	76.196	69.79	<0.1
E	1	1.61	8.211	8.211	7.52	1.0
κ	1	2.47	12.820	12.820	11.74	0.2
O_e	1	25.85	95.684	95.684	87.64	<0.1
ΔZ	1	44.49	185.106	185.106	169.54	<0.1
2-Way Inter.	5	3.96	16.296	3.259	2.99	2.5
$E \cdot \kappa$	1	1.64	6.859	6.859	6.28	1.7
$E \cdot O_e$	1	0.05	0.196	0.196	0.18	67.4
$E \cdot \Delta Z$	1	0.12	0.416	0.416	0.38	54.1
$\kappa \cdot \Delta Z$	1	1.15	4.660	4.660	4.27	4.7
$O_e \cdot \Delta Z$	1	1.01	4.162	4.162	3.81	5.9
Error	33	8.76	736.030	1.092		
Total	47	100				

lead us to conclude that the model is suitable. On examination, it is evident that no covariate significantly affects the response within the acquired ranges. This aligns with the findings and the strategy adopted in the *Optimization of carrier gas flow level*, thereby validating the decision to exclude this covariate from the optimization process. Interestingly, the Blocks also prove to be not significant.

About 74% of the data variability comes from the main effects, all significant to the chosen SL. The ΔZ is the most influential main effect, contributing to about 44.5 % of the variability, as confirmed by its p-value. The latter suggests that the number of layers into which the desired geometry is sliced directly influences the Height. As Fig. 5.5 illustrates, increasing ΔZ values, which means fewer layers, lead to a noticeable reduction in Height. This can potentially be attributed to the layer-by-layer additive effect of the surplus material on the response. Such findings align well with hypotheses and decisions drawn from the results of the preceding section. O_e holds the position as the second most significant main effect. Its SS contributes to around 25.8 % of the data variability. The response is significantly influenced by O_e,

as evidenced by its p-value being lower than the minimum resolution of the software. An increase in the response is observed when specimens are constructed with an O_e of 50 %, implying that the specimen is constructed over double the laser scanning passes. This effect is prominently displayed in the factorial plot (Fig. 5.5). The κ coefficient emerges as the third significant main effect. A tangible explanation for this is that when more powder is provided to the melt pool at higher levels, an increment in Height is realized. The main effect of least prominence is E. Specifically, as the specific energy supplied to the melt pool increases, the average height of the specimens also rises. This phenomenon can be attributed to the enhanced ability to melt and trap more powder. Indeed, a higher E in this study implies a reduced v.

Among the two-way interactions, depicted in Fig. 5.6, $E \cdot \kappa$ and $E \cdot \Delta Z$ can be identified. Specifically, for the interaction between E and κ, high values of both E and κ are observed to result in an increased response. The latter supports the hypothesis that an increase in E manages to melt a greater amount of powder. Regarding the interaction between $E \cdot \Delta Z$, as ΔZ increases, meaning a reduction in the number of layers, there is a decrease in Height, and for high values of E, the response increases. Although it does not meet the chosen SL, the interaction between $O_e \cdot \Delta Z$ should still be considered. In fact, its p-value is borderline, and, as with their respective main effects, the height also increases as O_e and the number of layers increases.

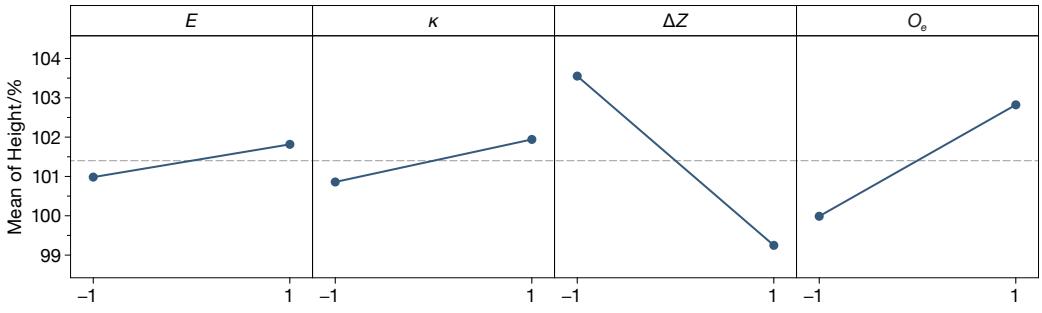

Fig. 5.5 Main effects plots for Height/%

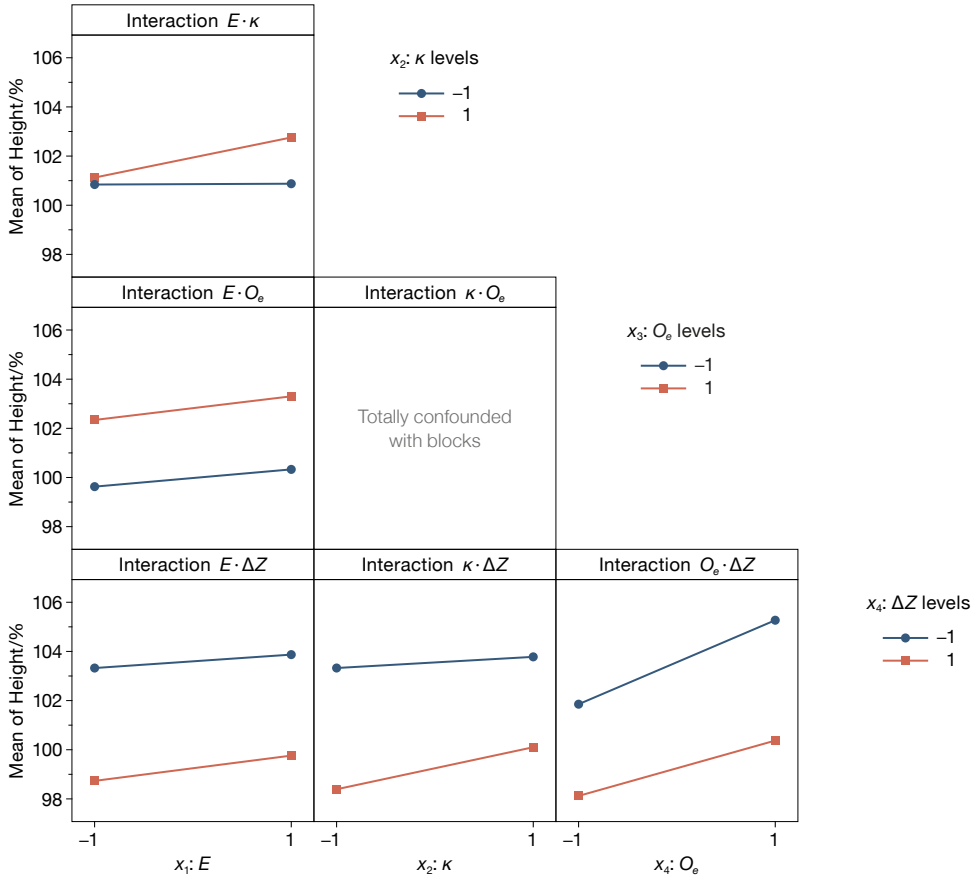

Fig. 5.6 Interaction plots for Height/%

After identifying the active factors through ANCOVA, they were used to derive a reduced model using the standard stepwise regression without hierarchical model terms, setting the SL at 10 %. This resulted in the following equations for the two levels of O_e in coded units are:

$$\begin{aligned} \text{Height}/\% = {} & 100.000 + 0.440 \cdot E + 0.448 \cdot \kappa + \\ & - 1.844 \cdot \Delta Z + 0.501 \cdot E \cdot \kappa + 0.352 \cdot \kappa \cdot \Delta Z \quad (O_e = 0\,\%) \end{aligned} \tag{5.11}$$

$$\begin{aligned} \text{Height}/\% = {} & 102.799 + 0.440 \cdot E + 0.448 \cdot \kappa + \\ & - 2.414 \cdot \Delta Z + 0.501 \cdot E \cdot \kappa + 0.352 \cdot \kappa \cdot \Delta Z \quad (O_e = 50\,\%) \end{aligned} \tag{5.12}$$

The metrics, including an S value of 1.1, an $R^2(adj)$ of 87.3 %, and an $R^2(pred)$ of 83.2 %, highlight the robustness and precision of the developed model. Furthermore, an analysis of the residuals supports this, revealing no significant anomalies or signs of LOF, further confirming the reliability of the model. From the system of equations,

presented in coded units and averaged across blocks, it is evident through the constant term that the average of the samples constructed with 50 % O_e is higher than those constructed without. The response trend, on the other hand, remains consistent for both construction strategies. Utilizing coded units allows for a straightforward interpretation of the regression coefficients, elucidating the impact of both the factor and the interaction. Notably, all the standard errors are identical, a characteristic of the regressors in a 2^k design. The values of the coefficients, alongside their respective standard errors, are detailed in Table 5.11.

Table 5.11 Estimates of parameters of the model in coded units

Variable	Parameter	Coef	SE Coef
Constant ($O_e = 50\,\%$)	β_0	101.400	0.152
Constant ($O_e = 0\,\%$)	β_0	100.000	0.152
E	β_1	0.441	0.152
κ	β_2	0.448	0.152
ΔZ	β_4	-2.129	0.152
$E \cdot \kappa$	β_{12}	0.501	0.152
$\kappa \cdot \Delta Z$	β_{24}	0.352	0.152
$\Delta Z \cdot O_e$ ($O_e = 0\,\%$)	β_{42}	0.285	0.152

Lastly, the contour plots of the response for the two qualitative levels of O_e are illustrated in Fig. 5.7.

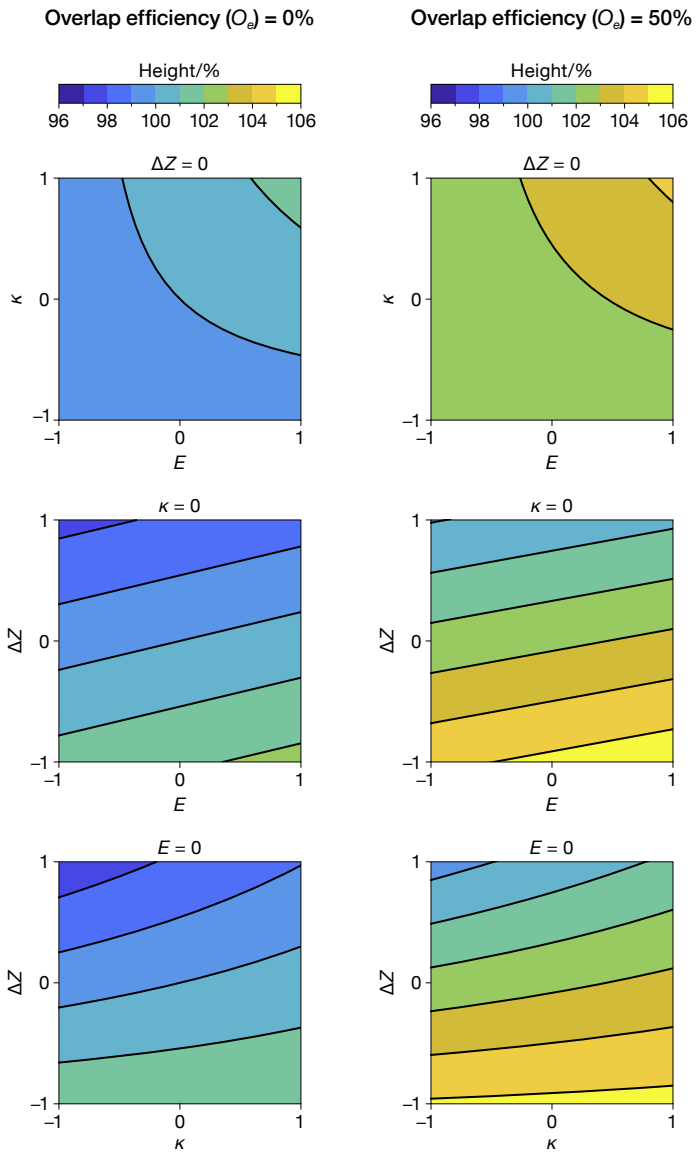

Fig. 5.7 Contour plots for the two qualitative levels of O_e for Height/%

Density assessment

In exploring specimen density as a response variable, findings provide intriguing insights. The model yielded an S of 0.01, an $R^2(adj)$ of 55.04 %, and an $R^2(pred)$ of 23.37 %. From the ANCOVA results about Density (Table 5.12) indicate that only the blocks exhibited a significant systematic effect. At this screening stage, pinpointing the exact cause of this effect remains challenging. Several reasons might explain this

Table 5.12 ANCOVA for Density/(g·cm^{-3})

Source	df	Contribution/ %	Adj SS	Adj MS	F	p-value/ %
Model	14	68.43	0.014927	0.001066	5.11	<0.1
Covariates	2	53.20	0.000764	0.000382	1.83	17.6
T_A	1	3.89	0.000012	0.000012	0.06	81.0
H_A	1	49.32	0.000759	0.000759	3.64	6.5
Blocks	3	11.22	0.002269	0.000756	3.62	2.3
Linear	4	1.29	0.000267	0.000067	0.32	86.2
E	1	0.55	0.000114	0.000114	0.55	46.4
k	1	0.00	0.000001	0.000001	0.00	95.0
O_e	1	0.43	0.000096	0.000096	0.46	50.2
ΔZ	1	0.31	0.000053	0.000053	0.25	61.7
2-Way Inter.	5	2.71	0.000592	0.000118	0.57	72.4
$E \cdot k$	1	0.10	0.000018	0.000018	0.08	77.3
$E \cdot O_e$	1	1.11	0.000232	0.000232	1.11	29.9
$E \cdot \Delta Z$	1	0.00	0.000002	0.000002	0.01	92.3
$k \cdot \Delta Z$	1	0.67	0.000149	0.000149	0.71	40.4
$O_e \cdot \Delta Z$	1	0.83	0.000181	0.000181	0.87	35.8
Error	33	31.57	0.006886	0.000209		

phenomenon. It could stem from one or more high-order interactions confounded within the blocks. Alternatively, discrepancies in the substrates could be at play. Another possibility is that each block was constructed on different platforms and days, leading to the observed variations. Given that the data are normally distributed, further confirmed by the ADT, such a variability in density might be attributed merely to process variability. Once again, Occam's razor provides guidance: the simplest explanation is most likely correct. This suggests that all specimens exhibit consistent density within the selected process parameter window with the designated evaluation system. This consistency lends credence to the equation system developed to correlate the construction parameters Q_p, and the powder transport system.

Upon further examination of the density values, the observed value[1] stands at (7.927 ± 0.006) g·cm^{-3}. When comparing this result with the density of the virgin powder using a one-sample t-test, where the null hypothesis states that the density

[1]Values were calculated based on the sample of 48 specimens, with the standard error multiplied by a coverage coefficient determined using the t-student distribution with 47 degrees of freedom and two-tailed 5 % (α) SL.

of the powder is equal is equal to specimen one, the hypothesis is rejected with a p-value lower than 0.01 %. The latter implies that a portion of the porosity inherent in the powder is eliminated during the construction process (see Fig. 5.8). Further bolstering the above findings, several crucial observations were made about the sample of 48 specimens. In particular, there are no data outliers that could adversely influence the test results. Moreover, the null hypothesis concerning the non-normality of the density of the specimens cannot be rejected, emphasizing the uniformity of the density of the sample. Given the sufficiently large sample size, it is adept at discerning the difference from the average density of the powder. These satisfied assumptions collectively reinforce the conclusions stated above.

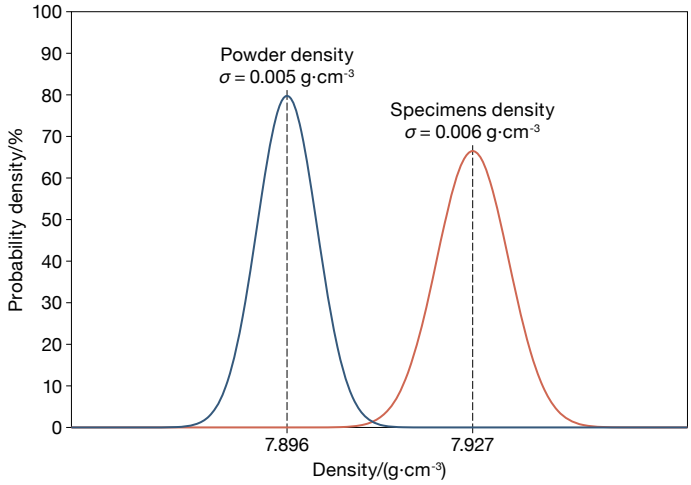

Fig. 5.8 Comparison between powder and specimens densities

Porosity assessment

The distribution of the Porosity data deviates from the expected normality, as evidenced in Fig. 5.9. Although there are two distinct clusters within the NPP, they have not been labelled as outliers.

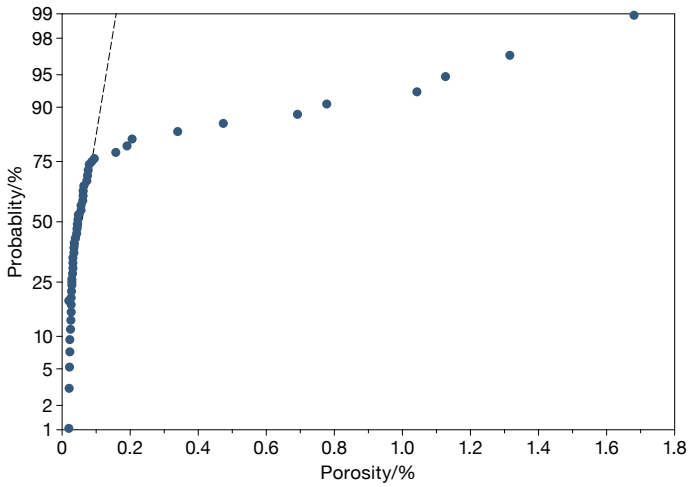

Fig. 5.9 NPP for the Porosity/%

This is particularly due to the secondary cluster that contains nine to eleven values, which is approximately 19 % to 23 % of all observations. This grouping cannot be associated with any specific factor or level, necessitating a distinct analytical approach. To ensure a normal distribution, which is essential for the proper application of ANOVA/ANCOVA, the Box-Cox transformation method was used [104]. The method is employed to address non-normal, positive data sets. Given that porosity inherently holds values greater than 0, this technique proves particularly appropriate for the case under consideration. Because of this iterative procedure, a rounded λ value of -0.5 was derived, subsequently leading to the transformation of data using the inverse square root, represented by the equation:

$$Y = Y^{-0.5} = \frac{1}{\sqrt{Y}} \tag{5.13}$$

Following this transformation, the ADT lead a p-value greater than 5 %, suggesting that the newly transformed data has a normal distribution, making it suitable for the subsequent statistical procedures.

The ANCOVA was conducted on transformed data (as shown in Table 5.13), and the resulting model exhibited a non-significant p-value. In the context of ANOVA and ANCOVA, a non-significant p-value challenges the tested hypotheses. Essentially, the null hypothesis posits no significant differences between the compared groups. This result could stem from an ES that is too subtle for our sample size to discern or from limitations in the current measurement system and technique.

Table 5.13 ANCOVA for transformed Porosity/%

Source	df	Contribution/ %	Adj SS	Adj MS	F	p-value/ %
Model	14	41.77	143.821	10.2730	1.69	10.6
Covariates	2	1.61	19.937	9.9687	1.64	20.9
T_A	1	1.03	0.032	0.0318	0.01	94.3
H_A	1	0.58	18.787	18.7867	3.09	8.8
Blocks	3	9.23	24.570	8.1899	1.35	27.6
Linear	4	7.46	22.159	5.5396	0.91	46.9
E	1	0.22	1.042	1.0419	0.17	68.1
k	1	2.07	4.265	4.2648	0.70	40.8
O_e	1	3.92	14.559	14.5590	2.40	13.1
ΔZ	1	1.25	2.781	2.7808	0.46	50.3
2-Way Inter.	5	23.47	80.830	16.1660	2.66	4.0
$E \cdot k$	1	0.00	0.373	0.3733	0.06	80.6
$E \cdot O_e$	1	1.41	5.966	5.9657	0.98	32.9
$E \cdot \Delta Z$	1	14.19	46.986	46.9858	7.73	0.9
$k \cdot \Delta Z$	1	5.84	19.959	19.9594	3.28	7.9
$O_e \cdot \Delta Z$	1	2.03	6.999	6.9987	1.15	29.1
Error	33	58.23	200.517	6.0763		
Total	47	100				

Considering this, a more advanced measurement technique, such as computed tomography (CT) scans, might offer a detailed insight on porosity. One of the inherent limitations of the current method is that it examines a single section, whereas the material potentially has infinite sections. The porosity of a given section could be influenced by its unique positioning within the whole. To substantiate these claims, a correlation study was conducted. Intuitively, an increase in porosity would decrease mass, then in density, implying a negative correlation coefficient (in an ideal case $r = -1$). As depicted in Fig. 5.10, the scatterplot does not display a trend suggestive of a negative correlation. A notable concentration of data points is observed at lower porosity values. When executing the Pearson correlation test between the density and porosity of the specimens, with a SL set at 5 %, a p-value of 19.2 % was obtained. Thus, the hypothesis suggesting a correlation between the two variables is rejected. This outcome aligns with our prior assertions, as it contradicts fundamental principles of physics. Building on the abovementioned observation, when isolating and re-executing the correlation test on the subset of these 9 data points (colored in

red in the Fig. 5.10), an r-value of -0.94 is derived. This pivotal result underscores that analyzing porosity on a section using an optical microscope may not adequately represent the comprehensive porosity of the entire specimen.

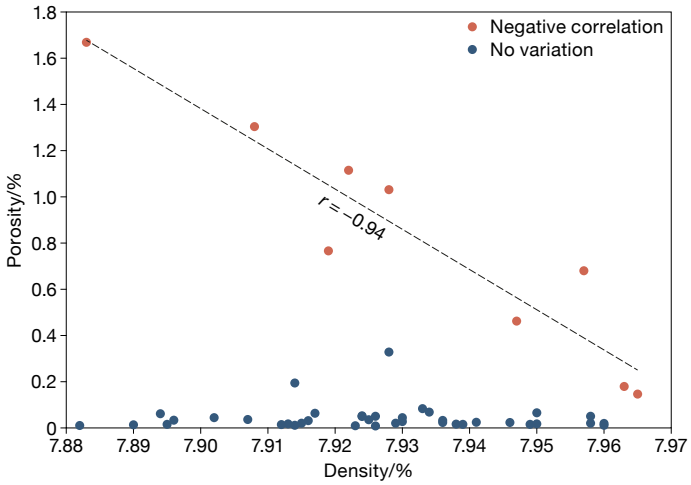

Fig. 5.10 Matrix plot of the Density/(g·cm^{-3}) vs. Porosity/%

Hardness assessment

Results from Table 5.14 indicate that the ANCOVA analysis validates the significance of the model. Neither covariates nor blocks appear to influence the response. Examination of the residuals reveals a normal distribution without discernible patterns. The regression analysis yields an S of 2.7 and a $R^2(adj)$ value of 30 %. This infers that the devised model elucidates 30 % of the observed variance in the dependent variable and underscores that a significant 70 % remains elusive. This discrepancy might arise from methodological errors, inherent variability in the studied phenomena, or other unconsidered factors. Such considerations are crucial when contextualizing the broader implications of this research. A noteworthy observation is the $R^2(pred)$ value of zero. This value underscores the predictive incapability for new data points of the model. Therefore, the primary utility of this model lies in discerning factors that influence hardness, a parameter intrinsically linked to Young's modulus, an essential measure in engineering materials studies.

A comprehensive evaluation reveals that all four main effects have a marked contribution, cumulatively accounting for 29 % of the model. Factor E emerges as the most predominant, succeeded by κ and O_e in terms of influence. Among

Table 5.14 ANCOVA for Hardness/(HV/0.5/15)

Source	df	Contribution/ %	Adj SS	Adj MS	F	p-value/ %
Model	14	51.37	248.502	17.7502	2.49	1.6
Covariates	2	0.40	15.966	7.9829	1.12	33.8
T_A	1	0.32	13.905	13.9051	1.95	17.2
H_A	1	0.08	0.430	0.4297	0.06	80.8
Blocks	3	9.26	32.492	10.8307	1.52	22.8
Linear	4	29.26	132.091	33.0228	4.63	0.4
E	1	12.15	56.406	56.4056	7.91	0.8
k	1	8.50	30.496	30.4963	4.28	4.7
O_e	1	8.26	41.836	41.8356	5.87	2.1
ΔZ	1	0.35	1.839	1.8386	0.26	61.5
2-Way Inter.	5	12.46	60.263	12.0526	1.69	16.4
$E \cdot k$	1	5.50	29.485	29.4848	4.14	5.0
$E \cdot O_e$	1	1.75	8.886	8.8860	1.25	27.2
$E \cdot \Delta Z$	1	1.78	8.075	8.0750	1.13	29.5
$k \cdot \Delta Z$	1	2.36	11.331	11.3314	1.59	21.6
$O_e \cdot \Delta Z$	1	1.06	5.112	5.1119	0.72	40.3
Error	33	48.63	235.276	7.1296		
Total	47	100				

the main effects, ΔZ registers as the least consequential. Regarding the two-way interactions, only $E \cdot \kappa$ appears to influence the response.

When examining the factorial plots (Fig. 5.11), it is evident that an increase in E leads to a significant reduction in hardness. This suggests that greater energy increases heat provision, affecting the cooling rates and grain growth coefficients. Such changes inevitably alter the microstructure of the specimens. This observation is consistent with established scientific findings such as the Hall-Petch law [105]. In contrast, a rise in the value κ tends to decrease hardness, probably due to phenomena related to thermal source attenuation. An O_e value of 50 % results in a stark decline in hardness. Given the initial assumptions, where E is halved during the construction with overlap, this phenomenon can be attributed solely to the double passage of the thermal source at each point. The total summation of power to construct a specimen with O_e, keeping E and ΔZ constant, remains unchanged. Lastly, decreasing the number of layers, or increasing ΔZ, leads to an enhanced hardness, which aligns

with expectations. The overall energy provided is less since E is surface-focused rather than volumetric.

Regarding interactions (Fig. 5.12), it is noteworthy that only the interaction between E and κ is significant. As mentioned above, this results in a greater fusion of powders. Specifically, at low κ values and increasing E, there is a significant reduction in hardness. This effect is not as pronounced for high κ values, implying that the surplus powder utilizes some energy to undergo a phase change from solid to liquid.

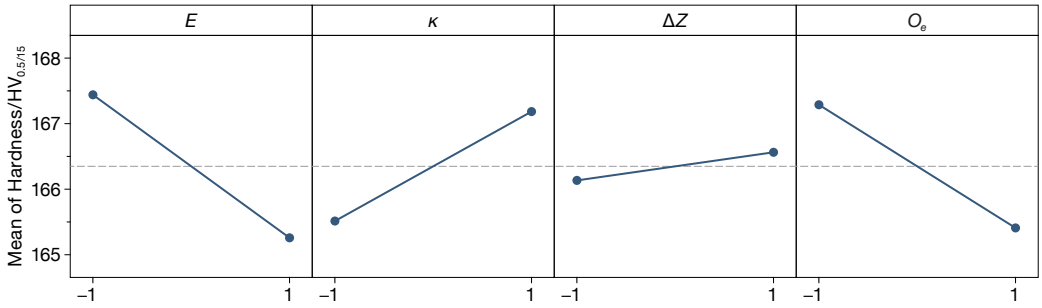

Fig. 5.11 Main effects plots for Hardness/(HV/0.5/15)

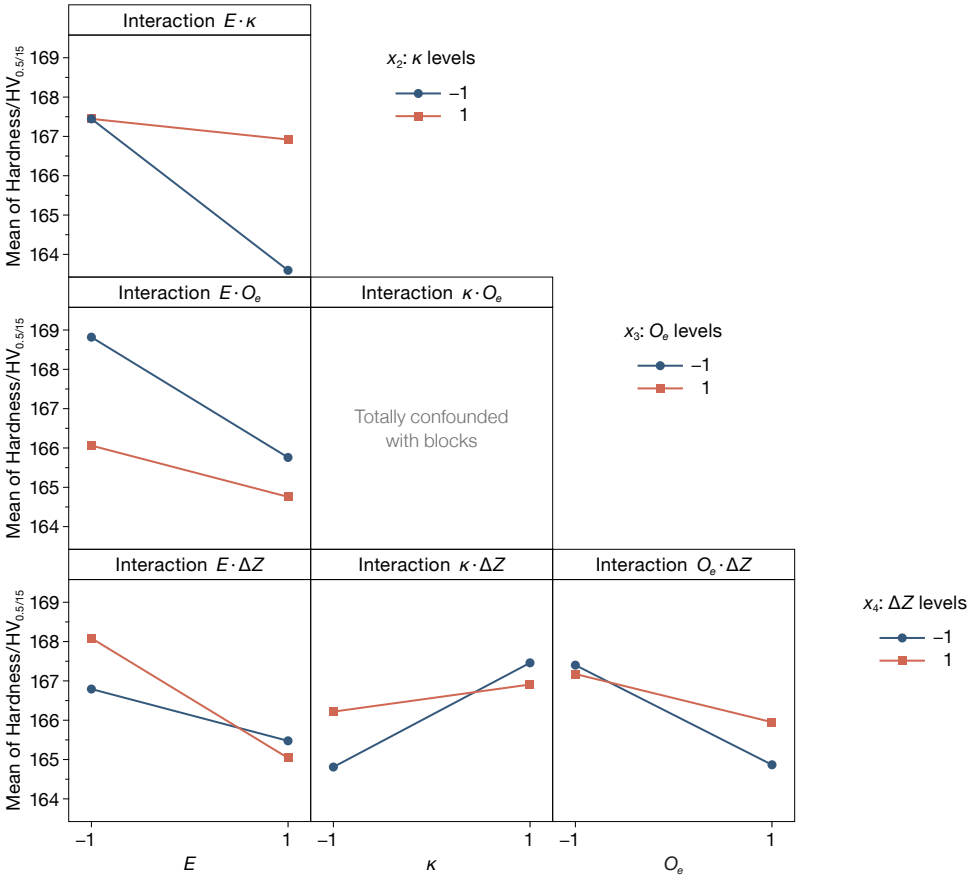

Fig. 5.12 Interaction plots for Hardness/(HV/0.5/15)

The reduced model using the standard stepwise regression without hierarchical model terms, setting the SL at 10 %. This resulted in the following equations for the two levels of O_e in coded units are:

$$\begin{aligned}\text{Hardness/(HV/0.5/15)} &= 167.352 - 1.027 \cdot E + \\ &\quad + 0.715 \cdot \kappa + 1.010 \cdot E \cdot \kappa \quad (O_e = 0\,\%) \qquad (5.14)\\ \text{Hardness/(HV/0.5/15)} &= 165.345 - 1.027 \cdot E + \\ &\quad + 0.715 \cdot \kappa + 1.010 \cdot E \cdot \kappa \quad (O_e = 50\,\%) \qquad (5.15)\end{aligned}$$

The latter yielded an S value of 2.7, an $R^2(adj)$ of 35.6 %, and an $R^2(pred)$ of 19.8 %. Issues related to residuals were not observed, and no signs of LOF were evident. Despite the limited applicability of the model, it provides a qualitative wealth of information that will be invaluable for future studies. Generally speaking, when examining the coefficients of the model, it can be inferred that given the same energy

provided to the specimen, constructing with overlap results in reduced hardness. Regression coefficients and their standard errors are presented in Table 5.15.

Table 5.15 Estimates of parameters of the model in coded units

Variable	Parameter	Coef	SE Coef
Constant ($O_e = 50\,\%$)	β_0	165.345	0.388
Constant ($O_e = 0\,\%$)	β_0	167.352	0.388
E	β_1	-1.027	0.388
κ	β_2	0.715	0.388
$E \cdot \kappa$	β_{12}	1.010	0.388
$\Delta Z \cdot O_e$ ($O_e = 0\,\%$)	β_{42}	0.285	0.388

Lastly, the contour plots of the response for the two qualitative levels of O_e are illustrated in Fig. 5.13.

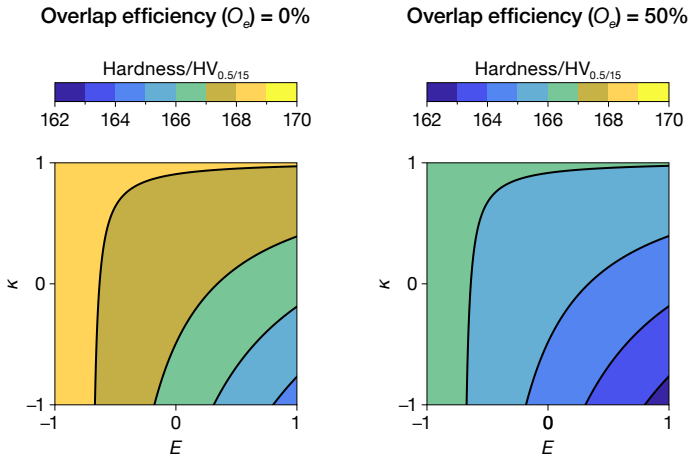

Fig. 5.13 Contour plots for the two qualitative levels of O_e for Hardness/(HV/0.5/15)

Building on the previous analysis, an evaluation was conducted contrasting each top five and bottom five points of each specimen. Subsequently, a two-sample t-test was executed, assuming equal variances. The findings suggest that with the exceptions of the specimens Block3-S2, Block4-S3, and Block1-S6, hardness at the top of the specimens is typically diminished compared to the bottom, corroborating Moheimani et al. [106]. ANOVA was then undertaken to ensure that such disparities were not associated with the selected factor levels or test assumptions. The ANOVA substantiated that the observed variations were linked to the specific case (either the process or the test) and could not be rationalized by the existing data set.

5.4 Linking the process parameters to the properties of the deposition

This thesis culminates in the development of a user-friendly framework to comprehensively guide the user through various aspects of process optimization and experimental data regression (see Appendix F) exploiting the Matlab software by MathWorks Inc. (Natick, Massachusetts, USA). The code is systematically divided into distinct sections, beginning with the crucial elements of the powder stream processes, followed by regression of experimental data. The code subsequently prompts the user to specify desired process parameters, providing options to focus on travel speed or specific energy. Moreover, it accommodates two approaches - operating with or without O_e - and leverages optimized response surface models for layer height to calculate the required powder mass flow rate (Q_p).

Powder stream process

This subsection is designed to serve as an instrumental guide for the experimenter, facilitating the assessment of the constraints and operational ranges of the powder feeder system. The investigation employs a rigorous methodology tailored to address the complexities inherent in powder stream systems. The scope of this inquiry is specifically limited to the study of disk rotational speed (ω) as a single influential factor. This particular focus arises from the conclusions drawn in Section 5.3.5, which stipulated a constant carrier V_{Ar} of $5\,\mathrm{L{\cdot}min^{-1}}$. In this context, the code is engineered to zero in on the determination of Q_p, elucidating its relationship with the rotational speed of the powder feeder system. The code is organized into the following steps:

1. User input for ω
2. Data validation for number of levels
3. Defining the range for ω
4. Calculating increment and levels of the factor
5. Query for the number of replicates

6. Generating the final ω vector
7. User option to view randomized test order
8. Randomization of experimental order
9. Post-experiment data input for Q_p
10. Creation of a data table for regression
11. Stepwise regression analysis
12. Displaying the selected model
13. Coefficient refinement
14. Regressors visualization
15. Predictive analysis

The first crucial step in the code requires the user to specify the number of levels for ω that will be studied. A minimum of 2 levels is necessary for conducting a linear regression analysis. However, a minimum of 3 levels is suggested to fit a quadratic model, which provides a more nuanced understanding of the relationship between the variables. The user input here significantly affects the resolution and breadth of subsequent experiments and analyses. After collecting the number of levels from the user, immediate validation is performed to ensure that at least 2 levels have been entered. This validation step is critical to preempt potential mathematical errors or inconsistencies at later stages of data analysis. It serves as an initial checkpoint to guarantee the suitability of the data for regression analysis.

Upon validation, the code asks the user for the minimum and maximum ω values. Determining the range of ω allows the code to calculate the increment ($\Delta\omega$) between each level, facilitating a uniform distribution of data points. This step is crucial in ensuring that the experiment covers a sufficiently wide span of the focus variable, making the findings more generalizable and robust. The increment between the speed levels is then calculated, generating a vector of rotational speed levels (ω_levels). This computed vector provides the experimental settings at which the factor of interest, rotational speed, in this case, will be tested.

The code then queries the user to specify the number of replicates for each ω level. Replication is indispensable in experimental design, as it allows for assessing experimental error and increases the reliability of the findings. The user is advised to conduct at least 5 replicates, enhancing statistical power in testing the slope coefficient of the linear regression. A final vector for ω is created on the basis of the levels and replicates. This vector is then displayed to the user, serving as a comprehensive guide to the levels of ω that will be evaluated in the experiment.

Randomization is an integral part of experimental design, mitigating the influence of extraneous variables and minimizing systematic error. A random index is generated and the vector ω is reordered based on this index, leading to $\omega\_randomized$. Finally, the user is asked whether they want to view the randomized test order. If the user opts to view it, the randomized vector is displayed. This step adds a layer of transparency, allowing the researcher to be fully aware of the sequence in which the experimental runs will be conducted. After the experiments, the user must manually enter the Q_p data obtained for each test following the Standard Order sequence.

After input of experimental data, the code constructs a data table explicitly designed for regression analysis. The organization of this data table provides the foundation for efficient and accurate statistical analyzes, ensuring the readiness of the data for complex algorithms to be applied subsequently. The next computational operation performed by the code is stepwise regression analysis. This technique iteratively evaluates the statistical significance of each predictor variable in the model, in this case, ω, and its potential linear and quadratic terms. It adds or removes terms based on statistical criteria to optimize the fit to the experimental data of the model. The outcome is a model that effectively captures the inherent relationships among the variables while simultaneously minimizing the risk of overfitting. Upon completion of the stepwise regression analysis, the code outputs the selected regression model for review. This transparent display of the model allows the experimenter to gain immediate insights into which predictor variables, and in what mathematical form, have a statistically significant impact on the response. In subsequent steps, the code refines the model coefficients to improve predictive accuracy. In this refinement phase, the insignificant coefficients are rounded to zero, simplifying the model without sacrificing significant predictive power. An illustration of the results returned by the Matlab code, employing the pre-set default vectors based on experimental trials with the powder feeder is presented below in the Command Window and depicted in Fig. 5.14:

```
1. Removing Omega^2,
FStat = 0.26923,
pValue = 0.62242
Optimized Model:
Linear regression model:
    Qp ~ 1 + Omega

Estimated Coefficients:
Estimate    SE  tStat   pValue
(Intercept) -0.12639    0.18342 -0.68906    0.51297
Omega   0.44375 0.015356    28.897  1.5296e-08

Number of observations: 9,
Error degrees of freedom: 7
Root Mean Squared Error: 0.301
R-squared: 0.992,  Adjusted R-Squared: 0.99
F-statistic vs. constant model: 835,
p-value = 1.53e-08

Model Coefficients:
   -0.1264
    0.4437
```

The experimenter is presented with the option of visualizing the regression model through a graph. Opting to execute this function will generate a plot that graphically represents the relationship between the predictor and the outcome variables. This graphical representation is beneficial for qualitative assessment and assists in presenting the findings in a more digestible format for both technical and non-technical audiences. Lastly, the code leverages the final selected model for predictive analysis. Using the experimentally determined range of ω, it calculates the minimum and maximum Q_p values that can be expected. These predicted values are then displayed, offering the researcher comprehensive information about the behavior of the system within the experimental constraints.

It is important to note the limitations in the applicability of this approach. Although the method has shown robustness within the explored constraints, meaning

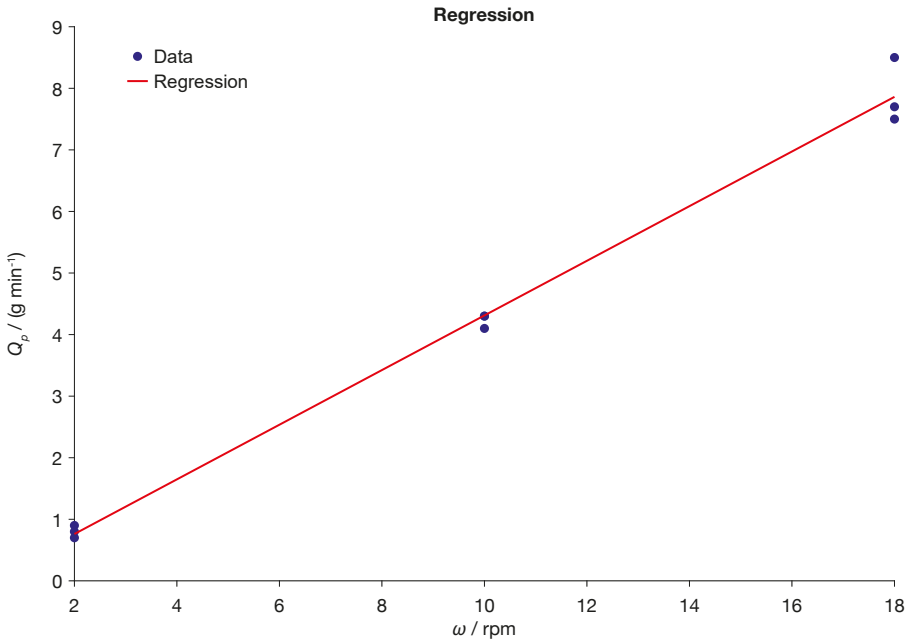

Fig. 5.14 Regression plot example

that it is reliable for interpolation within these limits, its validity becomes uncertain when extrapolating beyond these boundaries. Consequently, individual operators should recalibrate the method based on the specifics of their system, mainly when operating outside of the previously established limits.

Process parameters

This subsection elucidates the computational aspects of determining various process parameters crucial for DED-LB/Powder. It begins by defining initial settings and proceeds through multiple steps, including user input, validation checks, computational procedures, and output generation. The aim is to comprehensively determine and validate parameters such as overlap, laser beam power, scan speed, and energy density, which are indispensable for achieving precision and reliability in the subsequent manufacturing processes. The code is structured into the following steps:

1. Initialization of parameters
2. User choice for v or E

3. Validation and calculation
4. Energy layer adjustment
5. Powder feed rate calculation
6. Validation of Q_p
7. Equation solving for ω
8. Output

In the initial segment of this code, a set of predetermined parameters is established to serve as the framework for the DED-LB/Powder technique. These parameters include O_e, P, ΔZ, D, ρp, and the desired layer height as a percentage (H). These variables are hard-coded (see the example code below), thus serving as the foundation for the remaining calculations and decisions.

```
%%%%%%%%%%%%%%%%%%PROCESS PARAMETERS%%%%%%%%%%%%%%%%%%
% Input
Oe = 0;  % 50 if we are using 50% overlap, otherwise
   without overlap with any other number
P = 750;  % Laser Beam power in W
DeltaZ = 0.5; % value between 0.4 mm and 0.6 mm
D = 2;  % Laser beam diameter in mm
rho = 7.896e-3;  % Powder density in g*mm^{-3}
H = 100;  % Height of the desired layer in percentage
```

Following this, the code requests the user choose between v (scan speed) or E (energy density). This choice reflects the methodology applied in the ensuing calculations and affects how subsequent variables will be determined. If v is selected, its value must be entered, setting E to an undefined status (NaN). Conversely, selecting E requires its value to be entered, and v is then set to NaN. An error message is generated for invalid input, ensuring data integrity. A series of conditional checks are performed upon choosing between v and E. If v is numeric, E is calculated using a predefined formula involving laser beam power, scan speed, and diameter. The overlap condition is also accounted for, effectively doubling the energy per layer if a 50 % overlap is specified. When E is selected, the same computational rigor is applied, where v is computed using an equivalent formula. The next part of the code

is dedicated to calculating the powder feed rate ($Q_p\_calculated$). A distinct formula is used depending on whether there is an overlap. The computed $\kappa\_calculated$ value used in this calculation is set to a minimum of 1 if it falls below this threshold.

The code then checks if the computed powder feed rate is within a predefined feasible range, issuing a warning if not, informing the user to reconsider the geometric parameters. Lastly, a symbolic variable *Omega_sym* is declared to formulate a quadratic equation. This equation is then solved to obtain $omega\_calculated$, the computed value of rotations. Based on the specific conditions, such as overlap and other variables, the code outputs calculated values for E, $k\_calculated$, v, and $Q_p\_calculated$. The computed process parameters resulting from the Matlab code (see Fig. 5.15) are displayed in the Command Window as follows:

```
1 The calculated value of Rotations is: 12.3 rpm
2 The surplus of powder k spread on the melt pool is:
     1.20
3 The input of E is: 40.0 J/mm^2
4 The calculated value of v based on the specific
     energy supplied is: 562.5 mm/min
5 The calculated value of Qp is: 5.3 g/min
```

In summary, this subsection of the code is an essential mechanism for determining and validating key process parameters, effectively laying the groundwork for a robust and reliable additive manufacturing process, based on factor screening results.

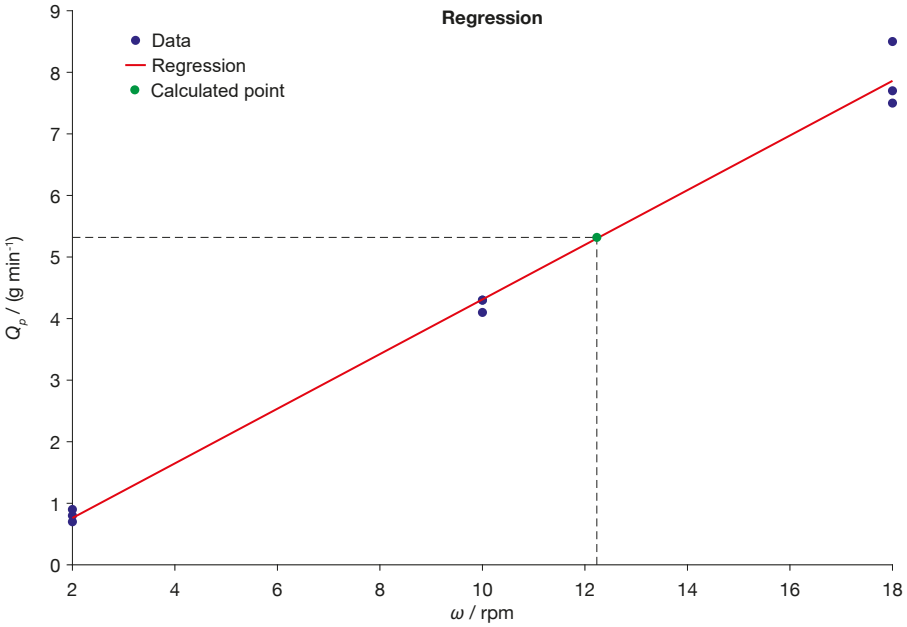

Fig. 5.15 Process parameters plot example

5.5 Conclusions

In the presented chapter, a detailed analysis was conducted on different mechanical and physical properties of samples, highlighting the various interactions between the parameters involved. Key findings are summarized below:

- **Height:** The analysis revealed a high correlation between the number of layers and the height of the sample. In particular, the increase in the ΔZ value, which indicates a lower number of layers, leads to a noticeable reduction in height. Other factors such as O_e, κ and E have significantly influenced pitch. The models developed for two levels of O_e highlighted the robustness and precision in analyzing the height of the samples;
- **Density:** The results showed an average density of (7.927 ± 0.006) g·cm^{-3} for the samples. Detailed analysis suggested a potential elimination of some inherent porosity in the material during the construction process. The homogeneous distribution of density data indicates the consistency and reproducibility of the manufacturing process within the chosen parameters;

- **Porosity:** The porosity distribution data was transformed to meet normality standards. However, the ANCOVA model proved insignificant post-transformation, and no correlations between density and porosity emerged. This underscores the need for future studies to employ more sophisticated tools to assess porosity accurately;

- **Hardness:** The results revealed that while microscopic hardness is affected by various factors, such as E, κ and O_e, the developed model explains only 30 % of the observed variance. This indicates that other factors or intrinsic variability could play a significant role in determining the hardness of samples. The interactions between the parameters, particularly between E and κ, showed a significant influence on hardness.

Chapter 6

Discussion and comparative evaluation of existing literature

6.1 Analysis and review of related literature

In any scientific exploration, a comprehensive understanding of existing studies, theories, and methodologies related to the topic is indispensable. This chapter critically reviews the existing literature, categorizing the findings based on the process parameters and the resulting outputs, defectiveness, and mechanical properties.

6.1.1 Analysis of key literature on process parameters and responses

The inherent adaptability of the DED-LB technology allows its configuration to be tailored to specific needs and requirements. Consequently, the process parameters can substantially differ from one configuration to another. Furthermore, the selection and emphasis on specific process parameters are driven mainly by the objectives that practitioners and researchers aim to achieve. For example, Qi and Mazumder [107] pinpointed the importance of 14 distinct process parameters in a quest to simulate the process numerically. This underlines the multifaceted nature of DED-LB, where different parameters can be prioritized based on the desired outcome and specific application demands.

On the other hand, Pinkerton [16], who delineated the three main physical processes that occur during DED-LB / powder-based construction, opted to isolate the key process parameters specifically for the powder-stream process. Among these, some are controllable and thus fall into the "manageable" category, such as laser power, gas flow rate, and powder mass flow rate. Other elements are intrinsic to the DED system employed, including the diameter and power distribution of the laser beam, the geometry of the nozzle and the stand-off distance. The latter, although adjustable, falls within the characteristics determined by the calibration procedure. Indeed, once the direction of the powder stream is calibrated, the point at which the powders collide becomes an intrinsic property of the system and is thus unmanageable. The remaining parameters are tied to the inherent "unmanageable" characteristics of the powder used.

Expanding on Pinkerton's categorization, the melt pool formation is predominantly influenced by laser power, though it can experience partial attenuation during its interaction with the powder stream. Influential parameters such as the powder flow rate and its velocity at the substrate, substrate temperature distribution, and travel speed are of paramount significance. Furthermore, the inherent chemical-physical characteristics of the substrate and the powder utilized determine the fabrication outcome. Additionally, attributes such as the dimensions of the substrate, thermo-mechanical properties, and surface quality undeniably impact the encompassing thermal phenomena within the DED-LB/Powder process.

In the DED-LB/Powder processes continuum, these stages culminate in the final step: solidification of the deposited track. The thermal history chiefly dictates the intricacies of this phase, the composition and morphology of the melt pool, the velocities of the solidification front, and the prevailing thermal gradient. Turning attention to the response categories delineated by Pinkerton, notable mentions include the residual stresses manifesting within the track and the substrate, the geometric attributes of the track, and lastly, the microstructure characteristics of the track, the remelting zone, and the HAZ.

The parameters mentioned above can be further detailed, and additional ones can also be identified, as pointed out by Svetlizky et al. [108]. Among the process parameters, we can also include the layer thickness, or layer Z-step (ΔZ), the hatching distance (comparable to O_e), and the deposition strategy (toolpath). Meanwhile, unmanageable parameters, unless there is a hermetically sealed building chamber,

include the amounts of oxygen and humidity within the chamber (BCs). With respect to the material itself, a finer level of detail can be achieved through analyses of the powder sample. Factors such as powder morphology, flowability, material reflectivity (given its interaction with a light source), and impurities such as undesired contents of oxygen, carbon, nitrogen, hydrogen, and moisture come into play. Moisture is often a cause of powder agglomeration, which leads to challenges in the powder stream process. To address this, it is prudent to dry and sieve the powders before every job or after the powder has been unused (or stored) for an extended period. Finally, when detailed system characteristics are presented, the source can be characterized by the type of laser, wavelength, pulse frequency, and duty cycle.

Single track

In the literature, significant efforts have been made regarding single tracks. Indeed, these are the initial outputs obtained through DED, following the solidification process (see Chapter 2). When the material is deepened, single tracks are linear scans that are used to characterize the geometric properties of the deposited material. Among these properties are the track height (H), width (W), and depth (D_{track}), as depicted in Figure 6.1. Despite the considerable endeavors in this domain, the approach adopted in this doctoral research diverges from this intermediate step. However, reporting some of the physically similar and comparable outcomes pertaining to single tracks is beneficial and essential.

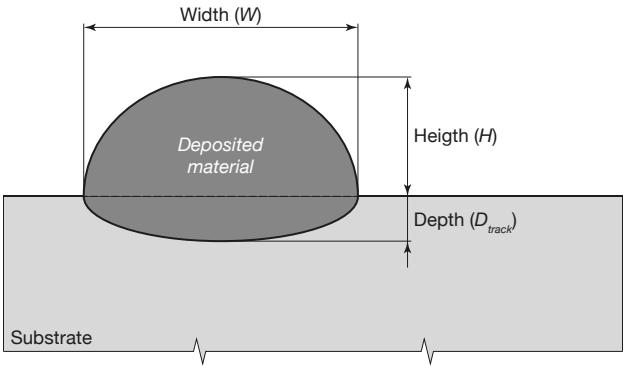

Fig. 6.1 Geometrical features of the msingle track; Depth (D_{track}), Width (W), Height (H). Image adapted from Piscopo et al. [109]

Kumar et al. [110] developed a mathematical model to predict the H of layers deposited using a specific technique. This model incorporated both the essential

material and build parameters that influence the H. Parameters not directly included in the model due to their complexity were validated using regression analysis, with titanium as the reference material. Though the validation was primarily for v the model applies to other significant build parameters, such as P and Q_p. The accuracy of this model in predicting the height of the deposited layer has an error margin close to 10 %

Sun et al. [111] explored the intricate relationship between process parameters and outcomes in laser cladding of Ti6Al4V using an Nd: YAG laser. Their findings indicate that while increased laser power expands layer width, a rise in scanning speed diminishes various metrics, except the W and H ratio. The powder feed rate displayed a contrasting influence on the depth and dimensions of the layer. The RSM emerged as an effective method to predict cladding geometry, with its developed model ensuring impressive accuracy of predictions within a 7 % error margin. This research underscores the potential of the model for enhancing precision and efficiency in laser cladding processes.

El Cheikh et al. [112] successfully applied multiple regression analysis to uncover the relationships between various process parameters and the cross-sectional properties of the clad, such as H and W. The high degree of correlation and residual analysis confirmed the efficacy of this statistical approach. The study reveals that H is mainly determined by energy intake per unit mass and the mass-to-length ratio of the powder. Although equations were developed to predict certain aspects of effective powder utilization, they needed to provide a comprehensive geometric understanding of the clad. The study concludes that the primary governing factor for clad geometry is surface tension on the molten pool rather than powder distribution in the jet.

Ocelík et al. [113] provide an in-depth study on side laser cladding, focusing on grey and compacted graphite cast iron substrates. Using combined parameters such as Q_p/v and P/v, the study finds that the process is robust across a range of laser power and powder feeding rates. A strong linear correlation is established between the feeding rate (Q_p) and H, supported by a high regression coefficient. The research also shows that side cladding achieves up to 90 % powder efficiency, higher than coaxial cladding. The study contributes to developing predictive models for optimizing laser cladding processes.

In the study conducted by Toyserkani et al. [114], the influence of E and powder F, defined as the Q_p divided by v times D, on the dimensions of the deposited track was examined. Notably, an increase in E resulted in elevations in both the H and width W of the deposited track. Conversely, a rise in F led to an increase in H but a decrease in W. In this context, F measures the powder density, influencing material deposition rates. These observations provide valuable guidance for optimizing process parameters in Directed Energy Deposition.

Building on the empirical relationships established by Toyserkani et al., Piscopo et al. [109] utilized this model to develop a thermal DED-LB/Powder model using the finite element method. This new model accounted for various physical characteristics of the process and demonstrated a reasonably accurate forecast for track geometry and temperatures, thus expanding the applicability of Toyserkani's findings.

In summary, extensive studies on single tracks have yielded predictive models to understand their geometric characteristics such as H, width W, and D_{track}. An increase in P generally leads to an expansion in W. On the contrary, a rise in scanning speed typically diminishes various geometric metrics, except for W/H. An increase in powder feeding rate also exhibits a contrasting influence on W and D_{track}. Importantly, these insights corroborate the initial hypotheses outlined in Chapter 2 of this research, thereby validating the adopted approach.

6.2 Linking between process parameters (predictors) and responses

In the progression from the literature review on single-track experiments to more comprehensive studies that correlate process parameters with responses such as layer thickness and microstructures, it becomes evident that DED-LB/Powder can be broadly categorized into two major types of machines. The first category consists of systems that incorporate a feedback loop for layer height control, adjusting parameters in real time to ensure optimal deposition. The second category lacks such a feedback mechanism, relying solely on pre-defined parameters without the capacity for real-time adjustments. This distinction is crucial, as it influences the geometric accuracy of the fabricated parts and their material properties, including micro-hardness and grain structure. Understanding the capabilities and limitations

of these two machine categories is instrumental in optimizing DED-LB/Powder processes.

The study by Shim et al. [35] delves into the intricacies of optimizing the slicing thickness in DED-LB/Powder manufacturing by adapting to actual deposited layer heights and various processing parameters. The authors carried out 31 sets of experiments, examining how changes in E and Q_p affect the height of the deposited layer. Their adaptive method yielded better geometric accuracy by automatically adjusting the slicing thickness based on the specific conditions, effectively minimizing errors due to under or over-deposition. While the feedback control method demonstrated superior geometric fidelity, it introduced variances in material properties, specifically micro-hardness, due to fluctuating energy input. Conversely, the conventional and adaptive methods maintained more uniform material properties but suffered from geometric inconsistencies, particularly under high-energy scenarios. Closed-loop control systems were suggested to overcome these limitations. The study illuminates the nuanced relationship between processing parameters and geometric and material outcomes in DED, providing a foundation for further advances in closed-loop control systems.

In the study by Webster et al. [37], a specialized energy density metric, GED, was introduced to explore its utility in parameter optimization for DED processes. These metrics serve as a compound variable that incorporates both laser power and powder mass flow rate, designed to predict melt pool dimensions. Although the investigation identifies a linear relationship between GED and the size of the melting pool for laser power and an exponential relationship for Q_p, the study claims that GED is not a consistent predictor of the dimensions of the melting pool or the height of the clad under varying process conditions. This observation challenges the validity of commonly used energy density metrics in DED and highlights the imperative for further empirical investigation.

One of the significant challenges in DED is the dynamic nature of the process parameters during deposition. Since metallic components under repair or construction typically have limited thermal diffusivity, they experience an increase in temperature until a steady state is reached. This increase in temperature poses a challenge to maintaining component quality and consistency. Consequently, adaptive tuning of process parameters during deposition, based on real-time temperature monitoring, has been identified as a critical approach for ensuring component integrity.

Consistent with this, Seltzer et al. [115] provided evidence that there is inherent variability in the geometry and temperature of the building during DED-based repair. They employed a camera system to monitor melt pool geometry and an optical profilometer for verification. Comparing these experimental results with numerical simulations, they demonstrated the feasibility of real-time parameter adjustments through feedback control systems to improve repair quality.

Similarly, Reutzel et al. [116] underscored the crucial role of sensing and control systems in the regulation of process variables such as the geometry of the melt pool, the temperature and the height of the build of the layer. They emphasized that these variables are directly related to the final quality of the components, affecting the dimensions, microstructure, and material properties. Both sets of research emphasize the need for real-time monitoring and parameter adaptation in DED. They highlight the intricate balance of variables that affect component quality and advocate for more research into advanced control mechanisms to further optimize the process.

Boisselier et al. [117] conducted an exhaustive study that is particularly relevant to the technique and material under consideration in this work. Focusing on AISI 316L stainless steel and using a coaxial laser cladding nozzle, they explored the critical role of powder characteristics in the DED process. Their findings revealed the necessity of thorough powder characterization—encompassing grain size, shape, and chemical composition—before applying DED. They used three different batches of AISI 316L powder and found that each batch produced different results in terms of deposition quality, requiring specific adjustments to process parameters. This research underscores the importance of tightly controlling powder characteristics, which is an unamangable parameter, to optimize flowability and laser-powder interaction and attain high-quality, defect-free components.

Aversa et al. [118] presented an in-depth investigation into the microstructure and composition of 316L stainless steel fabricated using DED-LB/Powder. Their work emphasized the formation of large columnar grains and complex microstructures containing γ-dendrites and δ-ferrite, which arise due to the unique thermal history of L-DED. They also focused on the occurrence of non-metallic particles rich in Si, Mn, and O, providing insights into their formation mechanisms during solidification. Their study further revealed the role of processing conditions, specifically building atmosphere, in influencing oxide formation and elemental pickup. Aversa et al. found that using a nitrogen-filled build chamber was more effective in limiting material

oxidation than only using a shielding gas. Their findings also demonstrated that the mechanical properties of the fabricated samples were influenced by the nitrogen atmosphere, leading to improved yield strength and elongation. Their meticulous examination of the microstructure and composition of DED-LB/Powder/AISI316L stainless steel makes their research particularly relevant for understanding the implications of processing conditions on material properties.

The next step of the previous work, always conducted by Aversa et al. [119], relates to optimizing process parameters for DED-LB/Powder/AISI316L stainless steel samples. They used nitrogen as the carrier and shielding gas, maintaining a flow rate of $3\,\mathrm{L{\cdot}min^{-1}}$. Single Scan Tracks (SSTs) were initially produced to refine parameter combinations. Subsequently, they were analyzed using optical microscopy and image analysis software. On the basis of these initial results, bulk samples were manufactured and examined for defects, geometrical characteristics, and mechanical properties using various techniques, including SEM and EBSD. The samples were also subjected to tensile tests and the results were evaluated using the Voce flow stress model. These comprehensive analyzes provided information on how different building parameters impact the mechanical properties, microstructure, and defect density of the samples.

6.3 Conclusions and implications for current research

In both academic and industrial landscapes, DED systems are inherently complex, continuously evolving in terms of reliability and sophistication year after year. Finding common ground among various studies is a highly challenging, if not nearly impossible, endeavor. However, specific fundamental physical processes are starting points for characterizing, developing, or improving a process. A unifying thread in the literature reviewed is a meticulous engineering-based methodological approach, which serves as a minimum common denominator among these studies.

This dissertation commences with the foundation laid by the literature review outlined in the preceding section, setting the stage for a methodological approach. Given the complexities of replicating precise results from other researchers, this work adopts an inherently experimental approach. Starting from basic hypotheses, the aim is to identify a window of process parameters and relationships that permit for consistent construction through the analyzed DED technique. Furthermore, the

findings of the cited publications have been leveraged to benchmark the test results, confirming that the research is progressing in the right direction. This methodology not only validates the reliability of the outcomes but also adds a layer of robustness, bridging the gap between academic research and industrial applicability.

In order to facilitate comparison of the results of this work with others in the field, rigorous adherence to established standards has been maintained, particularly concerning the Guide to the Expression of Uncertainty in Measurement (GUM). By diligently applying the GUM recommendations, it is anticipated that this research will not only stand on solid methodological ground but also serve as a reliable reference point for future studies, allowing meaningful comparisons and validations.

Chapter 7

Conclusions

In this work, rigorous mathematical modeling of the hypothesis followed by an extensive experimentation phase has comprehensively investigated the Laser Beam metal Powder Directed Energy Deposition (DED-LB/Powder) process. The study delves into three primary mechanisms: powder stream, melt pool, and track formation/solidification process.

Significant focus has been placed on characterizing the powder feeder system through a Design of Experiment (DoE) approach, which led to the determination of a response surface. Subsequently, a mathematical model was developed to quantify the amount of powder to flow in the powder streaming process to achieve the desired layer heights in the manufactured components.

Optimization of carrier gas levels was performed to ensure consistent growth (low process variability) of the specimens within the operating boundaries delineated by the response surface of the powder stream. A factor screening exercise was conducted to assess the validity of the proposed equation, considering parameters such as specific energy (E), powder surplus (κ), overlap efficiency (O_e), and layer height (ΔZ). This screening assessed the quality of the proposed equation and examined various output variables, such as specimen height relative to the target, density, porosity, and microhardness.

These meticulous evaluations generalize the findings, making them applicable and adaptable to various DED-LB/Powder systems. By fulfilling the initial research questions, this thesis provides a comprehensive understanding of the DED-LB process and paves the way for future research in this burgeoning field. The results of

this research endeavor are comprehensively synthesized and scrutinized, focusing on addressing the initial research questions:

RQ1: To what extent can a specimen be deposited to meet specified properties leveraging on process parameters utilizing a DED system?
In response to the first research question, the present study underscores the necessity for a rigorous mathematical framework. The latter should integrate key processes, including powder stream manipulation, track formation, and solidification. Notably, the overlay of tracks requires meticulous attention to ensure reliable material deposition, irrespective of variable process parameters such as applied energy. In the powder feeder system under examination, two principal variables—carrier gas flow rate (V_{cg}) and rotational speed of the perforated disk—merit particular attention. The observed response surface contradicts intuitive expectations; an increase in V_{cg} correlates with a reduced powder stream. Moreover, not all V_{cg} levels demonstrated efficacy in achieving proper material deposition. Suboptimal growth, defined as failure to attain the predetermined target height, was observed at V_{cg} levels below $5\,\mathrm{L{\cdot}min^{-1}}$. This phenomenon is potentially attributable to multiple factors, including but not limited to the morphological characteristics of the flow at the standoff point.

RQ2: How do deposition behaviors vary under diverse conditions when employing DED-LB, and which factors determine its robustness?
In addressing the second research question related to the variability in deposition behaviors under distinct conditions for DED-LB and the factors determining its robustness, the mathematical methodology formulated in response to the first research question was subjected to a factor screening analysis. Four key variables - E, κ, O_e, and ΔZ - were examined for their effects on deposition robustness. After the factor screening analysis, the following key findings were delineated to further elaborate on the methodology adopted:

- **Height** - Regression surfaces, one for each Oe strategy, optimized for the study displayed average values approximating 100 % of the targeted height. This outcome is of paramount significance as it provides initial geometric validation for the adopted methodology. By considering the influence of additional variables such as E, κ, and O_e, it becomes feasible to fine-tune the process parameters within the explored ranges to achieve the desired target height. Therefore, the first geometric requirement is satisfactorily met and is

intrinsically influenced by optimizing the powder stream process, particularly the carrier gas flow rate levels;

- **Density** - The factors investigated were found to be insignificant in differentiating core density variations among the samples. The latter indicates no substantial differences within and between groups and across the boundary conditions set for the ANCOVA. Moreover, the overall density of the sample size exceeded that of the powder, suggesting that some of the inherent porosity of the powder is lost during the deposition process. These results serve as invaluable insights regarding the methodology employed. Specifically, they imply that even when process parameters such as specific energy are varied (within the processability windows of the material), the specimens fabricated using this approach exhibit indistinguishable differences. This finding serves as a robust foundation for evaluating subsequent mechanical characteristics;

- **Porosity** – The analysis was assessed through optical microscopy of a specimen cross-section, leading to challenges such as data non-normality and the absence of a negative correlation with density. Given that only a small cluster of data exhibited behavior consistent with the underlying physics of the issue, porosity measurements obtained through this technique are not recommended for refined analyses. Instead, this approach should be employed for qualitative assessments, considering only a single cross-sectional plane of the specimen;

- **Hardness** - Given the limited coefficient of determination and predictive reliability of the model for the hardness, it is evident that the analysis may not yield precise outcomes for this specific response variable. However, several critical insights into microhardness were observed. Firstly, doubling the number of layers (O_e=50 %) while keeping specific energy and powder constant decreased the sample's microhardness. This finding aligns with thermal cycle theories and the consequent grain growth. Secondly, a variance in microhardness within the specimen was noted, depending on the height (along the Z-axis of construction). Specifically, the upper layers exhibited greater microhardness compared to the lower layers, which is attributable to the fewer thermal cycles the upper layers undergo relative to the layers constructed earlier.

The present study furnishes a nuanced understanding of the interdependencies between the various process parameters and their subsequent impact on the mechanical

and geometrical attributes of the samples. Importantly, the hypotheses postulated were validated; no discernible disparities were observed in the specimens from either geometrical or mechanical viewpoints, thereby affirming the methodological robustness of the study. These insights are vital for further refining AM procedures and producing high-quality end-products. The established relationships between process parameters and mechanical attributes also provide a basis for designing and manufacturing components with tailored properties.

7.1 Limitations and Future Research

The present study has sought to provide a comprehensive understanding of the relationships between various process parameters and the resulting material properties in additive manufacturing, specifically focusing on Direct Energy Deposition with Laser Beam and Powder (DED-LB/Powder) using AISI 316L. While the models developed offer promising avenues for optimizing geometric features and core properties, it is crucial to acknowledge the inherent limitations and scopes for future research. This contextualization not only affords the current findings their due weight but also charts a roadmap for subsequent scholarly investigations. The discussion elaborates on these limitations and suggests avenues for future research to bridge existing gaps.

Geometric Features and Core Properties: The models in this study are primarily designed to evaluate the geometric features and properties of the core bulk of samples. These models are particularly suited for parts produced through DED-LB/Powder and intended for subsequent machining processes. Surface finish is not incorporated into the current models, as any surface imperfections are assumed to be corrected through post-processing methods like machining. Porosity Assessment: No model is currently available for evaluating specific attributes of porosity, such as size or type (e.g., lack of fusion, gas entrapment, or keyhole formation). Future studies should consider using advanced measurement techniques like computed tomography scanning for a more comprehensive understanding of porosity.

Uniform Substrates of Similar Material: The research results are derived from samples deposited onto uniform substrates made of the same material, AISI 316L, as the samples. This could limit the immediate applicability to real-world components involving different or irregular substrate conditions.

Process Parameters and Material Specificity: The models are tailored for a specific range of specific energy and are based on the use of AISI 316L. However, the methodology itself can be generalized to various types of powders. Although individual calibration would be necessary, the investigation methods are universal and can be applied to any material system. Material Specificity: While the current model is developed for AISI 316L, the procedural framework is versatile and could be applied to any powder type. The investigative methods are universal, thus offering a foundational base for their application across diverse material systems. These limitations provide valuable context for the applicability of the current models and methodologies. The findings of this study open multiple avenues for future research to explore, refine, and expand upon the models and methodologies currently employed. Enhanced Predictive Models: The initial models have shown promise in mapping the relationships between process parameters and deposition quality. A natural progression would be to further explore the limits of process windows and assess deposition quality within these windows using the proposed methodology. In cases where systems exhibit optimizable responses—variations that lead to notable improvements—optimization techniques such as gradient-based methods in an experimental setting could be employed.

Advanced Porosity Assessment: Given the limitations of the optical microscopy-based approach for porosity evaluation, future studies could consider utilizing more advanced tools like CT scanners. This would enable a refined correlation analysis with the density data already obtained, possibly leading to more accurate predictive models for porosity. Mechanical Properties: Although density does not vary significantly with the changing input parameters, the same cannot be said for mechanical properties, which are affected by factors like energy input and thermal cycles. Particular attention should be paid to the junction area between the deposited material and the substrate to understand how these parameters influence mechanical characteristics.

Comparative Studies: As a further step, the research could be expanded to compare the findings of this study with results obtained using other Direct Energy Deposition methods, such as wire-based systems.

Material Versatility: While the current study focuses solely on AISI 316L, the methodologies are universal and can be adapted for any powder type, making the approach highly versatile. This roadmap sets the stage for a comprehensive

and multifaceted exploration of additive manufacturing technologies, pushing the boundaries of current knowledge and capabilities.

References

[1] KERN & SOHN GmbH. Analytical balance ABS-N_ABJ-NM_ACS_ACJ. Web Page, Accessed: 10-08-23.

[2] Anton Paar GmbH. Gas Pycnometer for Semi-Solid and Solid Density: Ultrapyc. Web Page, Accessed: 10-08-23.

[3] S. V. Buer, J. O. Strandhagen, and F. T. S. Chan. The link between industry 4.0 and lean manufacturing: Mapping current research and establishing a research agenda. *International Journal of Production Research*, 56(8):2924–2940, 2018.

[4] J. Bicheno and M. Holweg. *The lean toolbox*, volume 4. PICSIE books Buckingham, 2000.

[5] F. Almada-Lobo. The industry 4.0 revolution and the future of manufacturing execution systems (mes). *Journal of Innovation Management*, 3(4):16–21, 2015.

[6] M. Javaid, A. Haleem, R.P. Singh, R. Suman, and E. Santibañez Gonzalez. Understanding the adoption of Industry 4.0 technologies in improving environmental sustainability. *Sustainable Operations and Computers*, 3:203–217, 2022.

[7] S. Crump. Apparatus and method for creating three-dimensional objects, 6 1992. Patent No. 429,012.

[8] J. Gallego. A host of soon-to-be-expired patents are set to revolutionize 3d printing, 2016. Web Page, Accessed: 12-10-23.

[9] C. K. Chua, K. F. Leong, and C. S. Lim. *Rapid Prototyping: Principles and Applications*. World Scientific, 2010. Book.

[10] J. Patalas-Maliszewska and M. Topczak. A new management approach based on additive manufacturing technologies and industry 4.0 requirements. *Advances in Production Engineering & Management*, 16(1), 2021. Journal Article.

[11] M. Shahin, F. F. Chen, H. Bouzary, and K. Krishnaiyer. Integration of lean practices and industry 4.0 technologies: smart manufacturing for next-generation enterprises. *The International Journal of Advanced Manufacturing Technology*, 107:2927–2936, 2020.

[12] J. Franklin. Check out the first 3d-printed steel bridge recently unveiled in europe, 2021. Web Page, Accessed: 12-10-23.

[13] ISO/ASTM 52900:2021(E). Standard terminology for additive manufacturing – general principles – terminology, 2021. Standard.

[14] ASTM F3187-16. Standard guide for directed energy deposition of metals, 2016. Standard.

[15] Prima Additive S.r.l. Ianus cell, 2023. Web Page, Accessed: 15-10-23.

[16] Andrew J. Pinkerton. Advances in the modeling of laser direct metal deposition. *Journal of Laser Applications*, 27(S1):S15001, 2015.

[17] G. Piscopo, E. Atzeni, A. Saboori, and A. Salmi. An overview of the process mechanisms in the laser powder directed energy deposition. *Applied Sciences (Switzerland)*, 13(1), 2023.

[18] Ambrish Singh, Sajan Kapil, and Manas Das. A comprehensive review of the methods and mechanisms for powder feedstock handling in directed energy deposition. *Additive Manufacturing*, 35, 2020.

[19] S. Kapil, P. Kulkarni, P. Joshi, S. Negi, and K. P. Karunakaran. Retrofitment of a cnc machine for omni-directional tungsten inert gas cladding. *Virtual and Physical Prototyping*, 14(3):293–306, 2019.

[20] J. L. Arrizubieta, I. Tabernero, J. Exequiel Ruiz, A. Lamikiz, S. Martinez, and E. Ukar. Continuous coaxial nozzle design for lmd based on numerical simulation. In *Physics Procedia*, volume 56, pages 429–438, 2014.

[21] H. Tan, W. Shang, F. Zhang, A. T. Clare, X. Lin, J. Chen, and W. Huang. Process mechanisms based on powder flow spatial distribution in direct metal deposition. *Journal of Materials Processing Technology*, 254:361–372, 2021.

[22] E. S. Menon. *Piping calculations manual*. McGraw-Hill Education, 2005.

[23] P. Stavropoulos, H. Bikas, and T. Bekiaris. A powder delivery system for large-scale ded machines. In *Procedia CIRP*, volume 109, pages 617–622, 2022. Export Date: Feb. 20, 2023.

[24] G. Winkler. Analysing the vibrating conveyor. *International Journal of Mechanical Sciences*, 20(9):561–570, 1978.

[25] ISO/ASTM 52907-19. Additive manufacturing — feedstock materials — methods to characterize metallic powders, 2019.

[26] C. Bernauer, L. Meinzinger, A. Zapata, X. Fan Zhao, S. Baehr, and M. F. Zaeh. Design and investigation of a novel local shielding gas concept for laser metal deposition with coaxial wire feeding. *Applied Sciences*, 13(8), 2023.

[27] J. E. Ruiz, M. Cortina, J. I. Arrizubieta, and A. Lamikiz. Study of the influence of shielding gases on laser metal deposition of inconel 718 superalloy. *Materials*, 11(8):1388, 2018.

[28] K. Weman. *Welding processes handbook*. Elsevier, 2011.

[29] D. V. Sergachev, A. A. Mikhal'chenko, O. B. Kovalev, V. I. Kuz'min, G. N. Grachev, and P. A. Pinaev. Laser-optic measurements of velocity of particles in the powder stream at coaxial laser cladding. In *Physics Procedia*, volume 56, pages 193–203, 2014.

[30] N. Shamsaei, A. Yadollahi, L. Bian, and S. M. Thompson. An overview of direct laser deposition for additive manufacturing; part ii: Mechanical behavior, process parameter optimization and control. *Additive Manufacturing*, 8:12–35, 2015.

[31] A. Bejan and A. D. Kraus. *Heat transfer handbook*, volume 1. John Wiley & Sons Inc., 2003.

[32] L. K. Ang, Y. Y. Lau, and H. L. Gilgenbach, R. M. Spindler. Analysis of laser absorption on a rough metal surface. *Applied Physics Letters*, 70(6):696–698, 1997.

[33] S. Tornincasa. *Technical Drawing for Product Design*. Springer, 2021.

[34] Z. Gan, G. Yu, X. He, and S. Li. Numerical simulation of thermal behavior and multicomponent mass transfer in direct laser deposition of co-base alloy on steel. *International Journal of Heat and Mass Transfer*, 104:28–38, 2017.

[35] D.-S. Shim, G.-Y. Baek, J.-S. Seo, G.-Y. Shin, K.-P. Kim, and K.-Y. Lee. Effect of layer thickness setting on deposition characteristics in direct energy deposition (ded) process. *Optics & Laser Technology*, 86:69–78, 2016.

[36] I. Gibson, D. Rosen, and B. Stucker. *Additive manufacturing technologies: 3D printing, rapid prototyping, and direct digital manufacturing*. Springer, New York, 2nd edition, 2015.

[37] S. Webster, K. Ehmann, and J. Cao. Energy density comparison via highspeed, in-situ imaging of directed energy deposition. In *48th SME North American Manufacturing Research Conference, NAMRC 48*, volume 48, pages 691–696, 2020.

[38] M. Liu, A. Kumar, S. Bukkapatnam, and M. Kuttolamadom. A review of the anomalies in directed energy deposition (ded) processes & potential solutions - part quality & defects. In *49th SME North American Manufacturing Research Conference (NAMRC 49, 2021)*, volume 53, pages 507–518, 2021.

[39] J. O. Milewski. *Additive Manufacturing of Metals*. Springer Series in Materials Science. Springer, 2017.

[40] K. D. Traxel and A. Bandyopadhyay. Reactive-deposition-based additive manufacturing of ti-zr-bn composites. *Additive Manufacturing*, 24:353–363, 2018.

[41] Panagiotis Stavropoulos and Panagis Foteinopoulos. Modelling of additive manufacturing processes: a review and classification. *Manufacturing Review*, 5:2, 2018.

[42] V. C. Panagiotopoulou, A. Paraskevopoulou, and P. Stavropoulos. A framework to compute carbon emissions generated from additive manufacturing processes. In *Lecture Notes in Mechanical Engineering*, pages 311–319, 2023.

[43] J. Han, G. Zhang, X. Chen, Y. Cai, Z. Luo, X. Zhang, Y. Su, and Y. Tian. High strength ti alloy fabricated by directed energy deposition with in-situ cu alloying. *Journal of Materials Processing Technology*, 310, 2022.

[44] A. Dass and A. Moridi. State of the art in directed energy deposition: From additive manufacturing to materials design. *Coatings*, 9(7):418, 2019.

[45] H. Wang, Y. Hu, F. Ning, and W. Cong. Ultrasonic vibration-assisted laser engineered net shaping of inconel 718 parts: Effects of ultrasonic frequency on microstructural and mechanical properties. *Journal of Materials Processing Technology*, 276, 2020.

[46] B. Vamsi Krishna, Susmita Bose, and Amit Bandyopadhyay. Low stiffness porous ti structures for load-bearing implants. *Acta Biomaterialia*, 3(6):997–1006, 2007.

[47] P. Stavropoulos, H. Bikas, O. Avram, A. Valente, and G. Chryssolouris. Hybrid subtractive–additive manufacturing processes for high value-added metal components. *The International Journal of Advanced Manufacturing Technology*, 111:645–655, 2020.

[48] R. Steinhilper. *Remanufacturing - The Ultimate Form of Recycling*. Fraunhofer IRB Verlag, 1998.

[49] Prima Additive S.r.l. Ianus cell, 2023. Web Page, Accessed: 23-08-23.

[50] ASTM E8-E8M. Standard test methods for tension testing of metallic materials, 2021.

[51] ASTM A370-20. Standard test methods and definitions for mechanical testing of steel products, 2020.

[52] ASTM E384-22. *Standard Test Method for Microindentation Hardness of Materials*. ASTM International, 2022.

[53] J. Wang, S. Prakash, Y. Joshi, and F. W. Liou. Laser aided part repair–a review. In *Proceedings of the 13th Annual Solid Freeform Fabrication Symposium*, 2002.

[54] G. Maculotti, J. Kholkhujaev, G. Genta, and M. Galetto. Direct calibration of indenter tip geometry by optical surface topography measuring instruments. *Journal of Materials Research*, 38(13):3336 – 3348, 2023.

[55] S. D. Sun, Q. Liu, M. Brandt, M. Janardhana, and G. Clark. Microstructure and mechanical properties of laser cladding repair of aisi 4340 steel. In *28th Congress of the International Council of the Aeronautical Sciences 2012, ICAS 2012*, volume 6, pages 5127–5135, 2012.

[56] H. Paydas, A. Mertens, R. Carrus, J. Lecomte-Beckers, and J. T. Tchuindjang. Laser cladding as repair technology for ti–6al–4v alloy: Influence of building strategy on microstructure and hardness. *Materials & Design*, 85:497–510, 2015.

[57] A. Saboori, A. Aversa, G. Marchese, S. Biamino, M. Lombardi, and P. Fino. Application of directed energy deposition-based additive manufacturing in repair. *Applied Sciences-Basel*, 9(16):3316, 2019.

[58] V. K. Balla, S. Banerjee, S. Bose, and A. Bandyopadhyay. Direct laser processing of a tantalum coating on titanium for bone replacement structures. *Acta Biomaterialia*, 6(6):2329–2334, 2010.

[59] T. Hauser, P. P. Breese, T. Kamps, C. Heinze, J. Volpp, and A. F. H. Kaplan. Material transitions within multi-material laser deposited intermetallic iron aluminides. *Additive Manufacturing*, 34, 2020.

[60] G. P. Dinda, L. Song, and J. Mazumder. Fabrication of ti-6al-4v scaffolds by direct metal deposition. *Metallurgical and Materials Transactions A*, 39:2914–2922, 2008.

[61] K. I. Makarenko and I. V. Shishkovsky. Direct energy deposition of cu-fe system functionally graded structures. In *IOP Conference Series: Materials Science and Engineering*, volume 969, 2023. Export Date: 02 October 2023; Cited By: 4.

[62] S. M. Banait, C. P. Paul, A. N. Jinoop, H. Kumar, R. S. Pawade, and K. S. Bindra. Experimental investigation on laser directed energy deposition of functionally graded layers of ni-cr-b-si and ss316l. *Optics & Laser Technology*, 121:105787, 2020.

[63] FAO. Wheat: Crop description and climate, 2023. Web Page, Accessed: 17-07-23.

[64] F. Yates. Sir ronald fisher and the design of experiments. *Biometrics*, 20(2):307–321, 1964.

[65] A. Sacco, A. Onofri, and D. Experimental methods in agriculture, 2022. Web Page, Accessed: 17-07-23.

[66] Pedro Domingos. The role of occam's razor in knowledge discovery. *Data Mining and Knowledge Discovery*, 3(4):409–425, 1999.

[67] George E.P. Box, William H. Hunter, and Stuart Hunter. *Statistics for Experimenters*, volume 664. John Wiley & Sons Inc., New York, 1978.

[68] JCGM. Guide to the expression of uncertainty in measurement, 2008. Web Page, Accessed: 19-07-23.

[69] D. C. Montgomery and G. C. Runger. *Applied Statistics and Probability for Engineers*. Wiley Series in Probability and Statistics. John Wiley & Sons Inc., 7th edition, 2023.

[70] F. Yates. The design and analysis of factorial experiments. 1937.

[71] D. C. Montgomery. *Design and Analysis of Experiments, 9th Edition*. John Wiley & Sons, 2022.

[72] Dharmaraja Selvamuthu and Dipayan Das. *Introduction to Statistical Methods, Design of Experiments and Statistical Quality Control*. Springer, 2018.

[73] Minitab LLC. Residual plots for analyze factorial design, 2023. Web Page, Accessed: 08-08-23.

[74] A. Messac. *Optimization in practice with MATLAB®: for engineering students and professionals*. Cambridge University Press, 2015.

[75] Minitab LLC. Screening designs, 2023. Web Page, Accessed: 06-08-23.

[76] X. Li, N. Sudarsanam, and D. D. Frey. Regularities in data from factorial experiments. *Complexity*, 11(5):32–45, 2006.

[77] C. Daniel. Use of half-normal plots in interpreting factorial two-level experiments. *Technometrics*, 1(4):311–341, 1959.

[78] Paul Mathews. *Sample size calculations: Practical methods for engineers and scientists*. Mathews Malnar and Bailey Inc., 2010.

[79] M. Kaya Bahçecitapar, Ö. Karadağ, and S. Aktaş. Estimation of sample size and power for general full factorial designs. *istatistikçiler Dergisi: istatistik ve Aktüerya*, 9(2):79–86, 2016.

[80] G. E. P. Box and K. B. Wilson. *On the Experimental Attainment of Optimum Conditions*, pages 270–310. Springer New York, 1992.

[81] N. R. Draper and H. Smith. *Applied regression analysis*, volume 326. John Wiley & Sons, 1998.

[82] R. H Myers, D. C. Montgomery, and C. M. Anderson-Cook. *Response surface methodology: process and product optimization using designed experiments*. John Wiley & Sons, 2016.

[83] ISO 80000-3:2020. Quantities and units. Space and time, 2020.

[84] BIMP. The international system of units (SI), 2019.

[85] Y. Cengel and J. Cimbala. *Fluid Mechanics Fundamentals and Applications: Third Edition*. McGraw-Hill Education, 2013.

[86] ISO 3953:2011. Metallic powders – Determination of tap density, 2011.

[87] ISO 4490:2018. Metallic powders – etermination of flow rate by means of a calibrated funnel (Hall flowmeter), 2011.

[88] Y. A. Cengel and A. Ghajar. *Heat and Mass Transfer: A Practical Approach, SI Version*. McGraw-Hill Education, New York, NY, USA, 2011.

[89] Richard P. Feynman, Robert B. Leighton, and Matthew Sands. *The Feynman Lectures on Physics; Vol. I.* Addison-Wesley, 1965.

[90] N. de Nevers. *Physical and Chemical Equilibrium for Chemical Engineers: Second Edition*. Wiley, 2012.

[91] C. A. Ellis and S. A. Parbery. Is smarter better? a comparison of adaptive, and simple moving average trading strategies. *Research in International Business and Finance*, 19(3):399–411, 2005.

[92] F. R. Johnston, J. E. Boyland, M. Meadows, and E. Shale. Some properties of a simple moving average when applied to forecasting a time series. *Journal of the Operational Research Society*, 50(12):1267–1271, 1999.

[93] J. Cohen. *Statistical Power Analysis for the Behavioral Sciences*. Routledge, 2013.

[94] F. Faul, E. Erdfelder, A.-G. Lang, and A. Buchner. G* power 3: A flexible statistical power analysis program for the social, behavioral, and biomedical sciences. *Behavior Research Methods*, 39(2):175–191, 2007.

[95] J. Von Neumann. Various techniques used in connection with random digits. *Appl. Math Ser*, 12(36-38):3, 1951.

[96] Minitab LLC. Interpret all statistics and graphs for display descriptive statistics, 2023. Web Page, Accessed: 09-05-2023.

[97] I. Garmendia, J. Pujana, A. Lamikiz, M. Madarieta, and J. Leunda. Structured light-based height control for laser metal deposition. *Journal of Manufacturing Processes*, 42:20–27, 2019.

[98] W.-S. Woo, E.-J. Kim, H.-I. Jeong, and C.-M. Lee. Laser-assisted machining of ti-6al-4v fabricated by ded additive manufacturing. *International Journal of Precision Engineering and Manufacturing-Green Technology*, 7, 2020.

[99] L. D. Landau, A. I. Akhiezer, and E. M. Lifshitz. *General Physics: Mechanics and Molecular Physics*. Pergamon Press, 2013.

[100] W. J. Stronge. *Impact Mechanics*. Cambridge University Press, 2018.

[101] A. Bejan. *Convection Heat Transfer*. John Wiley & Sons Inc., 2013.

[102] ISO 6507-1:2023. Metallic materials — vickers hardness test — part 1: Test method, 2023.

[103] ASTM E384-22. Standard test method for microindentation hardness of materials, 2022.

[104] Y. M. Chou, A. M. Polansky, and R. L. Mason. Transforming non-normal data to normality in statistical process control. *Journal of Quality Technology*, 30(2):133–141, 1998.

[105] Y. Li, A. J. Bushby, and D. J. Dunstan. The hall–petch effect as a manifestation of the general size effect. *Proceedings of the Royal Society A: Mathematical, Physical and Engineering Sciences*, 472(2190):20150890, 2016.

[106] S. K. Moheimani, L. Iuliano, and A. Saboori. The role of substrate pre-heating on the microstructure, roughness, and mechanical performance of aisi 316l produced by directed energy deposition additive manufacturing. *The International Journal of Advanced Manufacturing Technology*, 119(11-12):7159–7174, 2022.

[107] H. Qi, J. Mazumder, and H. Ki. Numerical simulation of heat transfer and fluid flow in coaxial laser cladding process for direct metal deposition. *Journal of Applied Physics*, 100(2):024903, 07 2006.

[108] D. Svetlizky, M. Das, B. Zheng, A. L. Vyatskikh, S. Bose, A. Bandyopadhyay, J. M. Schoenung, E. J. Lavernia, and N. Eliaz. Directed energy deposition (ded) additive manufacturing: Physical characteristics, defects, challenges and applications. *Materials Today*, 49:271–295, 2021.

[109] G. Piscopo, E. Atzeni, and A. Salmi. A hybrid modeling of the physics-driven evolution of material addition and track generation in laser powder directed energy deposition. *Materials*, 12(7), 2019.

[110] S. Kumar, V. Sharma, A. K. S. Choudhary, S. Chattopadhyaya, and S. Hloch. Determination of layer thickness in direct metal deposition using dimensional analysis. *International Journal of Advanced Manufacturing Technology*, 67(9-12):2681–2687, 2013.

[111] Y. Sun and M. Hao. Statistical analysis and optimization of process parameters in ti6al4v laser cladding using nd:yag laser. *Optics and Lasers in Engineering*, 50(7):985–995, 2012.

[112] H. El Cheikh, B. Courant, S. Branchu, J.-Y. Hascoët, and R. Guillén. Analysis and prediction of single laser tracks geometrical characteristics in coaxial laser cladding process. *Optics and Lasers in Engineering*, 50(3):413–422, 2012.

[113] V. Ocelík, U. de Oliveira, M. de Boer, and J. Th. M. de Hosson. Thick co-based coating on cast iron by side laser cladding: Analysis of processing conditions and coating properties. *Surface and Coatings Technology*, 201(12):5875–5883, 2007.

[114] E. Toyserkani, A. Khajepour, and S. F. Corbin. *Laser Cladding*. CRC Press, 2004.

[115] D. M. Seltzer, X. Wang, A. R. Nassar, J. L. Schiano, and E. W. Reutzel. System identification and feedback control for directed-energy, metal-based additive manufacturing. In *Proceedings - 26th Annual International Solid Freeform Fabrication Symposium - An Additive Manufacturing Conference, SFF 2015*, pages 592–601, 2020.

[116] E. W. Reutzel and A. R. Nassar. A survey of sensing and control systems for machine and process monitoring of directed-energy, metal-based additive manufacturing. *Rapid Prototyping Journal*, 21(2):159–167, 2015.

[117] D. Boisselier and S. Sankaré. Influence of powder characteristics in laser direct metal deposition of ss316l for metallic parts manufacturing. volume 39, pages 455–463, 2012.

[118] A. Aversa, A. Saboori, E. Librera, M. de Chirico, S. Biamino, M. Lombardi, and P. Fino. The role of directed energy deposition atmosphere mode on the microstructure and mechanical properties of 316l samples. *Additive Manufacturing*, 34, 2020.

[119] A. Aversa, G. Marchese, and E. Bassini. Directed energy deposition of aisi 316l stainless steel powder: Effect of process parameters. *Metals*, 11(6), 2021.

[120] Minitab LLC. Types of t-tests, 2023. Web Page, Accessed: 14-08-23.

[121] G. E. P. Box and D. R. Cox. *An Analysis of Transformations Revisited, Rebutted*. University of Wisconsin-Madison, Mathematics Research Center, 1981.

[122] A. Agresti and M. Kateri. *Foundations of Statistics for Data Scientists: With R and Python*. CRC Press, 2021.

[123] JCGM 100:2008 BIPM. Evaluation of measurement data — guide to the expression of uncertainty in measurement, 2008. Web Page, Accessed: 10-08-23.

Appendix A

Parametric Statistical Tests

A.1 *t*-test in hypothesis testing

In statistical analysis, the t-test is employed to ascertain whether the mean of a specific population significantly deviates from a hypothesized value. This methodology is particularly advantageous when the population variance is unknown, distinguishing it from the Z-test, necessitating knowledge of this variance. Instead, the t-test utilizes sample variance as an estimate. The t-test can be classified as follows [120]:

- **One-Sample *t*-test:** evaluates if the mean of a single population is statistically equivalent to a predefined value;
- **Two-Sample *t*-test:** determines whether there is a statistically significant difference between the means of two independent populations;
- **Paired *t*-test:** assesses if the mean difference between paired observations is statistically equivalent to a hypothesized value;
- ***t*-test in regression:** In advanced statistical contexts, this variation of the t-test evaluates whether specific coefficients in a regression equation differ significantly from zero.

For the effective application of the t-test, certain assumptions must be met. Both populations under comparison must exhibit independence and be approximately normally distributed. Furthermore, these populations should display homogeneity of

variances. The veracity of these assumptions can be assessed using NPP. Despite its sensitivity to deviations from normality, the robustness of the t-test is noteworthy, particularly with larger sample sizes. However, alternative statistical tests might be more appropriate in cases of smaller sample sizes accompanied by significant deviations from normality. In certain contexts, the t-test quantifies the magnitude of deviation of an estimated value from an expected value relative to variability. Some literature posits that, given random sampling, the t-test might retain its validity even without strict adherence to the normality assumption. Such versatility has entrenched the t-test as a fundamental tool in diverse research domains.

A.2 ANOVA

This paragraph introduces the core principles of ANOVA, preparing the groundwork for subsequent chapters. The objective is to equip readers with a foundational grasp of this statistical method, paving the way for in-depth analyses and results.

The elegance of ANOVA lies in its ability to provide a unified framework for multiple comparisons without inflating the Type I error rate. Where multiple t-tests would compound the risk of false positives, ANOVA controls for this risk, ensuring that the overall error rate remains consistent. This statistical rigor is combined with efficiency, as ANOVA's comprehensive approach avoids the complexity and potential inconsistencies that might arise from performing and interpreting multiple individual tests. In addition to its primary function of testing the equality of means, ANOVA can be extended and adapted to various complex designs, such as repeated measures and factorial ANOVA, making it a versatile tool in the statistical toolkit.

ANOVA validity lies in the following assumptions:

- Observations within and between groups must be independent;
- Populations from which samples are drawn must be normally distributed;
- Homoscedasticity of the variances within each group.

When these assumptions, especially the normal distribution of responses, are not met, it becomes essential to adopt corrective measures. One fundamental approach

to address this issue is through data transformation. The importance of data transformation is accentuated as it addresses challenges related to non-normal distributions. By leveraging appropriate transformations, variance can be stabilized, ensuring the robustness of subsequent ANOVA analyses. This work will exploit the Box-Cox transformation, a pivotal technique for managing non-normally distributed data [121].

Suppose we have k groups, or treatments (factor levels), with n_i observation for each group. There are an overall of N observations, and the sample mean of the i^{th} group is:

$$\bar{y}_i = \frac{1}{n_i} \sum_{j=1}^{n_i} y_{ij} \tag{A.1}$$

and the overall sample mean is:

$$\bar{\bar{y}} = \frac{1}{N} \sum_{i=1}^{k} \sum_{j=1}^{n_i} y_{ij} \tag{A.2}$$

ANOVA facilitates the simultaneous analysis of three or more means by partitioning the total variance in a dataset into two distinct components: between-group variance and within-group variance, which is equal to, say:

$$y_{ij} = \bar{\bar{y}} + (\bar{y}_i - \bar{\bar{y}}) + (y_{ij} - \bar{y}_i) \tag{A.3}$$

where the first term in brackets is the difference between groups, while the second term is the difference within groups, the effect model is a more straightforward way to express the latter relationship equation:

$$y_{ij} = \bar{\bar{y}} + \tau_i + \varepsilon_{ij} \tag{A.4}$$

where τ_i is the deviation from the overall sample means when a treatment is applied, and ε_{ij} is the random error component. The equation can be manipulated to obtain:

$$y_{ij} - \bar{\bar{y}} = \tau_i + \varepsilon_{ij} \tag{A.5}$$

Since we are interested in evaluating if the treatment has an effect on the response, the null and the alternative hypotheses become:

$$H_0 : \tau_1 = \tau_2 = \cdots = \tau_i = 0$$
$$H_A : \tau_i \neq 0 \quad \text{for at least one treatment level}$$

The decomposition of the sum of squares (SS) can be obtained:

$$\mathrm{SS}_{\mathrm{Total}} = \mathrm{SS}_{\mathrm{Treatment}} + \mathrm{SS}_{\mathrm{Error}} \tag{A.6}$$

where the $\mathrm{SS}_{\mathrm{Total}}$, $\mathrm{SS}_{\mathrm{Treatment}}$, and $\mathrm{SS}_{\mathrm{Error}}$ are, respectively, the total, the treatment, and the error sum of squares and are computed as:

$$\begin{aligned} \mathrm{SS}_{\mathrm{Total}} &= \sum_i \sum_j (y_{ij} - \bar{\bar{y}})^2 \\ \mathrm{SS}_{\mathrm{Treatment}} &= \sum_i \sum_j (\bar{y}_i - \bar{\bar{y}})^2 \\ \mathrm{SS}_{\mathrm{Error}} &= \sum_i \sum_j (\bar{y}_{ij} - \bar{y}_i)^2 \end{aligned} \tag{A.7}$$

The mean square (MS) determines the division of each SS by its degrees of freedom:

$$\begin{aligned} \mathrm{MS}_{\mathrm{Treatment}} &= \frac{\mathrm{SS}_{\mathrm{Treatment}}}{k-1} \\ \mathrm{MS}_{\mathrm{Error}} &= \frac{\mathrm{SS}_{\mathrm{Error}}}{N-k} \end{aligned} \tag{A.8}$$

where the treatment mean square ($\mathrm{MS}_{\mathrm{Treatment}}$) measures the variability of the sample means between each treatment, and mean squared error ($\mathrm{MS}_{\mathrm{Error}}$) measure the variability within the groups [69]. Finally the F-test is performed:

$$F = \frac{\mathrm{MS}_{\mathrm{Treatment}}}{\mathrm{MS}_{\mathrm{Error}}} \tag{A.9}$$

By comparing with a F-distribution with $k-1$ and $N-k$ degrees of freedom, and the null hypothesis could be rejected if F is larger than the F critic value (right of the 5% tail for 95% SL) [122]. These findings can be summarized in Table A.1.

Table A.1 ANOVA Table

Source	df	SS	MS	F
Treatment	$k-1$	$\mathrm{SS}_{\mathrm{Treatment}}$	$\mathrm{MS}_{\mathrm{Treatment}}$	$\frac{\mathrm{MS}_{\mathrm{Treatment}}}{\mathrm{MS}_{\mathrm{Error}}}$
Error	$N-k$	$\mathrm{SS}_{\mathrm{Error}}$	$\mathrm{MS}_{\mathrm{Error}}$	
Total	$N-1$	$\mathrm{SS}_{\mathrm{Total}}$		

A.2.1 ANCOVA

Analysis of Covariance (ANCOVA) is a sophisticated statistical technique that enhances the precision of experimental outcomes by adjusting for potential confounders. It elegantly melds principles intrinsic to both analysis of variance and regression analysis.

In empirical studies, it is common to encounter scenarios where a primary response variable exhibits a linear association with another variable. ANCOVA combines features from both analysis of variance and regression, making it a unique and powerful tool for researchers. This method is similar to blocking in experimental design. When researchers can directly control or block certain variables to reduce their influence, they do so. But blocking these variables, e.g. boundary conditions, is sometimes impossible. That's when ANCOVA comes in handy, allowing researchers to measure and adjust for these uncontrollable variables, known as covariates.

The ANCOVA model for a single-factor experiment with one covariate is articulated as:

$$y_{ij} = \bar{\bar{y}} + \tau_i + \gamma(x_{ij} - \bar{\bar{x}}) + \varepsilon_{ij} \tag{A.10}$$

within this model, y_{ij} is the response observation corresponding to a specific treatment, x_{ij} is the covariate measurement related to the y_{ij}, $\bar{\bar{y}}$ is the overall mean, τ_i is the effect associated with a specific treatment, γ is the regression coefficient, and ε_{ij} is the random error component. Furthermore, compared to the Taguchi method, which treats disturbance variables as being on just two discrete levels (low and high), ANCOVA offers a more robust approach. It views disturbance variables as continuous, capturing a wider range of potential influences. This makes the results more precise and provides a clearer picture of the underlying processes. In short, ANCOVA provides a reliable alternative for research situations where blocking is nott feasible, ensuring accuracy and clarity in findings [71].

Appendix B

Uncertainty estimation

B.1 Powder sample estimation

This appendix provides an in-depth analysis of uncertainty estimation for a sample of AISI 316L powder. In the domain of measurement, inherent uncertainties invariably manifest. This research diligently seeks to quantify such uncertainties, conforming to the criteria stipulated by the Guide to the Expression of Uncertainty in Measurement (GUM) [123].

For the mass measurement, a singular reading was obtained. Owing to the absence of multiple measurements, statistical analysis to ascertain variability was not feasible. Consequently, based on established norms and references, the uncertainty was classified as Type B. In contrast, the procedure for volume measurement was divergent. Multiple observations were procured utilizing a pycnometer, which permitted the categorization of the uncertainty as Type A, derived from the observed dispersion of results. The endeavor then transitioned to the computation of the combined uncertainty, integrating uncertainties from mass and volume measurements.

In this process, there was a consideration to employ the Welch-Satterthwaite formula. However, given the inherent nature of the Type B uncertainty associated with the mass measurement, its degrees of freedom are theoretically infinite. Consequently, this research utilized the degrees of freedom associated with the volume measurement to ensure a conservative stance in the combined uncertainty estimation. By adopting this method, the integrity of the Type B uncertainty remains unaltered. After this, the task was to derive a coverage factor, reflecting the confidence en-

veloping these measurements. A 95 % confidence level was employed, and specific methodologies were adopted to ascertain this factor.

The computational framework supporting this research was a bespoke MATLAB code. Such software facilitated intricate data analysis and fortified the reliability and precision of the uncertainty determinations. It merits noting that ancillary factors, including but not limited to temperature and pressure, were meticulously accounted for in the analysis, underscoring the rigor of the adopted methodology.

Appendix C

BCs system

C.1 Boundary condition system Sender

```
// Boundary condition system Sender
#include <Wire.h>
#include <Adafruit_BME280.h>
#include "max6675.h"
#include <SPI.h>
#define RXp2 16
#define TXp2 17
#include <Wire.h>
#include <Adafruit_BME280.h>
#include "max6675.h"
#include <SPI.h>
#define RXp2 16
#define TXp2 17

int thermoDO = 19;
int thermoCS = 23;
int thermoCLK = 5;

MAX6675 thermocouple(thermoCLK, thermoCS, thermoDO);
Adafruit_BME280 bme;

int x;
```

```
int k = 0;
int counter = 1;
int counter_TC = 1;
int var = 0;
float T;
float P;
float H;
double TC;
float T_avg = 0;
float P_avg = 0;
float H_avg = 0;
float TC_avg = 0;

void setup() {
  pinMode(26, INPUT);
  Wire.begin();
  Serial.begin(115200);
  Serial2.begin(9600, SERIAL_8N1, RXp2, TXp2);
  bme.begin(0x76);
}
void loop() {
  x = digitalRead(26);
  if (x == 1)
{
    T = bme.readTemperature();
    P = bme.readPressure();
    H = bme.readHumidity();
    TC = thermocouple.readCelsius();
    //Serial.println(TC);
    if (counter_TC == 1)
    {
      TC_avg = TC;
    }
    if (counter_TC != 1)
    {
      TC_avg = (TC_avg + TC) / 2;
    }
    counter_TC = counter_TC + 1;
```

```
61
62      if (counter == 1)
63      {
64        T_avg = T;
65        P_avg = P;
66        H_avg = H;
67      }
68      else
69      {
70        T_avg = (T_avg + T) / 2;
71        P_avg = (P_avg + P) / 2;
72        H_avg = (H_avg + H) / 2;
73      }
74      counter = counter + 1;
75      counter_TC = counter_TC + 1;
76      var = var +1;
77      k = 1;
78      if (var == 10)
79      {
80        //Serial.print("Thermocouple Temperature: ");
81        Serial.println(TC_avg,1);
82        var = 0;
83        counter_TC = 1;
84      }
85    }
86    if (x == 0 && k == 1)
87    {
88      Serial2.print("Average Temperature:");
89      Serial2.print(T_avg);
90      Serial2.print(" C  ");
91      Serial2.print("Average Pressure:");
92      Serial2.print(P_avg);
93      Serial2.print(" Pa  ");
94      Serial2.print("Average Humidity:");
95      Serial2.println(H_avg);
96      Serial2.print(" %  ");
97      k = 0;
98    }
```

```
  delay(1000);
}
```

C.2 Boundary condition system Reciver

```
// Boundary condition system Receiver
#include <Wire.h>
#include <WiFi.h>
#define RXp2 16
#define TXp2 17

const int output26 = 26;

WiFiServer server(80);
String header;
String testo;
int flag = 0;

const char* ssid     = "ESP32-Access-Point";
const char* password = "123456789";



void setup() {
  Serial.begin(115200);

  Serial2.begin(9600, SERIAL_8N1, RXp2, TXp2);

  pinMode(output26, OUTPUT);
  digitalWrite(output26, LOW);

  WiFi.softAP(ssid, password);
  IPAddress IP = WiFi.softAPIP();
  Serial.print("AP IP address: ");
  Serial.println(IP);
  server.begin();
```

```
32
33
34 }
35 void loop() {
36     Serial.println("TEST");
37     WiFiClient client = server.available();
38 if (client) {   // If a new client connects,
39     Serial.println("New Client.");  // print a message
        out in the serial port
40     String currentLine = "";    // make a String to hold
        incoming data from the client
41     while (client.connected()) {    // loop while the
        client's connected
42       if (client.available()) { // if there's bytes to
          read from the client,
43         char c = client.read(); // read a byte, then
44         Serial.write(c);    // print it out the serial
            monitor
45         header += c;
46         if (c == '\n') {    // if the byte is a newline
            character
47           if (currentLine.length() == 0) {
48             client.println("HTTP/1.1 200 OK");
49             client.println("Content-type:text/html");
50             client.println("Connection: close");
51             client.println();
52
53            if (header.indexOf("GET /START") >= 0) {
54               Serial.println("START");
55               flag = 1;
56               digitalWrite(output26, HIGH);
57             }
58             else if (header.indexOf("GET /STOP") >= 0) {
59               Serial.println("STOP");
60               flag = 0;
61               digitalWrite(output26, LOW);
62               testo = Serial2.readString();
63             }
```

```
64
65              // Display the HTML web page
66              client.println("<!DOCTYPE html><html>");
67              client.println("<head><meta name=\"viewport\"
                   content=\"width=device-width,
                   initial-scale=1\">");
68              client.println("<link rel=\"icon\"
                   href=\"data:,\">");
69              // CSS to style the on/off buttons
70              // Feel free to change the background-color
                   and font-size attributes to fit your
                   preferences
71              client.println("<style>html { font-family:
                   Helvetica; display: inline-block; margin:
                   0px auto; text-align: center;}");
72              client.println(".button { background-color:
                   #4CAF50; border: none; color: white;
                   padding: 16px 40px;");
73              client.println("text-decoration: none;
                   font-size: 30px; margin: 2px; cursor:
                   pointer;}");
74              client.println(".button2 {background-color:
                   #555555;}</style></head>");
75
76              // Web Page Heading
77              client.println("<body><h1>ESP32 Web
                   Server</h1>");
78
79              if (flag == 0) {
80                client.println("<p><a
                     href=\"/START\"><button
                     class=\"button\">START</button></a></p>");
81              } else {
82                client.println("<p><a
                     href=\"/STOP\"><button class=\"button
                     button2\">STOP</button></a></p>");
83              }
84
```

```
85              if (flag == 0) {
86                 client.println("<p> Bc's </p>");
87                 client.println("<p>" + testo + "</p>");
88                }
89
90              client.println("</body></html>");
91              client.println();
92              break;
93            }
94            else { // if you got a newline, then clear
                 currentLine
95              currentLine = "";
96            }
97          }
98          else if (c != '\r') {   // if you got anything
               else but a carriage return character,
99           currentLine += c;  // add it to the end of the
               currentLine
100         }
101       }
102     }
103     // Clear the header variable
104     header = "";
105     // Close the connection
106     client.stop();
107     Serial.println("Client disconnected.");
108     Serial.println("");
109   }
110
111
112 }
```

C.2.1 Boundary condition system thermocouple

The substrate temperature is an unmanageable parameter that needs to be monitored, as this could affect the quality of the molten pool process. The K-type

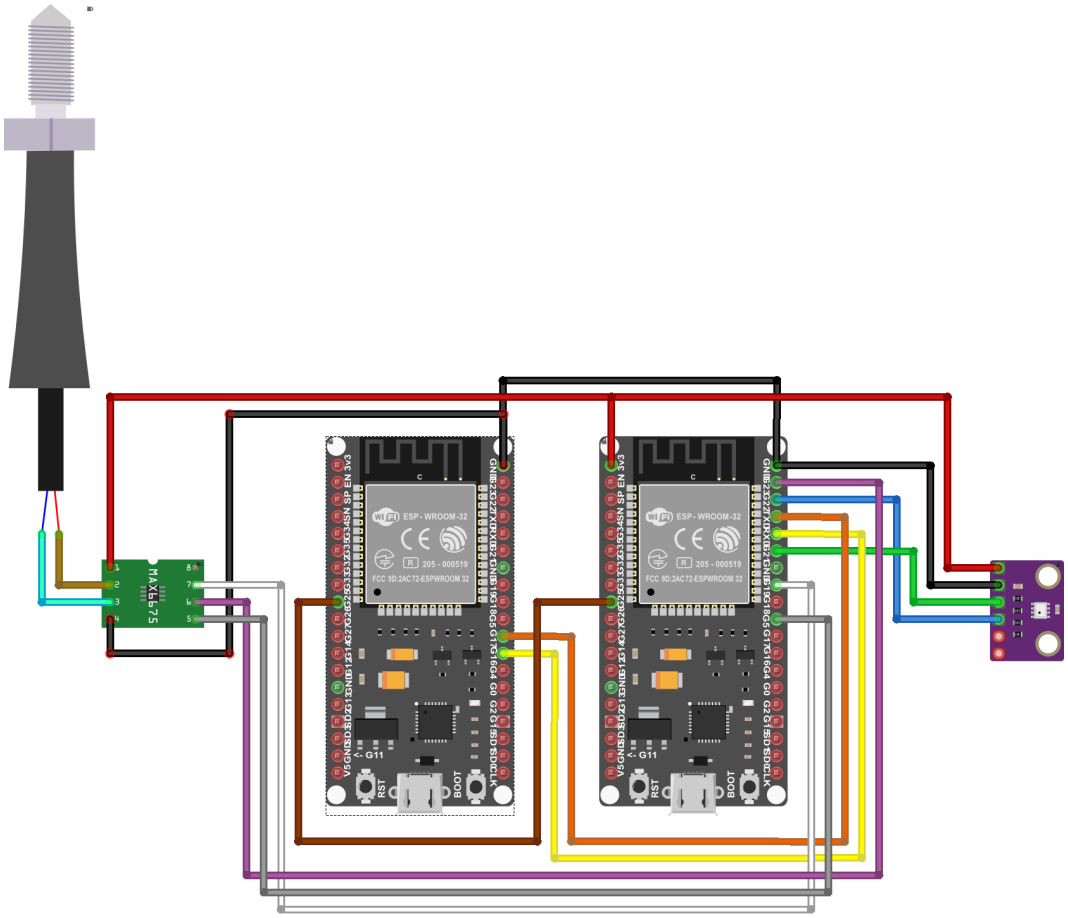

Fig. C.1 BCs monitoring system sketch

(chromel–alumel) thermocouple probe and a MAX6675 were selected to acquire the temperature as a covariate. The MAX6675 is an amplifier that performs cold-junction compensation and treats the signal from the thermocouple. The latter can reach temperatures of 0 °C–1024 °C, and has an accuracy of 8 LSBs (12-bit). The thermocouple has a gain of 41 µV·°C^{-1} and shows a linear characteristic between 0 °C and 700 °C:

$$V_{OUT} = (41\,\mu\text{V}) \cdot (T_R - T_{AMB}) \tag{C.1}$$

where V_{OUT} corresponds to the amplifier output voltage in µV, T_T is the temperature measured by the thermocouple, and T_{AMB} is the room temperature, both in °C. The monitoring system is qualitatively represented in Fig. C.1, and since it must be installed inside the construction chamber, it is plugged into an IP55 box, except for the sensors.

The system was calibrated using a thermostatic bath of distilled water under two conditions: 0 °C (melting ice) and 100 °C (boiling water). It should be noted that distilled water boils at 100 °C only under standard conditions (101.325 kPa), so a function that combines pressure and boiling temperature must be used to overcome this problem. Physics comes to aid with the Clapeyron equation for vaporization of a liquid [89]:

$$T_B = \left(\frac{1}{T_0} - \frac{\bar{R} \cdot \ln \frac{p}{p_0}}{\Delta H_{\text{vap}}} \right) \tag{C.2}$$

where T_B is the boiling point at the pressure p, R is the ideal gas constant, p is the vapor pressure of the water, p_0 is 101.325 kPa for the water, T_0 is equal to 100 °C, and ΔH_{vap} is the enthalpy of vaporization of the water. Furthermore, the semiempirical Antoine equation is most manageable based on experimental data and is derived from Claperyon's equation. Several Antoine equations are available in the literature with different parameter numbers (2 to 4). In this case, the three-parameter Antoine equation with a validity range between 0 and 100 °C is necessary. The formula used is the following:

$$T = \frac{B}{A - \log_{10} p} - C \tag{C.3}$$

where p is the vapour pressure in mmHg, T is the boiling temperature in °C and A = 7.96681, B = 1668.21, and C=228 are the water Antoine constants.

The calibration of the system was carried out in a single day with four replications; to be more precise, the measurement was carried out alternatingly from the melting ice to the boiling water, with respect to the dynamic response time of the sensor as reported in Table C.1, where WIT is the ideal temperature of the water, BT is the actual temperature of the bath, and in the last column there are the related measures.

The data indicate that the boiling water temperature at the measured pressure may be considered to be constant for the resolution of the system since the calibration was carried out in a short time. The linear regression resulted in the following equation:

$$\text{Output}/^\circ\text{C} = 3.725 + 1.00443 \cdot \text{input}/^\circ\text{C} \tag{C.4}$$

The regression model yields a standard deviation of 0.28 and an R^2 of almost100 %. As Fig. C.2 shows, to obtain the expected value, a roto-translation of the real

Table C.1 Thermocouple calibration data

Test	WIT /°C	Pressure/Pa	BT/°C	Measurement/°C
1	0	98779.8	0.00	3.63
2	100	98779.1	99.45	102.85
3	0	98779.5	0.00	3.63
4	100	98779.8	99.46	103.83
5	0	98777.5	0.00	3.78
6	100	98801.6	99.46	104.08
7	0	98799.0	0.00	3.58
8	100	98799.2	99.45	103.15
9	0	98799.3	0.00	4.03
10	100	98793.8	99.45	104.20

thermocouple interpolation was performed:

$$q_i = \frac{(q_o - b)}{m} \tag{C.5}$$

where q_i is the expected value, q_o is the experimental value, b is 3.725, and m is 1.00443. Note that the model result was rounded to reflect the resolution of the thermocouple and the standard deviation of the regression.

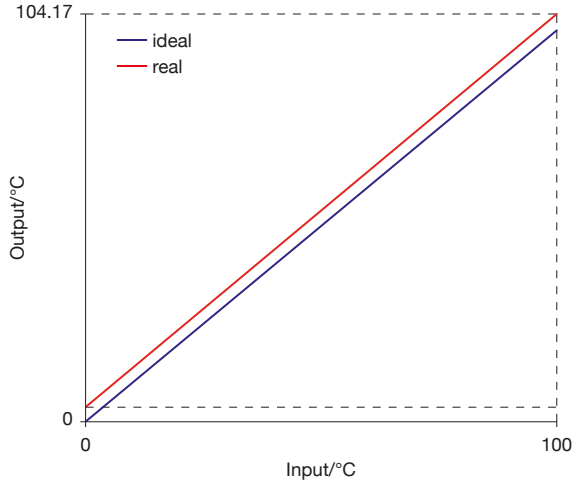

Fig. C.2 Thermocouple calibration

Appendix D

Powder feeder characterization

Table D.1 Powder feeder experiment Data

Std. Order	ω/ rpm	V_{Ar}/ L·min^{-1}	Q_p/ g·min^{-1}	T_A/ °C	p/ Pa	H_A/ g·m^{-3}
1	2	2	2.44	25.7	98052	11.0
2	2	4	1.29	25.5	98096	11.1
3	2	6	0.73	25.5	98105	11.2
4	2	8	0.28	27.3	98283	10.7
5	6	2	6.59	26.3	97968	10.6
6	6	4	4.59	25.4	98126	11.2
7	6	6	2.28	25.9	98018	10.9
8	6	8	1.23	27.6	98268	10.9
9	10	2	11.43	26.2	97948	10.4
10	10	4	8.49	25.5	98111	11.2
11	10	6	5.15	25.9	98039	11.0
12	10	8	2.76	28.0	98238	10.9
13	14	2	15.20	26.3	98006	11.0
14	14	4	12.49	25.9	98034	10.9
15	14	6	7.07	25.6	98093	11.1
16	14	8	4.07	27.0	98307	10.6
17	18	2	20.82	25.3	98138	11.2
18	18	4	16.30	25.7	98066	11.1

Table D.1 – continued from previous page

Std. Order	ω/ rpm	V_{Ar}/ L·min^{-1}	Q_p/ g·min^{-1}	T_A/ °C	p/ Pa	H_A/ g·m^{-3}
19	18	6	9.16	26.3	98004	10.4
20	18	8	5.27	27.9	98242	10.9
21	22	2	25.02	29.22	98641	12.4
22	22	4	15.37	29.05	98639	12.2
23	22	6	8.34	28.98	98649	12.3
24	22	8	5.14	29.12	98641	12.2
25	2	2	1.76	26.2	98020	11.0
26	2	4	1.37	25.6	98073	11.1
27	2	6	0.75	25.4	98117	11.2
28	2	8	0.26	26.8	98303	10.6
29	6	2	7.59	25.9	98040	11.0
30	6	4	4.14	25.3	98138	11.2
31	6	6	2.47	25.5	98100	11.1
32	6	8	1.42	27.9	98245	11.0
33	10	2	11.35	25.2	98142	11.2
34	10	4	8.29	26.3	97968	10.4
35	10	6	4.86	25.6	98080	11.1
36	10	8	2.52	27.7	98257	10.9
37	14	2	18.89	26.3	98011	10.5
38	14	4	10.48	26.3	97999	10.4
39	14	6	6.75	25.6	98091	11.1
40	14	8	4.31	26.6	98312	10.5
41	18	2	22.82	25.9	98043	11.0
42	18	4	16.24	26.3	97977	10.6
43	18	6	8.67	26.3	97983	10.3
44	18	8	4.47	27.5	98272	10.8
45	22	2	19.46	29.4	98611	12.4
46	22	4	15.69	29.2	98634	12.3
47	22	6	7.15	29.4	98621	12.2
48	22	8	5.45	29.1	98651	12.3
49	2	2	2.55	26.1	98014	10.9

Table D.1 – continued from previous page

Std. Order	ω/ rpm	V_{Ar}/ L·min^{-1}	Q_p/ g·min^{-1}	T_A/ °C	p/ Pa	H_A/ g·m^{-3}
50	2	4	1.50	25.6	98082	11.1
51	2	6	1.00	25.8	98041	11.0
52	2	8	13.99	28.0	98235	11.0
53	6	2	6.73	25.5	98108	11.1
54	6	4	4.65	26.2	97971	10.6
55	6	6	2.65	26.0	98016	10.9
56	6	8	1.00	27.1	98291	10.7
57	10	2	11.72	26.3	97956	10.4
58	10	4	8.11	26.3	97989	10.3
59	10	6	5.09	25.7	98069	11.1
60	10	8	2.92	27.7	98250	10.9
61	14	2	17.71	26.3	98000	10.5
62	14	4	12.89	26.0	98005	10.9
63	14	6	7.00	25.7	98072	11.1
64	14	8	4.07	27.2	98291	10.7
65	18	2	21.87	25.3	98126	11.2
66	18	4	16.09	26.3	97980	10.7
67	18	6	9.34	25.8	98051	11.0
68	18	8	4.72	27.8	98243	10.9
69	22	2	25.06	29.1	98648	12.2
70	22	4	14.61	28.9	98657	10.4
71	22	6	8.66	29.2	98635	12.2
72	22	8	4.03	29.5	98609	12.4

Appendix E

Melt Pool and Track Formation: Modeling and Experiments

Table E.1 Optimization of carrier gas flow level experiment Data

Std. Order	Run Order	V_{Ar}/ L·min^{-1}	κ	Height/ %	T_A/ °C	H_A/ g·min^{-1}
3	1	5	1.50	85.15	24.58	10.9
5	2	6	1.25	103.95	26.11	10.6
16	3	7	1.00	106.70	26.36	10.6
26	4	7	1.25	105.80	26.54	10.2
25	5	7	1.00	106.45	26.83	10.1
20	6	5	1.25	96.70	27.01	10.1
27	7	7	1.50	110.35	27.10	10.2
9	8	7	1.50	112.90	27.24	10.1
12	9	5	1.50	102.90	27.36	10.1
23	10	6	1.25	106.15	27.47	10.0
21	11	5	1.50	101.40	27.57	9.9
11	12	5	1.25	94.50	27.62	9.8
6	13	6	1.50	126.55	27.80	9.8
4	14	6	1.00	115.40	27.94	9.8
1	15	5	1.00	113.75	27.93	9.8
18	16	7	1.50	134.85	28.01	9.7

Table E.1 – continued from previous page

Std. Order	Run Order	V_{Ar}/ L·min^{-1}	κ	Height/ %	T_A/ °C	H_A/ g·min^{-1}
24	17	6	1.50	129.60	28.12	9.7
10	18	5	1.00	114.55	28.24	9.8
2	19	5	1.25	122.05	28.26	9.7
19	20	5	1.00	114.70	28.34	9.7
17	21	7	1.25	137.00	28.44	9.6
14	22	6	1.25	123.05	28.63	9.6
15	23	6	1.50	124.90	28.69	9.7
8	24	7	1.25	138.25	28.79	9.7
13	25	6	1.00	127.70	29.01	9.7
22	26	6	1.00	123.25	29.11	9.6
7	27	7	1.00	134.05	29.13	9.7

Table E.2 Factor screening experiment Arrangement

Std. Order	Run Order	Block	Pos. Substrate	E/ J·mm^{-2}	ΔZ/ mm	O_e	κ
25	1	3	11	46	0.4	0.0	1.4
35	2	3	9	60	0.6	0.0	1.4
31	3	3	2	60	0.6	0.0	1.4
36	4	3	8	46	0.6	0.5	1.25
34	5	3	12	60	0.4	0.5	1.25
28	6	3	3	46	0.6	0.5	1.25
29	7	3	7	46	0.4	0.0	1.4
33	8	3	1	46	0.4	0.0	1.4
27	9	3	6	60	0.6	0.0	1.4
26	10	3	5	60	0.4	0.5	1.25
32	11	3	10	46	0.6	0.5	1.25
30	12	3	4	60	0.4	0.5	1.25
38	13	4	3	46	0.4	0.5	1.4
41	14	4	8	60	0.4	0.0	1.25
46	15	4	7	46	0.4	0.5	1.4
42	16	4	10	46	0.4	0.5	1.4
48	17	4	1	60	0.6	0.5	1.4
45	18	4	11	60	0.4	0.0	1.25
44	19	4	5	60	0.6	0.5	1.4
43	20	4	9	46	0.6	0.0	1.25
39	21	4	12	46	0.6	0.0	1.25
47	22	4	2	46	0.6	0.0	1.25
40	23	4	4	60	0.6	0.5	1.4
37	24	4	6	60	0.4	0.0	1.25
4	25	1	1	60	0.6	0.5	1.25
8	26	1	8	60	0.6	0.5	1.25
5	27	1	4	60	0.4	0.0	1.4
3	28	1	10	46	0.6	0.0	1.4
2	29	1	12	46	0.4	0.5	1.25
10	30	1	9	46	0.4	0.5	1.25
7	31	1	7	46	0.6	0.0	1.4

Table E.2 – continued from previous page

Std. Order	Run Order	Block	Pos. Substrate	E/ J·mm^{-2}	ΔZ/ mm	O_e	κ
11	32	1	6	46	0.6	0.0	1.4
6	33	1	2	46	0.4	0.5	1.25
9	34	1	5	60	0.4	0.0	1.4
1	35	1	3	60	0.4	0.0	1.4
12	36	1	11	60	0.6	0.5	1.25
16	37	2	6	46	0.6	0.5	1.4
19	38	2	3	60	0.6	0.0	1.25
14	39	2	2	60	0.4	0.5	1.4
15	40	2	12	60	0.6	0.0	1.25
20	41	2	11	46	0.6	0.5	1.4
24	42	2	8	46	0.6	0.5	1.4
17	43	2	10	46	0.4	0.0	1.25
18	44	2	4	60	0.4	0.5	1.4
13	45	2	9	46	0.4	0.0	1.25
23	46	2	1	60	0.6	0.0	1.25
21	47	2	5	46	0.4	0.0	1.25
22	48	2	7	60	0.4	0.5	1.4

Table E.3 Factor screening experiment Data

Heigth/ %	Density/ $g \cdot cm^{-3}$	Porosity/ %	Hardness/ (HV/0.5/15)	T_T/ °C	T_A/ °C	H_A/ $g \cdot m^{-3}$
101.16	7.928	1.032	166	24.6	25.3	6.4
99.16	7.926	0.051	165	*	25.9	6.4
101.25	7.933	0.084	167	21.2	26.3	6.2
98.63	7.936	0.033	169	18.9	26.5	6.2
103.92	7.939	0.017	166	18.8	26.5	6.2
97.79	7.916	0.021	167	23.1	26.5	6.2
99.78	7.909	1.305	170	19.0	26.6	6.2
101.68	7.924	0.050	172	19.9	26.9	6.2
98.28	7.926	0.009	166	22.9	26.8	6.2
105.28	7.934	0.069	161	20.0	27.1	6.2
99.35	7.928	0.329	170	22.8	27.2	6.2
106.03	7.936	0.024	160	21.4	27.1	6.3
104.08	7.949	0.016	165	*	24.9	6.2
100.13	7.922	1.116	167	17.8	25.4	6.2
103.81	7.941	0.025	164	14.2	25.6	6.1
105.56	7.939	0.016	167	18.7	25.7	6.1
102.21	7.929	0.021	168	18.4	25.8	5.9
101.78	7.919	0.767	164	17.3	26.1	5.9
102.58	7.930	0.045	171	20.6	26.2	5.8
99.14	7.914	0.195	172	16.9	26.2	5.8
98.28	7.925	0.036	169	16.0	26.1	5.8
97.92	7.930	0.028	168	15.8	26.2	5.8
102.57	7.923	0.010	162	17.1	26.2	5.9
103.03	7.912	0.015	166	19.1	26.6	5.9
100.20	7.916	0.032	164	16.6	26.3	5.9
100.19	7.915	0.012	159	21.5	26.6	5.9
103.79	7.924	0.053	168	22.2	26.9	5.9
98.88	7.917	0.064	170	17.4	27.0	6.1
105.89	7.895	0.016	167	18.6	27.1	6.0
106.40	7.882	0.011	161	18.0	27.2	5.9
97.88	7.895	0.062	167	20.9	27.4	6.1

Table E.3 – continued from previous page

Heigth/ %	Density/ g·cm^{-3}	Porosity/ %	Hardness/ (HV/0.5/15)	T_T/ °C	T_A/ °C	H_A/ g·m^{-3}
98.34	7.913	0.018	168	15.1	27.7	6.1
105.61	7.897	0.034	164	22.0	27.9	6.2
105.65	7.883	1.670	170	22.0	28.0	6.1
102.01	7.907	0.037	163	22.2	27.9	6.2
101.39	7.902	0.045	163	20.0	28.1	6.3
98.59	7.890	0.014	161	*	25.5	7.8
95.44	7.960	0.012	163	16.3	26.1	8.0
105.74	7.957	0.681	169	15.4	26.5	8.1
96.50	7.946	0.024	162	22.3	26.7	8.1
100.52	7.961	0.020	165	18.4	26.7	8.0
100.60	7.965	0.147	170	19.0	26.9	8.1
99.60	7.958	0.021	169	16.0	26.9	8.3
106.33	7.963	0.180	169	17.4	27.2	8.4
101.94	7.950	0.018	168	24.8	27.4	8.4
96.80	7.951	0.066	168	24.8	27.5	8.4
101.58	7.958	0.051	168	17.6	27.5	8.3
103.90	7.947	0.463	166	19.7	27.4	8.4

Appendix F

Linking the process parameters

F.1 Matlab code

```
clc;
clear all;
close all;

%%%%%%%%%%%%%%%%%%%%%%%%%%%%%%%%%%%%%%%%%%%%%%%%%%%%%%%%%%%%%%%%%%%%
%%%%%%%%%%%POWDER STREAM CHARACTERIZATION%%%%%%%%%%%%%
% Query the user for the number of rotational speed levels to explore
num_levels = input('How many levels of Rotational Speed would you like to investigate? (suggestion: 3): ');
% Validate input
if num_levels < 2
    error('The number of levels must be at least 2 to perform a linear regression.');
end

% Query the user for the minimum and maximum omega values
```

```
15 omega_min = input('Enter the minimum Rotational speed
       in rpm: ');
16 omega_max = input('Enter the maximum Rotational speed
       in rpm: ');
17 % Calculate the omega level increment
18 delta_omega = (omega_max - omega_min) / (num_levels -
       1);
19
20 % Calculate the increment between omega levels
21 omega_levels = omega_min:delta_omega:omega_max;
22
23 % Query the user for the number of replicates for
       each level
24 num_replicates = input('How many replicates would you
       like to perform for each level? (suggestion: 5): '
       );
25
26 % Create the final omega vector based on the levels
       and replicates
27 omega = repelem(omega_levels, num_replicates);
28
29 % Display the vector
30 disp('The Rotation vector is:');
31 disp(omega);
32
33 % Generate a randomized index to conduct the
       experiment in randomized order
34 random_idx = randperm(length(omega));
35
36 % Reorder the omega vector using the randomized index
37 omega_randomized = omega(random_idx);
38
39 % Ask the user if they want to view the randomized
       test order
```

```
answer = input('Would you like to view the randomized order for conducting the tests? (yes/no): ', 's');

if strcmpi(answer, 'yes')
    % Display the randomized omega vector
    disp('Execute the tests in the following order:');
    disp(omega_randomized);
end

%%%%%%%%%%%%%%%%%%%%%RESPONSE%%%%%%%%%%%%%%%%%%%%%
% Asks the user if they want to input the Qp vector manually
answer = input('Do you want to enter the Qp vector manually? (yes/no): ', 's');

if strcmpi(answer, 'yes')
    % If the user says 'yes', they will input the Qp vector manually
    Qp = input('Please enter the Qp (in g/min) vector manually: ');
else
    % Otherwise, use the predefined Qp vector
    Qp = [0.8 0.9 0.7 4.1 4.3 4.3 7.7 8.5 7.5];
    % Qp = [0.7 0.8 0.6 0.7 0.7 6.6 6.5 6.7 6.6 6.6 12.5 12.4 12.6 12.5 12.5]; % Insert test values here
    disp('Using predefined Qp values.');
end

% Create a data table for regression
tbl = table(omega', Qp', 'VariableNames', {'Omega', 'Qp'});

```

```
% Execute stepwise regression with alpha-to-enter and
    alpha-to-remove at 10%
% Including linear and quadratic terms for omega
mdl = stepwiselm(tbl, 'Qp~1+Omega+Omega^2', '
   Criterion', 'SSE','Premove',0.1);

% Display the selected model
disp('Optimized Model:');
disp(mdl);

% Display model coefficients
disp('Model Coefficients:');
disp(mdl.Coefficients.Estimate);
regressors = mdl.Coefficients.Estimate;
indices = find(abs(regressors) < 0.001); % Find the
   indices of elements that are smaller than 0.001
regressors(indices) = 0; % Set the corresponding
   elements to 0

% Create data for the plot
omega_range = linspace(min(omega), max(omega), 100)';
tbl_predict = table(omega_range, 'VariableNames', {'
   Omega'});
Qp_fit = predict(mdl, tbl_predict);

% Ask the user if they want to view the regression
   plot
plot_decision = input('Would you like to view the
   regression plot? Respond with "yes" or "no": ', 's'
   );

if strcmpi(plot_decision, 'yes')
% Display the plot
    figure;
```

```
91      scatter(omega, Qp, 'b', 'filled'); % Experimental
            data
92      hold on;
93      plot(omega_range, Qp_fit, 'r', 'LineWidth', 2); %
            Regression fit function
94      xlabel('Omega');
95      ylabel('Qp');
96      legend('Data', 'Regression');
97      title('Regression');
98      hold off;
99  end
100
101 % Calculation of the minimum and maximum omega values
        in the range of interest
102 omega_min = min(omega);
103 omega_max = max(omega);
104
105 % Create a table with the minimum and maximum values
        of omega
106 tbl_min_max = table([omega_min; omega_max], '
        VariableNames', {'Omega'});
107
108 % Predict the minimum and maximum values of Qp using
        the model
109 Qp_min_max = predict(mdl, tbl_min_max);
110
111 % Extract and store the minimum and maximum values of
        Qp
112 Qp_min = min(Qp_min_max);
113 Qp_max = max(Qp_min_max);
114
115 % Display the results
116 fprintf('The minimum value of Qp for the powder
        feeder is: %.2f g/min\n', Qp_min);
```

```
117 fprintf('The maximum value of Qp for the powder
       feeder is: %.2f g/min\n', Qp_max);
118
119 %%%%%%%%%%%%%%%%%%PROCESS PARAMETERS%%%%%%%%%%%%%%%%%%
120 % Input manually the data
121 Oe = 50; % 50 if using 50 % overlap, otherwise
       without overlap with any other number
122 P = 750; % Laser Beam power in W
123 DeltaZ = 0.6; % value between 0.4 mm and 0.6 mm
124 D = 2; % Laser beam diameter in mm
125 rho = 7.896e-3;  % Powder density in g/mm^3
126 H = 100; % Height of the desired layer in percentage
127
128 % Prompt user to choose between using v or E
129 choice = input('Would you like to use v or E? Enter "
       v" or "E": ', 's');
130
131 if strcmpi(choice, 'v')
132     % If the user chooses 'v', prompt for its value
          and set E to NaN
133     v = input('Enter the value of v in mm/min: ');
134     E = NaN; % Update E with NaN
135 elseif strcmpi(choice, 'E')
136     % If the user chooses 'E', prompt for its value
          and set v to NaN
137     E = input('Enter the value of E in J/mm^2: ');
138     v = NaN; % Update v with NaN
139 else
140     error('Invalid choice. You must enter either "v"
          or "E".');
141 end
142
143 % Check if v is a numeric value
144 if ~isnan(v)
```

```
145     E = P * 60 / (v * D); % Calculate E if v is a
            numeric value in J*mm^[117]
146     if Oe == 50
147         E = E * 2; % The energy per layer is doubled
                due to the increased number of passes
148     end
149 % Check if E is a numeric value
150 elseif ~isnan(E)
151     v = P * 60 / (E * D); % Calculate v if E is a
            numeric value in mm*min^{-1}
152     if Oe == 50
153         v = v * 2; % The energy per layer is doubled
                due to the increased number of passes
154     end
155 else
156     error('At least one of v or E must be a numeric
            value.');
157 end
158
159 fprintf('The calculated value of E per layer is: %.1f
    \n', E);
160
161 %%%%%%%%%%CALCULATION OF POWDER FEED RATE%%%%%%%%%%
162 halfFlag = 0;
163 if Oe == 50
164     halfFlag = 1;
165     k_calculated = (201.6 - H - 0.440 * E - 2.414 *
            DeltaZ) / (0.448 - 0.501 * E - 0.352 * DeltaZ);
166 else
167     k_calculated = (100.0 - H - 0.440 * E - 1.844 *
            DeltaZ) / (0.448 - 0.501 * E - 0.352 * DeltaZ);
168 end
169
170 % If k_calculated is less than 1, set it to 1
171 if k_calculated < 1
```

```
172     k_calculated = 1;
173 end
174
175 Qp_calculated = k_calculated * (D * v * DeltaZ) * rho
    ;
176
177 if halfFlag == 1
178     Qp_calculated = 0.5 * Qp_calculated;  % If
        constructed with overlap, the feed rate should
        be halved
179 end
180
181 % Check on Qp_calculated
182 if Qp_calculated < Qp_min || Qp_calculated > Qp_max
183     warning('The powder feeder is unable to construct
         adequately with these geometric parameters.
        Consider modifying DeltaZ or v.');
184 end
185
186 % Set the symbolic variable and the quadratic
    equation
187 Omega_sym = sym('Omega_sym');
188 eqn = regressors(1) + regressors(2) * Omega_sym +
    regressors(3) * Omega_sym^2 == Qp_calculated;
189
190 % Solve the equation
191 sol = solve(eqn, Omega_sym);
192
193 % Extract numerical values
194 omega_calculated = double(sol);
195
196 % Update specific layer energy
197 if Oe == 50
198     E = E * 2; % The energy per layer is doubled due
        to the increased number of passes
```

```
199 end
200
201 % Check if the equation is linear or quadratic
202 if length(omega_calculated) == 1
203     fprintf('The calculated value of Rotations is:
          %.1f\n', omega_calculated);
204 else
205     fprintf('The calculated value of Rotations is:
          %.1f (second root)\n', omega_calculated(2));
206 end
207
208 fprintf('The calculated value of k is: %.2f\n',
      k_calculated);
209 fprintf('The calculated value of v based on the
      specific energy supplied is: %.1f\n', v);
210 fprintf('The calculated value of Qp is: %.1f\n',
      Qp_calculated);
211
212 %%%%%%%%%%%%%%%%%%%%%%FIGURE%%%%%%%%%%%%%%%%%%%%%%%%
213 % Formatting Constants
214 height = 7; % Height in cm
215 width = 9; % Width in cm
216 Fontsize = 7; % Font size in pt
217 LineWidth = 0.25; % Axis and dashed line width in pt
218 tickLengthCm = 0.07; % Tick length in cm
219 cm_to_points = 72 / 2.54; % Conversion factor from cm
      to points
220
221 % Create a figure with specified dimensions in
      centimeters
222 figure('Units','centimeters','Position',[0 0 width
      height]);
223
224 % Scatter plot (blue points without edge)
```

```
225 scatter(omega, Qp, 1.2*cm_to_points, 'bo', 'filled',
       'MarkerEdgeColor', 'none');
226 hold on;
227
228 % Regression plot
229 plot(omega_range, Qp_fit, 'r', 'LineWidth', 0.75);
230
231 % Line segments with 0.25 pt width
232 plot([omega_calculated, omega_calculated], [0,
       Qp_calculated], 'k--', 'LineWidth', LineWidth);
233 plot([0, omega_calculated], [Qp_calculated,
       Qp_calculated], 'k--', 'LineWidth', LineWidth);
234
235 % Additional points (green point without edge and
       same size)
236 scatter(omega_calculated, Qp_calculated, 1.2*
       cm_to_points, 'g', 'filled', 'MarkerEdgeColor', '
       none');
237
238 % X and Y Labels
239 hx = xlabel('Rotation / rpm');
240 hy = ylabel('Qp / g \cdot min^{-1}');
241
242 % Font settings
243 set([hx, hy], 'FontName', 'Helvetica Neue', 'FontSize
       ', Fontsize, 'Color', 'k');
244 set(gca, 'FontName', 'Helvetica Neue', 'FontSize',
       Fontsize, 'XColor', 'k', 'YColor', 'k');
245
246 % Line settings for axis
247 set(gca, 'LineWidth', LineWidth);
248
249 % Tick settings
250 set(gca, 'TickDir', 'out');
```

```
251 set(gca, 'TickLength', [tickLengthCm/10, tickLengthCm
    /10]) % Adjusted the tick length
252
253 % Legend with consistent font and size
254 hl = legend('Powder Feeder Tests', 'Regression', '
    Calculated Point', 'Location', 'northwest');
255 set(hl, 'FontName', 'Helvetica Neue', 'FontSize',
    Fontsize, 'TextColor', 'k', 'Box', 'off');
256
257 % X and Y Limits
258 xlim([omega_min, omega_max]);
259
260 % Turn off the box
261 set(gca, 'Box', 'off');
262
263 hold off;
```